THE UNIVERSITY *of* EDINBURGH

Scattering and diffusion of inertia-gravity waves

Michael R. Cox

Doctor of Philosophy
University of Edinburgh
June 2024

Abstract

Inertia-gravity waves (IGWs) propagate under the restoring forces of buoyancy and the Coriolis effect. They are present in the ocean and the atmosphere and play a key role in the energetics of both. As IGWs propagate, they encounter inhomogeneities such as background flows, bottom topography and other waves. If these inhomogeneities are weak and either slowly evolving or stationary, the IGWs are scattered and their energy spreads through wavenumber space whilst preserving frequency.

The scattering of IGWs by weak, slowly evolving background flows can be modelled as a spectral diffusion process providing the IGWs propagate in the WKB regime, that is, they have much shorter spatial scales than the background flow. Previous studies consider Doppler shift to be the sole mechanism causing IGW diffusion. If the flow evolves so slowly it can be considered stationary, it can be shown that energy diffuses along cones of constant frequency in wavenumber space.

In this thesis, we relax the assumption of time-independent background flow and find that a slowly time-dependent flow induces energy diffusion across the constant frequency cones. We solve the corresponding diffusion equation and find energy decays rapidly away from the cone within a thin boundary layer.

We consider mechanisms for wave diffusion other than Doppler shift. We generalise the diffusion equation to account for any weak, slowly evolving inhomogeneities interacting with waves in the WKB regime. We evaluate the general diffusivity and find exact solutions for two examples of these inhomogeneities: fluctuations in the IGW buoyancy frequency due to the thermal wind balance and, for a rotating shallow water system, fluctuations in the layer height due to geostrophic balance. For the latter, we support our findings with ray tracing simulations.

Lay summary

The atmosphere and oceans are examples of rotating fluids of varying density. Waves propagate through the interior of these fluids, driven by buoyancy and rotation effects. These waves, called inertia-gravity waves, are important in transporting and mixing heat, pollutants and carbon dioxide, amongst other things.

Mathematical models are used to predict the way in which fluid in the atmosphere and ocean evolves. These models can be local – for example, tidal predictions at a harbour. The model predictions may be relatively short term, as is the case for daily weather forecasts. Models also operate on much larger scales in space and time. This is the case for climate models, used to make global, long-term predictions of changes in, for example, temperature and sea-level rise.

Large-scale mathematical models for the atmosphere and ocean focus on larger scale motions than waves, such as the swirling eddies that can be seen in weather forecasts which are 100–1000 kms across. However, waves change the way in which large features behave, and vice versa. It is important to understand how waves behave and interact with large-scale fluid flow in order to accurately model the atmosphere and oceans.

This thesis concerns the interactions of waves with large-scale, slowly changing features, such as slowly evolving eddies. Specifically, it looks at how the eddies and other large-scale features impact the waves. We find that if an eddy is sufficiently slow in its evolution, it can be considered stationary when modelling its impact on the waves. After this, we look at the interactions between other large-scale features and the waves, such as density changes and an uneven seabed, and derive a general equation to describe these interactions.

Declaration

I declare that this thesis was composed by myself and that the work contained therein is my own, except where explicitly stated otherwise in the text.

Michael R. Cox

Acknowledgements

I am indebted to my supervisors, Jacques Vanneste and Hossein Kafiabad, for their guidance and support over the past few years. They have been extraordinarily generous with their time, especially in recent months leading up to this submission. It has been a pleasure to work with you both. I hope our collaborations continue long into the future.

I am grateful to Carsten Eden and Manita Chouksey for their hospitality in hosting me at the theoretical oceanography department, Universität Hamburg, for 2 months.

Without amazing teachers and mentors, this thesis would not exist. Thank you to Mr Barry, Dr Udall, Mr Ibison, Mike Gunn, Martin Long and Alexandra Tzella.

I thank my family and friends for their support throughout my education. My parents and grandparents have always encouraged me to be curious about the world we live in. My brother has been a wonderful companion in this. To Holly, my partner, thank you for making me smile every day.

My grandfather, Dr Albert Peter Cox, was delighted to hear of my first publication some sixty years after his own. This thesis is dedicated to his memory.

* * *

This work was supported by the MAC-MIGS Centre for Doctoral Training under grant EP/S023291/1 of the UK Engineering & Physical Sciences Research Council (EPSRC).

Contents

Chapter 1

Introduction

Inertia-gravity waves (IGWs), also called internal waves or gravity waves, propagate in the atmosphere and ocean under the restoring forces of the Coriolis effect and buoyancy. They are generated by a variety of mechanisms. For example, near-inertial waves are primarily generated by wind forcing and propagate close to the inertial (Coriolis) frequency (see Alford *et al.* (2016) for a review). Large scale currents generate IGWs as they pass over bottom topography: steady currents give rise to lee waves; oscillatory tidal currents driven by astronomical forcing result in internal tides that propagate at the diurnal and semi-diurnal frequencies (e.g. Bell 1975). Waves are also emitted spontaneously as part of the evolution of slow currents or through instability mechanisms (see reviews Vanneste, 2013; Plougonven & Zhang, 2014). The majority of IGW energy in the ocean is distributed between near-inertial waves and internal tides. This can be seen in IGW energy spectra which peak at the inertial, diurnal and semi-diurnal frequencies with a continuum of frequencies between (e.g. Ferrari & Wunsch 2009; Luecke *et al.* 2020).

Most of the energy in the atmosphere and ocean is contained in large-scale, layer-wise two-dimensional turbulence. These low-frequency, horizontal currents evolve on scales of 1000 kms in the atmosphere (the synoptic scale) and 100 kms in the ocean (the mesoscale). They are driven by balances between the pressure gradient of the flow and Coriolis and buoyancy forces (e.g. Vallis, 2017*b*). At very large scales, energy is constantly injected by, for example, solar heating and tidal and wind forcing. Layer-wise two-dimensional turbulence theory (Charney, 1971) predicts an inverse cascade

of energy to larger scales and this is the dominant feature of observations (e.g. Scott & Wang, 2005; Schubert, Vergara & Gula, 2023). The same theory predicts a forward cascade of enstrophy to smaller scales (e.g. Pedlosky, 1987) which is also a feature of observations (e.g. Khatri *et al.*, 2018). The inverse cascade of energy requires an accompanying forward cascade to explain how energy is dissipated at small scales by, for example, viscosity. IGWs are thought to facilitate downward energy transfer from large-scale currents (e.g. Ferrari & Wunsch, 2009). As such, it is important to understand the way in which IGWs and large-scale, turbulent currents interact.

Furthermore, although balanced turbulence dominates large-scale energetics, at smaller scales, decompositions of observed atmospheric and oceanic energy spectra suggest that IGWs dominate (Callies & Ferrari, 2013; Callies, Ferrari & Bühler, 2014; Bühler, Callies & Ferrari, 2014; Callies, Bühler & Ferrari, 2016). At these scales, internal wave breaking and the ensuing small-scale turbulence drives vertical mixing in the ocean of heat and other tracers such as pollutants and carbon dioxide (see reviews by Wunsch & Ferrari, 2004; Whalen *et al.*, 2020). Modelling the impact of large-scale currents on IGWs is key to understanding small-scale dynamics and mixing.

The physical and temporal scale separation between slow, large-scale currents and winds and fast, small-scale IGWs makes it difficult to resolve both in large-scale models of the atmosphere and ocean. Recent progress towards including internal waves in global ocean circulation models is summarised by Arbic (2022). Parameterisations, such as IDEMIX (Olbers *et al.*, 2019) and MSG-WaM (Bölöni *et al.*, 2021; Kim *et al.*, 2021; Voelker *et al.*, 2024) aim to capture the effect of internal waves in large-scale models. Understanding the way in which waves interact with large-scale flows and how they evolve is crucial to accurately modelling the atmosphere and ocean.

IGW dynamics are affected by varying background flow velocity, as well as other inhomogeneities such as density profiles, topography and other waves. Inhomogeneities refract, reflect and advect waves. In the ocean, internal tides are refracted by background velocities (which also advect the waves), density profiles and bottom topography (e.g. Pan *et al.*, 2021) causing changes in frequency, wavelength and propagation direction. IGWs incident upon sharp density profiles are reflected (e.g. Sutherland, 2016). Repeated reflection of wave fields at bottom topography in the ocean causes wave energy redistribution (e.g. Müller & Xu, 1992) .

Waves are described in a phase–space, position–wavenumber representation which emerges from phase averaging. Then, wave energy and frequency are functions of position and wavenumber. Advection of waves by a slowly evolving, large-scale background flow results in a Doppler shift term in the wave frequency. This is similar but not equivalent to Doppler shift in physics (Gerkema, Maas & van Haren, 2013).

Repeated, weak interactions between IGWs and inhomogeneities can be modelled statistically as a scattering process of energy in wavevector space (e.g. Hasselmann, 1966). This is the subject of this thesis. Specifically, we focus on the subregime of scattering where there is scale separation between short waves and large-scale inhomogeneities – the WKB regime. In this limit, scattering becomes a diffusion process in spectral space. In the case of scattering by background flow velocities, this spectral diffusion is induced by Doppler shift in the wave frequency.

Doppler-shift-induced spectral diffusion was first proposed by McComas & Bretherton (1977). At the end of this chapter, §1.5, we recap previous work on Doppler-shift-induced diffusion. The generalisation of this diffusion framework to 1) account for time dependence in the background flow (§2) and; 2) account for inhomogeneities other than Doppler shift (§3), are the main results of this thesis.

The remainder of this chapter is as follows. In §1.2, we introduce IGWs mathematically through two models which describe fluid flow in the atmosphere and ocean: the Boussinesq equations describing continuously stratified fluids and the rotating shallow water equations. In §1.3, we outline simplifications to these models which filter out IGWs and describe the large scale, turbulent flow.

In §1.4, we use WKB analysis to examine the effect of a background flow on waves in the rotating shallow water system. We show Doppler shift in the wave frequency emerges from advection. We show that wave action, closely related to wave energy, obeys a conservation law. This conservation law is well known and holds for any short wave interacting with a large-scale, slowly evolving inhomogeneity – the novelty of our derivation is that it is applied to a shallow water system with a background flow of variable height.

Induced spectral diffusion is the weak-interaction limit of wave action conservation. In §1.5, as well as recapping previous results on Doppler-shift-induced diffusion, we reiterate the various assumptions required to move between governing fluid equations,

action conservation, scattering and diffusion.

1.1 Papers and notation

This thesis is based on two papers: §2 contains Cox, Kafiabad & Vanneste (2023), published in the Journal of Fluid Mechanics and; §3 contains Cox, Kafiabad & Vanneste (2024), under review and available at `https://doi.org/10.48550/arXiv.2406.17149`.

Due to the large number of variables and different choices in notation between the first and second paper, there are some symbols with multiple definitions. For example: in §2, ω is the intrinsic frequency of the waves, whereas in §3 it is the total frequency and; across both papers, h is used as a subscript to denote horizontal quantities but in §1.4, it also denotes the wave height in the rotating shallow water system. We include each paper in its entirety and so the notation within each chapter is consistent and symbols are redefined if their definition changes. Outside of §2, variable choices are in-keeping with §3.

1.2 Inertia-gravity waves

The Boussinesq equations describe a rotating, stratified fluid layer and model the fluid flow in the atmosphere and ocean in a highly idealised way. Cartesian geometry is used, justified by considering a small patch of the atmosphere/ocean. Density is decomposed into a mean part, ρ_0, and small variations, $\tilde{\rho}(z) + \rho'(\boldsymbol{x})$,

$$\rho = \rho_0 + \tilde{\rho}(z) + \rho'(\boldsymbol{x}), \tag{1.1}$$

where $\boldsymbol{x} = (\boldsymbol{x}_h, z)$ is Cartesian space with $\boldsymbol{x}_h = (x_1, x_2, 0)$. Then, the buoyancy variable is

$$b = -g\rho'(\boldsymbol{x})/\rho_0, \tag{1.2}$$

where g is gravitational acceleration. For a fluid of velocity $\boldsymbol{u} = (u, v, w)$, pressure p and buoyancy b, the Boussinesq equations are given by the momentum conservation

equation,

$$(\partial_t + \boldsymbol{u} \cdot \boldsymbol{\nabla}_{\boldsymbol{x}})\boldsymbol{u} + f\boldsymbol{e}_z \times \boldsymbol{u} = -\boldsymbol{\nabla}_{\boldsymbol{x}} p + b\boldsymbol{e}_z, \tag{1.3}$$

the mass conservation equation,

$$\boldsymbol{\nabla}_{\boldsymbol{x}} \cdot \boldsymbol{u} = 0, \tag{1.4}$$

and the buoyancy equation,

$$(\partial_t + \boldsymbol{u} \cdot \boldsymbol{\nabla}_{\boldsymbol{x}})b + N^2 w = 0. \tag{1.5}$$

Here, $\boldsymbol{e}_z$ denotes the unit vector in the z direction,

$$N^2(z) = -g\partial_z \tilde{\rho}(z)/\rho_0, \tag{1.6}$$

is the square buoyancy frequency and $f < N$ is the Coriolis frequency. The rotation vector $\boldsymbol{f} = f\boldsymbol{e}_z$ is taken to be constant and parallel to the vertical (this is a combination of the traditional approximation, in which horizontal components of the rotation vector are neglected, and the f-plane approximation, under which the Coriolis frequency is constant). For a derivation of (1.3)–(1.5) and justification of their application to the atmosphere and ocean, see, for example, Vallis (2017*a*).

IGWs are described by the Boussinesq equations (1.3)–(1.5). Assuming the waves are a small perturbation to a homogeneous medium (constant N) at rest, a wave ansatz,

$$(\boldsymbol{u}, p, b)^{\mathrm{T}} = (\boldsymbol{u}', p', b')^{\mathrm{T}} \mathrm{e}^{i(\boldsymbol{k}\cdot\boldsymbol{x} - \omega t)}, \tag{1.7}$$

yields the frequencies $\omega = 0$ and

$$\omega = \pm(f^2 \cos^2\theta + N^2 \sin^2\theta)^{1/2}. \tag{1.8}$$

Here, primes denote constant wave variable amplitudes. The wavevector $\boldsymbol{k} = (k_1, k_2, k_3)$ forms an angle θ with the vertical. IGWs travelling in opposite directions are described by the non-zero frequencies (1.8). The IGW frequencies (1.8) only depend on θ, the polar angle, and so the constant frequency surface is a cone, as shown in figure 1.1.

The three-dimensional Boussinesq system (1.3)–(1.5) is computationally costly to

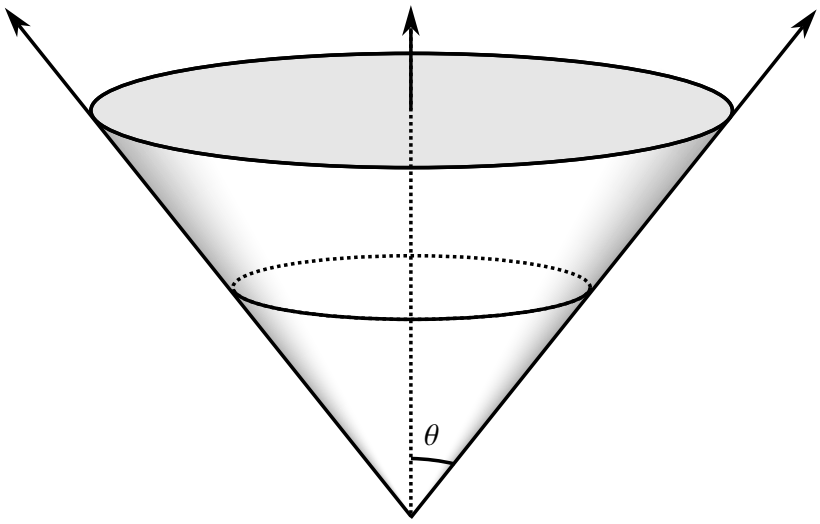

Figure 1.1: In 3D, IGW frequency (1.8) is dependent only on the wavevector's polar angle θ and so the surface of constant frequency in wavevector space is a cone, shown here for $k_3 > 0$.

simulate and tricky to evaluate analytically. A reduced model used in its place is the rotating shallow water system. This two-dimensional model describes a thin layer of rotating fluid with constant density and horizontal motions independent of height. The rotating shallow water momentum equation is

$$(\partial_t + \boldsymbol{u} \cdot \boldsymbol{\nabla}_{\boldsymbol{x}})\boldsymbol{u} + f\boldsymbol{e}_z \times \boldsymbol{u} = -g\boldsymbol{\nabla}_{\boldsymbol{x}}\eta, \tag{1.9}$$

and the mass conservation equation is

$$\partial_t \eta + \boldsymbol{\nabla}_{\boldsymbol{x}} \cdot (\eta \boldsymbol{u}) = 0, \tag{1.10}$$

where $\boldsymbol{u} = (u, v, 0)$ and $\boldsymbol{\nabla}_{\boldsymbol{x}} = (\partial_{x_1}, \partial_{x_2})$ are now horizontal quantities and η is the height of the fluid layer. For simplicity, we have assumed a flat bottom. For a derivation see, for example, Vallis (2017*c*). For a thorough overview of the use of rotating shallow water models in geophysical fluid dynamics, see Zeitlin (2018).

With a wave ansatz of the same form as (1.7), the frequencies of shallow water waves, called Poincaré waves, propagating in a layer of constant height $\bar{H}$ are

$$\omega = \pm(f^2 + g\bar{H}k_h^2)^{1/2}. \tag{1.11}$$

The wavevector magnitude is $k_h = (k_1^2 + k_2^2)^{1/2}$ and the h-subscript emphasises it is horizontal.

A key assumption in the shallow water model (1.9)–(1.10) is hydrostatic balance, whereby the vertical pressure gradient of the fluid is balanced by gravity. This is a valid assumption for fluids with horizontal motions that evolve on much larger spatial scales than the water depth. The hydrostatic approximation can also be applied directly to the Boussinesq system (1.3)–(1.5). Then, the vertical momentum equation becomes

$$\partial_z p = b. \tag{1.12}$$

Unlike rotating shallow water, this allows for a stratification profile $N = N(z)$ and the horizontal motions are not necessarily independent of height. The Boussinesq equations (1.3)–(1.5) with hydrostatic balance (1.12) are a good model for internal tides because of their long wavelength (see, for example, Olbers, Willebrand & Eden, 2012*b*).

For IGWs propagating under hydrostatic balance with a constant buoyancy frequency N, the IGW frequencies (1.8) become

$$\omega = \pm(f^2 + N^2 k_h^2 / k_3^2)^{1/2}. \tag{1.13}$$

1.3 Background flows and geostrophy

IGWs do not propagate in homogeneous mediums at rest. Inhomogeneities cause changes in wavelength, propagation direction, wave amplitude and frequency and the plane wave ansatz (1.7) is insufficient. Unlike the plane waves, energy is not conserved. Instead, it is exchanged between waves of different wavevectors and frequencies, and between the waves and inhomogeneities. In this section, we introduce two models for one such inhomogeneity: large-scale, turbulent background flow in geostrophic and hydrostatic balance.

Large-scale motions in the atmosphere and ocean are dominated by layer-wise two-dimensional turbulence approximately in geostrophic and hydrostatic balance. Geostrophic balance occurs when the horizontal pressure gradient of the Boussinesq

equations balances the Coriolis effect. Then the momentum equation (1.3) becomes

$$f\boldsymbol{e}_z \times \boldsymbol{u}_h = -\boldsymbol{\nabla}_{\boldsymbol{x}_h} p, \tag{1.14}$$

where the h-subscript indicates horizontal quantities. Taking the curl of (1.14), we see that,

$$\boldsymbol{\nabla}_{\boldsymbol{x}_h} \cdot \boldsymbol{u}_h = 0, \tag{1.15}$$

which implies from the mass conservation equation (1.4)

$$\partial_z w = 0. \tag{1.16}$$

Therefore, we have two-dimensional, horizontal, non-divergent turbulence. This means the flow can be described by the stream function ψ,

$$\boldsymbol{u}_h = (-\partial_y \psi, \partial_x \psi, 0). \tag{1.17}$$

In the rotating shallow water system, geostrophy is a balance between the Coriolis effect and height gradient. Then, (1.9) becomes

$$f\boldsymbol{e}_z \times \boldsymbol{u}_h = -g\boldsymbol{\nabla}_{\boldsymbol{x}_h} \eta. \tag{1.18}$$

(The h-subscripts here are for ease of comparison with Boussinesq geostrophy (1.14), but are not necessary because the shallow water system is 2D.)

In fluid dynamics, the full governing fluid equations are rarely used. We have already made approximations to reach the Boussinesq and rotating shallow water models, neglecting terms such as viscosity which do not play a part on the length and time scales we consider in the atmosphere and ocean. We can make further assumptions on the size of terms in the Boussinesq and rotating shallow water models depending on location and the length and time scales we consider. Formally, this is done through non-dimensionalisation, then expansion in small parameters (see, for example, Vallis, 2017*b*).

We present two regimes for the Boussinesq and shallow water equations which

incorporate geostrophic turbulence. These are planetary geostrophy (PG) (e.g. Phillips, 1963) and the quasi-geostrophic regime (QG) (Charney, 1948). The scalings chosen to reach these regimes filter out IGWs entirely, instead describing a slowly evolving, large-scale background flow.

PG in the rotating shallow water system is a combination of geostrophic balance (1.18) and the mass conservation equation (1.10). Defining the characteristic flow velocity U_* and length scale L_*, it is characterised by small Rossby number

$$Ro = \frac{U_*}{L_* f}, \tag{1.19}$$

and motions above the Rossby radius of deformation,

$$L_D = \frac{(g\bar{H})^{1/2}}{f}. \tag{1.20}$$

This length scale describes the point at which rotation effects are as important as buoyancy effects. Equivalently, the Burger number

$$Bu = \left(\frac{L_D}{L_*}\right)^2 \tag{1.21}$$

is small.

PG for a Boussinesq system is, to leading order, geostrophic (1.14) and hydrostatic balance (1.12), the mass conservation equation (1.4) and the buoyancy equation (1.5). The scaling to reach these equations is the same as for the rotating shallow water system. Rossby number and Burger number are small, except Rossby radius of deformation takes the alternative form

$$L_D = \frac{\bar{N}\bar{H}}{f}, \tag{1.22}$$

where $\bar{H}$ is now the characteristic vertical length scale of the flow and $\bar{N}$ is the characteristic buoyancy frequency.

The atmosphere has a larger vertical scale than the ocean and in general, the ratio $\bar{N}/f$ is also higher in the atmosphere than the ocean ($O(10^2)$ versus $O(10)$ (e.g. Gill, 1982; Olbers, Willebrand & Eden, 2012*a*)). This means the horizontal scale L_D at which significant rotation effects occur is much greater in the atmosphere than

the ocean. For example, at mid-latitudes, $f = O(10^{-4})$ s^{-1} and in the upper ocean, $\bar{N} = O(10^{-2})$ s^{-1} and $\bar{H} = O(1)$ km (e.g. Vallis, 2017*b*). Then, $L_D = O(100)$ km by (1.22). In the atmosphere with the same buoyancy and Coriolis frequencies as used for the ocean and $\bar{H} = O(10)$ km, $L_D = O(1000)$ km.

For PG, the characteristic horizontal length scale of motion must be much greater than L_D. We can see from the typical atmospheric value of L_D that this means dynamics take place on the *planetary* scale i.e. of the order of the planet's radius. Over this scale in the atmosphere, the Coriolis parameter f varies significantly (see Vallis, 2017*b*). For PG to hold, f must be approximately constant and so PG has limited application in the atmosphere. It is more relevant in the ocean where L_D is typically smaller.

QG scaling is similar to the PG case: the Rossby number is small but the Burger number is $O(1)$. To leading order, the momentum equations of the shallow water and Boussinesq systems are geostrophic and hydrostatic balance. These equations are diagnostic and time independent – they describe how velocity is related to height or pressure, but not how each quantity evolves in time. Higher order terms in the perturbation analysis are required for closure and these result in a conservation equation for potential vorticity (which we omit here for brevity). This means that dynamically, QG contains significant ageostrophic and geostrophic motions whereas PG consists only of geostrophy (see Vallis, 2017*b*, for further details).

QG occurs at smaller horizontal scales than PG because the characteristic horizontal length scale of dynamics satisfies $L \sim L_D$ ($Bu = O(1)$). This is less restrictive than the PG scaling and so is more relevant to dynamics in the atmosphere and ocean. As L_D characterises the point at which rotation effects become as significant as buoyancy effects, the typical size of rotation-driven, large-scale geostrophic eddies in the atmosphere is significantly larger than in the ocean.

In summary, layer-wise two-dimensional, approximately geostrophic and hydrostatic turbulence is prevalent in the atmosphere and ocean. It dominates large-scale motions. It can be described by two simplified versions of the Boussinesq and rotating shallow water models: PG where $Ro \ll 1$ and $Bu \ll 1$ and; QG where $Ro \ll 1$ and $Bu \sim O(1)$.

1.4 WKB

Many theories exist to describe the interactions of waves and inhomogeneities and the distribution of wave energy in physical and spectral space. If the waves and inhomogeneities evolve on the same time and length scales, it is difficult to separate the two. We navigate this by considering waves in the WKB regime propagating on much shorter length and time scales than the inhomogeneities. Although we focus on IGWs and Poincaré waves scattered by background flows, the theory is applicable to all wave–inhomogeneity interactions in which a scale separation exists. A geophysical example of this is surface waves interacting with large-scale bottom topography.

The WKB approximation is named after Wentzel, Kramers and Brillouin (and Jeffreys if called WKBJ), the most recent pioneers of the technique (see, for example, Olbers, Willebrand & Eden, 2012*c*; Vallis, 2017*d*). They developed the method for linear differential equations with spatially/temporally varying coefficients in quantum mechanics such as the Schrödinger equation. In our framework, these coefficients are functions of the background flow which varies over larger length and time scales than the waves.

Consider this example ODE for $\zeta(t)$, adapted from Bender & Orszag (1999):

$$\epsilon^2 \frac{\mathrm{d}^2\zeta}{\mathrm{d}t^2} + Q(t)\zeta = 0, \quad \epsilon \ll 1, \tag{1.23}$$

where the variable coefficient $Q(t) > 0$. A WKB ansatz

$$\zeta = \zeta'(t)\mathrm{e}^{\mathrm{i}\Theta(t)/\epsilon}, \tag{1.24}$$

where primes denote the amplitude and Θ is the real phase function, and perturbation expansion of the amplitude

$$\zeta' = \zeta'_0 + \epsilon\zeta'_1 + O(\epsilon^2) \tag{1.25}$$

gives, after dividing through by the exponential,

$$\left(-\left(\frac{\mathrm{d}\Theta}{\mathrm{d}t}\right)^2 + Q(t)\right)\zeta'_0 = 0 \quad \Rightarrow \quad \Theta = \pm\int Q^{1/2}(x)\mathrm{d}t \tag{1.26}$$

at leading order in ϵ. At first order, again having divided through by the exponential,

$$\left(-\left(\frac{\mathrm{d}\Theta}{\mathrm{d}t}\right)^2 + Q(t)\right)\zeta_1' + \mathrm{i}\left(\frac{\mathrm{d}^2\Theta}{\mathrm{d}t^2}\zeta_0' + 2\frac{\mathrm{d}\Theta}{\mathrm{d}t}\frac{\mathrm{d}\zeta_0'}{\mathrm{d}t}\right) = 0. \tag{1.27}$$

The real part of this equation gives the same equation for the phase as leading order. The imaginary part can be solved via, for example, an integrating factor of $Q^{-1/4}/2$ to give the leading order amplitude ζ_0'. Then, the full leading order solution is

$$\zeta \approx \kappa_1 Q^{-1/4}(t)\exp\left(\frac{\mathrm{i}}{\epsilon}\int Q^{1/2}(t)\mathrm{d}t\right) + \kappa_2 Q^{-1/4}(t)\exp\left(-\frac{\mathrm{i}}{\epsilon}\int Q^{1/2}(t)\mathrm{d}t\right), \tag{1.28}$$

where κ_1 and κ_2 are arbitrary constants and we have superimposed the two opposite phase solutions. By using the WKB ansatz (1.24), we have approximated the solution to a highly oscillatory differential equation as a sum of slowly modulated, high-frequency plane waves.

In the remainder of this chapter, we replace the plane wave ansatz of §1.2 with a WKB ansatz to account for slowly varying background flows in the rotating shallow water system (1.9)–(1.10). The subsequent WKB analysis results in 1) a revision of the expressions for wave frequency in a homogeneous medium and; 2) a conservation equation describing the evolution of wave energy in physical and spectral space.

WKB scale separation between IGWs and the background flow is more well-justified in the atmosphere than the ocean and used extensively (e.g. Bölöni *et al.*, 2021; Kim *et al.*, 2021). This is because typical length scales of geostrophic eddies, characterised by L_D (1.22), are larger in the atmosphere due to larger values of $\bar{N}/f$ and typical characteristic vertical scales, as discussed in §1.3. Scale separation in the ocean is particularly weak for lower-mode internal tides but simulations relying on WKB techniques still perform surprisingly well (see Park & Watts, 2006; Rainville & Pinkel, 2006; Chavanne *et al.*, 2010).

The analysis we perform here is standard – see, for example, Achatz (2022) in the context of atmospheric IGWs. The novel part of our derivation is the inclusion of height variations induced by the background flow which are oftentimes neglected, for example, in Dong, Bühler & Smith (2020). These variations are induced by the geostrophic balance (1.18). This section is an adaption of appendix A of Cox *et al.*

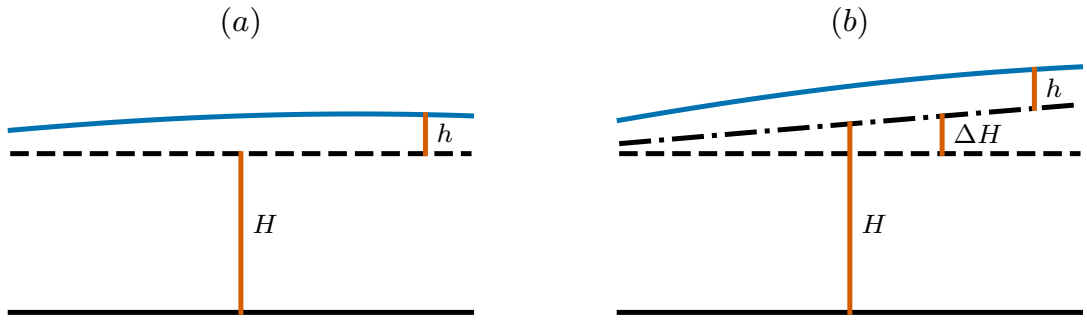

Figure 1.2: Sketch of flat-bottomed, shallow water set-up. In both panels, the free surface is the solid blue line, the flat bottom is the solid black line and the dashed black line is the constant mean height $\bar{H}$. The wave perturbations are given by h. The height of the layer in the absence of waves is H which is equal to $\bar{H}$ in panel (a) whilst in panel (b), it includes geostrophic height corrections ΔH, given by the dashed-dotted line.

(2024, under review).

We separate the fluid into a background flow component and a wave component,

$$\begin{pmatrix} \boldsymbol{u} \\ \eta \end{pmatrix} \rightarrow \begin{pmatrix} \boldsymbol{U} \\ H \end{pmatrix} + \begin{pmatrix} \boldsymbol{u} \\ h \end{pmatrix}, \tag{1.29}$$

where lowercase symbols now indicate wave variables and uppercase the background flow. Typically, the background flow height H is taken to be constant so that $H = \bar{H}$. This is shown in panel (a) of figure 1.2. We account for variations in height, shown in panel (b). The separation of background height into a constant part and varying part $H = \bar{H} + \Delta H$ is for use in later sections. The total flow and the background flow $(\boldsymbol{U}, H)^{\mathrm{T}}$ are solutions to the rotating shallow water equations (1.9)–(1.10).

We apply a WKB ansatz to the wave part,

$$\begin{pmatrix} \boldsymbol{u} \\ h \end{pmatrix} = \begin{pmatrix} \boldsymbol{u}'(\boldsymbol{X}, T) \\ h'(\boldsymbol{X}, T) \end{pmatrix} \mathrm{e}^{\mathrm{i}\Theta(\boldsymbol{X},T)/\epsilon}. \tag{1.30}$$

Here, we introduce the slow time and space scales $(\boldsymbol{X}, T) = \epsilon(\boldsymbol{x}, t)$, $\epsilon \ll 1$. The background flow $(\boldsymbol{U}(\boldsymbol{X}, T), H(\boldsymbol{X}, T))^{\mathrm{T}}$ and wave amplitudes, hereafter denoted by

$$\boldsymbol{\phi} = (\boldsymbol{u}', h')^{\mathrm{T}}, \tag{1.31}$$

evolve on these slow scales, whereas the wave phase Θ/ϵ evolves $O(1/\epsilon)$ quicker. We introduce the local wavevector and frequency

$$\boldsymbol{k} = (k_1, k_2)^{\mathrm{T}} = \boldsymbol{\nabla}_{\boldsymbol{X}}\Theta \quad \text{and} \quad \omega = -\partial_T\Theta, \tag{1.32a,b}$$

and expand the wave amplitudes in ϵ,

$$\boldsymbol{\phi}(\boldsymbol{X}, T) = \boldsymbol{\phi}_0 + \epsilon\boldsymbol{\phi}_1 + O(\epsilon^2) = \begin{pmatrix} \boldsymbol{u}_0' \\ h_0' \end{pmatrix} + \epsilon \begin{pmatrix} \boldsymbol{u}_1' \\ h_1' \end{pmatrix} + O(\epsilon^2). \tag{1.33}$$

In what follows, we drop the primes on the amplitudes $\boldsymbol{u}_0', h_0'$ etc. We look at terms linear in the wave phase.

At $O(1)$ in ϵ, momentum and mass conservation (1.9)–(1.10) become the right and left eigenvector problem

$$\mathrm{i}\boldsymbol{B}\boldsymbol{\mu}\boldsymbol{\phi}_0 = \mathrm{i}\omega_{\mathrm{in}}\boldsymbol{\phi}_0 \quad \text{and} \quad \boldsymbol{\phi}_0^{\dagger}\boldsymbol{\mu}\boldsymbol{B}\boldsymbol{\mu} = \boldsymbol{\phi}_0^{\dagger}\boldsymbol{\mu}\omega_{\mathrm{in}}, \tag{1.34a,b}$$

where

$$\boldsymbol{B} = \begin{pmatrix} 0 & \mathrm{i}f/H & k_1 \\ -\mathrm{i}f/H & 0 & k_2 \\ k_1 & k_2 & 0 \end{pmatrix} \quad \text{and} \quad \boldsymbol{\mu} = \begin{pmatrix} H & 0 & 0 \\ 0 & H & 0 \\ 0 & 0 & g \end{pmatrix}. \tag{1.35}$$

The form of the left eigenvector in (1.34a,b) is because $\boldsymbol{B}$ and $\boldsymbol{\mu}$ are Hermitian. Here, the intrinsic frequency ω_{in} is the frequency of the waves moving with the background flow,

$$\omega_{\mathrm{in}} = \omega - \boldsymbol{U}\cdot\boldsymbol{k}. \tag{1.36}$$

It is the difference between the total frequency and the Doppler shift $\boldsymbol{U}\cdot\boldsymbol{k}$. The Doppler shift term is a direct result of advection by the background flow, $\boldsymbol{U}\cdot\boldsymbol{\nabla}_{\boldsymbol{x}}$. The same term is introduced for IGWs in the Boussinesq system in the presence of a background flow.

The eigenvalues are

$$\omega_{\mathrm{in}} = 0, \pm(f^2 + gHk_h^2)^{1/2}. \tag{1.37}$$

The zero eigenvalue corresponds to the slowly evolving background flow mode and the non-zero eigenvalues are waves propagating with the same frequency as shallow water

waves in a homogeneous medium (1.11), but with variable background height H. Note that H can also include bottom topography.

Without loss of generality, we choose the positive intrinsic frequency eigenvalue so that the total frequency is

$$\omega = (f^2 + gHk_h^2)^{1/2} + \boldsymbol{U}\cdot\boldsymbol{k}. \tag{1.38}$$

To reiterate, at leading order, the background flow introduces height dependence into the intrinsic frequency, which it also Doppler shifts.

We consider the effect the inhomogeneities have on wave amplitude and thus energy distribution. The positive eigenvalue has the corresponding eigenvector

$$\boldsymbol{\phi}_0 = \frac{\alpha}{(Hk_h^2)^{1/2}\omega_{\text{in}}}\begin{pmatrix} \mathrm{i}fk_2 + k_1\omega_{\text{in}} \\ -\mathrm{i}fk_1 + k_2\omega_{\text{in}} \\ Hk_h^2 \end{pmatrix}, \tag{1.39}$$

where α is an $(\boldsymbol{X},\boldsymbol{k},T)$-dependent complex amplitude parameterising the eigenspace of $\boldsymbol{B\mu}$. Note that the α-independent part of the eigenvector is non-unique in that it can be rotated by a complex phase $\mathrm{e}^{\mathrm{i}\theta}$. The eigenvector (1.39) is normalised such that the square amplitude $|\alpha|^2$ corresponds to the energy density, $E(\boldsymbol{X},\boldsymbol{k},T)$,

$$\frac{1}{2}\boldsymbol{\phi}_0^\dagger\boldsymbol{\mu}\boldsymbol{\phi}_0 = \underbrace{\frac{H|\boldsymbol{u}_0|^2 + g|h_0|^2}{2}}_{E} = |\alpha|^2. \tag{1.40}$$

We seek an evolution equation for the energy density E.

At $O(\epsilon)$, the momentum and mass conservation equations (1.9)–(1.10) become

$$\mathcal{D}_U\boldsymbol{\phi}_0 + \begin{pmatrix} 0 & 0 & \partial_{X_1} \\ 0 & 0 & \partial_{X_2} \\ \partial_{X_1} & \partial_{X_2} & 0 \end{pmatrix}\boldsymbol{\mu}\boldsymbol{\phi}_0 + \begin{pmatrix} \partial_{X_1}U & \partial_{X_2}U & 0 \\ \partial_{X_1}V & \partial_{X_2}V & 0 \\ 0 & 0 & \boldsymbol{\nabla}_{\boldsymbol{X}}\cdot\boldsymbol{U} \end{pmatrix}\boldsymbol{\phi}_0 + \mathrm{i}(\boldsymbol{B\mu} - \omega_{\text{in}})\boldsymbol{\phi}_1 = 0, \tag{1.41}$$

where

$$\mathcal{D}_U = \partial_T + \boldsymbol{U}\cdot\boldsymbol{\nabla}_{\boldsymbol{X}}, \tag{1.42}$$

is the advective derivative with $\boldsymbol{U}$. We pre-multiply by the left eigenvector $\boldsymbol{\phi}_0^\dagger \boldsymbol{\mu}$ to remove the $\boldsymbol{\phi}_1$ term leaving

$$\underbrace{\boldsymbol{\phi}_0^\dagger \boldsymbol{\mu} \mathcal{D}_{\boldsymbol{U}} \boldsymbol{\phi}_0}_{①} + \underbrace{\boldsymbol{\phi}_0^\dagger \boldsymbol{\mu} \begin{pmatrix} 0 & 0 & \partial_{X_1} \\ 0 & 0 & \partial_{X_2} \\ \partial_{X_1} & \partial_{X_2} & 0 \end{pmatrix} \boldsymbol{\mu} \boldsymbol{\phi}_0}_{②} + \underbrace{\boldsymbol{\phi}_0^\dagger \boldsymbol{\mu} \begin{pmatrix} \partial_{X_1} U & \partial_{X_2} U & 0 \\ \partial_{X_1} V & \partial_{X_2} V & 0 \\ 0 & 0 & \boldsymbol{\nabla}_{\boldsymbol{X}} \cdot \boldsymbol{U} \end{pmatrix} \boldsymbol{\phi}_0}_{③} = 0. \quad (1.43)$$

We add the complex conjugate, divide by 2 and evaluate each term. Expanding term 1 and rearranging gives

$$\frac{1}{2}(①\text{+c.c.}) = \frac{1}{2}\left(\mathcal{D}_{\boldsymbol{U}}(H|\boldsymbol{u}_0|^2 + g|h_0^2|) - |\boldsymbol{u}_0|^2 \mathcal{D}_{\boldsymbol{U}} H\right) = \frac{1}{2}\mathcal{D}_{\boldsymbol{U}} E - \frac{1}{2}|\boldsymbol{u}_0|^2 \mathcal{D}_{\boldsymbol{U}} H, \quad (1.44)$$

where we use the normalisation (1.40) for the second equality. Using the product rule, term 2 becomes

$$\frac{1}{2}(② + \text{c.c.}) = \boldsymbol{\nabla}_{\boldsymbol{X}} \cdot (gH(\boldsymbol{u}_0^* h_0 + \boldsymbol{u}_0 h_0^*)/2) = \boldsymbol{\nabla}_{\boldsymbol{X}} \cdot (\boldsymbol{c}_{\text{in}} E), \quad (1.45)$$

where we use the explicit form of the eigenvector (1.39) to find

$$\frac{1}{2}(\boldsymbol{u}_0^* h_0 + \boldsymbol{u}_0 h_0^*) = \boldsymbol{k} E/\omega_{\text{in}} = \boldsymbol{c}_{\text{in}} E/(gH). \quad (1.46)$$

Here, we have introduced

$$\boldsymbol{c}_{\text{in}} = (\boldsymbol{\nabla}_{\boldsymbol{k}} \omega_{\text{in}})_{\boldsymbol{X},T} = \frac{gH\boldsymbol{k}}{\omega_{\text{in}}}, \quad (1.47)$$

the group velocity associated with the waves' intrinsic frequency. The $\boldsymbol{X}, T$ - subscript indicates that these variables are kept constant whilst taking the partial derivative, despite both being implicitly dependent on $\boldsymbol{k}$.

The final term is

$$\frac{1}{2}\left(③ + \text{c.c.}\right) = (H|\boldsymbol{u}_0|^2 + g|h_0|^2)\boldsymbol{\nabla}_{\boldsymbol{X}}\cdot\boldsymbol{U} - H(|u_0|^2\partial_{X_2}V + |v_0|^2\partial_{X_1}U) + \frac{1}{2}H(v_0u_0^* + v_0^*u_0)(\partial_{X_1}V + \partial_{X_2}U) \quad (1.48)$$

$$= E\left(2\boldsymbol{\nabla}_{\boldsymbol{X}}\cdot\boldsymbol{U} - \frac{\omega_{\text{in}}^2 - gHk_2^2}{\omega_{\text{in}}^2}\partial_{X_2}V - \frac{\omega_{\text{in}}^2 - gHk_1^2}{\omega_{\text{in}}^2}\partial_{X_1}U + \frac{gHk_1k_2}{\omega_{\text{in}}^2}(\partial_{X_1}V + \partial_{X_2}U)\right) \quad (1.49)$$

$$= E\left(\omega_{\text{in}}\boldsymbol{\nabla}_{\boldsymbol{X}}\cdot\boldsymbol{U} + \boldsymbol{k}\cdot(\boldsymbol{c}_{\text{in}}\cdot\boldsymbol{\nabla}_{\boldsymbol{X}}\boldsymbol{U})\right)/\omega_{\text{in}}, \quad (1.50)$$

where we use the normalisation (1.40) and

$$|u_0^2| = E\frac{\omega_{\text{in}}^2 - gHk_2^2}{H\omega_{\text{in}}^2}, \quad |v_0^2| = E\frac{\omega_{\text{in}}^2 - gHk_1^2}{H\omega_{\text{in}}^2}, \quad \text{and} \quad v_0u_0^* + v_0^*u_0^* = E\frac{2gk_1k_2}{\omega_{\text{in}}^2}, \quad (1.51\text{a,b,c})$$

derived from the eigenvector (1.39). All together, (1.43) becomes

$$0 = \mathcal{D}_{\boldsymbol{U}}(E) - \frac{1}{2}|\boldsymbol{u}_0|^2\mathcal{D}_{\boldsymbol{U}}H + \boldsymbol{\nabla}_{\boldsymbol{X}}\cdot(\boldsymbol{c}_{\text{in}}E) + E\left(\omega_{\text{in}}\boldsymbol{\nabla}_{\boldsymbol{X}}\cdot\boldsymbol{U} + \boldsymbol{k}\cdot(\boldsymbol{c}_{\text{in}}\cdot\boldsymbol{\nabla}_{\boldsymbol{X}}\boldsymbol{U})\right)/\omega_{\text{in}} \quad (1.52)$$

$$= \omega_{\text{in}}\left(\partial_T A + \boldsymbol{\nabla}_{\boldsymbol{X}}\cdot(\boldsymbol{c}_g A)\right) + A\left(\partial_T + \boldsymbol{c}_g\cdot\boldsymbol{\nabla}_{\boldsymbol{X}}\right)\omega_{\text{in}} - \frac{1}{2}|\boldsymbol{u}_0|^2\mathcal{D}_{\boldsymbol{U}}H + A\boldsymbol{k}\cdot(\boldsymbol{c}_{\text{in}}\cdot\boldsymbol{\nabla}_{\boldsymbol{X}}\boldsymbol{U}), \quad (1.53)$$

where

$$\boldsymbol{c}_g = \boldsymbol{c}_{\text{in}} + \boldsymbol{U}, \quad (1.54)$$

is the total group velocity and

$$A = E/\omega_{\text{in}}, \quad (1.55)$$

is wave action – the energy density normalised by the intrinsic frequency.

We introduce

$$\Omega(\boldsymbol{X}, \boldsymbol{k}(\boldsymbol{X}, T), T) = \omega(\boldsymbol{X}, T), \quad (1.56)$$

the total frequency with explicit $\boldsymbol{k}$ dependence. The eikonal equations are derived from

cross-derivatives of (1.32a,b),

$$(\partial_T + \boldsymbol{c}_g \cdot \boldsymbol{\nabla}_{\boldsymbol{X}})\omega \equiv \partial_T \Omega = \boldsymbol{k} \cdot \partial_T \boldsymbol{U} + (\partial_H \omega_{\text{in}})_{\boldsymbol{k}} \partial_T H, \tag{1.57}$$

and

$$(\partial_T + \boldsymbol{c}_g \cdot \boldsymbol{\nabla}_{\boldsymbol{X}})\boldsymbol{k} \equiv -\boldsymbol{\nabla}_{\boldsymbol{X}} \Omega = -\boldsymbol{k} \cdot (\boldsymbol{\nabla}_{\boldsymbol{X}} \boldsymbol{U}) - (\partial_H \omega_{\text{in}})_{\boldsymbol{k}} \boldsymbol{\nabla}_{\boldsymbol{X}} H. \tag{1.58}$$

To find derivatives of Ω, we have used the expression for total frequency ω (1.38). Note that $(\partial_H \omega_{\text{in}})_{\boldsymbol{k}}$ is the partial derivative of ω_{in} with respect to H with $\boldsymbol{k}$ fixed. Then, using (1.57)–(1.58),

$$\left(\partial_T + \boldsymbol{c}_g \cdot \boldsymbol{\nabla}_{\boldsymbol{X}}\right) \omega_{\text{in}} = \left(\partial_T + \boldsymbol{c}_g \cdot \boldsymbol{\nabla}_{\boldsymbol{X}}\right) \omega - \boldsymbol{U} \cdot \left(\partial_T + \boldsymbol{c}_g \cdot \boldsymbol{\nabla}_{\boldsymbol{X}}\right) \boldsymbol{k} - \boldsymbol{k} \cdot \left(\partial_T + \boldsymbol{c}_g \cdot \boldsymbol{\nabla}_{\boldsymbol{X}}\right) \boldsymbol{U} \tag{1.59}$$

$$= (\partial_H \omega_{\text{in}})_{\boldsymbol{k}} \partial_T H + (\partial_H \omega_{\text{in}})_{\boldsymbol{k}} \boldsymbol{U} \cdot \boldsymbol{\nabla}_{\boldsymbol{X}} H + \boldsymbol{k} \cdot (\boldsymbol{U} \cdot \boldsymbol{\nabla}_{\boldsymbol{X}} \boldsymbol{U}) - \boldsymbol{k} \cdot (\boldsymbol{c}_g \cdot \boldsymbol{\nabla}_{\boldsymbol{X}} \boldsymbol{U}) \tag{1.60}$$

$$= (\partial_H \omega_{\text{in}})_{\boldsymbol{k}} \mathcal{D}_{\boldsymbol{U}} H - \boldsymbol{k} \cdot (\boldsymbol{c}_{\text{in}} \cdot \boldsymbol{\nabla}_{\boldsymbol{X}} \boldsymbol{U}). \tag{1.61}$$

Substituting this result into (1.53) yields

$$\omega_{\text{in}} \left(\partial_T A + \boldsymbol{\nabla}_{\boldsymbol{X}} \cdot (\boldsymbol{c}_g A)\right) + A(\partial_H \omega_{\text{in}})_{\boldsymbol{k}} \mathcal{D}_{\boldsymbol{U}} H - \frac{1}{2}|\boldsymbol{u}_0|^2 \mathcal{D}_{\boldsymbol{U}} H = 0. \tag{1.62}$$

If the background flow is non-divergent flow, as is the case for the geostrophic flow we consider, then $\mathcal{D}_{\boldsymbol{U}} H = 0$ and, letting our book-keeping parameter $\epsilon = 1$,

$$\partial_t A + \boldsymbol{\nabla}_{\boldsymbol{x}} \cdot (\boldsymbol{c}_g A) = 0. \tag{1.63}$$

Otherwise, we have that

$$\partial_t A + \boldsymbol{\nabla}_{\boldsymbol{x}} \cdot (\boldsymbol{c}_g A) - \frac{f^2}{\omega_{\text{in}}^2} A \boldsymbol{\nabla}_{\boldsymbol{x}} \cdot \boldsymbol{U} = 0, \tag{1.64}$$

where we use the square components (1.51a,b,c) and

$$\partial_t H + \boldsymbol{U} \cdot \boldsymbol{\nabla}_{\boldsymbol{x}} H = -H \boldsymbol{\nabla}_{\boldsymbol{x}} \cdot \boldsymbol{U}, \tag{1.65}$$

which holds because the flow is a solution of the shallow equations (1.9)–(1.10).

For rotation effects to be significant in the dispersion relation of the shallow water waves, $1 \sim Bu(k_h/K_*)^2$ where Bu is the flow Burger number as defined by (1.21). Then, $f^2/\omega_{\text{in}}^2 = O(1)$. By the WKB ansatz, $k_h/K_* \gg 1$ and so $Bu \ll 1$. This is the planetary-geostrophy regime discussed in §1.3, whereby the scale of wave motion is much greater than the Rossby radius of deformation and the background flow is in geostrophic balance. Thus, the flow is non-divergent and (1.64) reduces to (1.63). If rotation effects are neglected, we have gravity waves and $f^2/\omega_{\text{in}}^2 \ll 1$. Therefore, in the WKB regime, the divergence term in (1.64) can always be neglected.

A consistent derivation for waves propagating with significant rotation f in a QG flow $Bu \sim O(1)$ is not possible. We defer to Bretherton (1971): "... when the physical situation is inappropriate, no amount of juggling will give a consistent, slowly varying wavetrain."

The conservation law (1.63) is for wave action $A(\boldsymbol{x}, t)$ defined through (1.40) and (1.55). It is coupled to the eikonal equation for $\boldsymbol{k}$, (1.58). It was first introduced by Bretherton & Garrett (1968).

The remainder of this derivation is standard and does not rely on the specific form of the dispersion relation. We closely follow §10.3.8 of Achatz (2022). For a conservation law that spans all of $(\boldsymbol{x}, \boldsymbol{k})$ space, we index each solution of (1.58) and (1.63) with the 2D parameter $\boldsymbol{\alpha}$ such that

$$\partial_t A_{\boldsymbol{\alpha}} + \boldsymbol{\nabla}_{\boldsymbol{x}} \cdot (\boldsymbol{c}_{g\boldsymbol{\alpha}} A_{\boldsymbol{\alpha}}) = 0 \quad \text{and} \quad (\partial_t + \boldsymbol{c}_{g\boldsymbol{\alpha}} \cdot \boldsymbol{\nabla}_{\boldsymbol{x}}) \boldsymbol{k}_{\boldsymbol{\alpha}} = -\boldsymbol{\nabla}_{\boldsymbol{x}} \Omega_{\boldsymbol{\alpha}}, \tag{1.66a,b}$$

and define the $\boldsymbol{k}$-dependent wave action density,

$$a(\boldsymbol{x}, \boldsymbol{k}, t) = \int A_{\boldsymbol{\alpha}}(\boldsymbol{x}, t) \delta(\boldsymbol{k} - \boldsymbol{k}_{\boldsymbol{\alpha}}) \mathrm{d}\boldsymbol{\alpha}, \tag{1.67}$$

a superposition of the individual solutions to the coupled equations. The time derivative

of the wave action density is

$$\partial_t a = \int \partial_t A_{\boldsymbol{\alpha}} \delta(\boldsymbol{k} - \boldsymbol{k}_{\boldsymbol{\alpha}}) \mathrm{d}\boldsymbol{\alpha} - \int A_{\boldsymbol{\alpha}} \partial_t \boldsymbol{k}_{\boldsymbol{\alpha}} \cdot \boldsymbol{\nabla}_{\boldsymbol{k}} \delta(\boldsymbol{k} - \boldsymbol{k}_{\boldsymbol{\alpha}}) \mathrm{d}\boldsymbol{\alpha}. \tag{1.68}$$

Then, by action conservation and the $\boldsymbol{k}_{\boldsymbol{\alpha}}$ eikonal equation (1.66a,b),

$$\partial_t a = -\int \left\{ \boldsymbol{\nabla}_{\boldsymbol{x}} \cdot (\boldsymbol{c}_{g\boldsymbol{\alpha}} A_{\boldsymbol{\alpha}}) \delta(\boldsymbol{k} - \boldsymbol{k}_{\boldsymbol{\alpha}}) - A_{\boldsymbol{\alpha}} (\boldsymbol{\nabla}_{\boldsymbol{x}} \Omega_{\boldsymbol{\alpha}} + \boldsymbol{c}_{g\boldsymbol{\alpha}} \cdot \boldsymbol{\nabla}_{\boldsymbol{x}} \boldsymbol{k}_{\boldsymbol{\alpha}}) \cdot \boldsymbol{\nabla}_{\boldsymbol{k}} \delta(\boldsymbol{k} - \boldsymbol{k}_{\boldsymbol{\alpha}}) \right\} \mathrm{d}\boldsymbol{\alpha}. \tag{1.69}$$

Next, we use $-\boldsymbol{c}_{g\boldsymbol{\alpha}} A_{\boldsymbol{\alpha}} \cdot \boldsymbol{\nabla}_{\boldsymbol{x}} \delta(\boldsymbol{k} - \boldsymbol{k}_{\boldsymbol{\alpha}}) = (\boldsymbol{c}_{g\boldsymbol{\alpha}} A_{\boldsymbol{\alpha}} \cdot \boldsymbol{\nabla}_{\boldsymbol{x}} \boldsymbol{k}_{\boldsymbol{\alpha}}) \cdot \boldsymbol{\nabla}_{\boldsymbol{k}} \delta(\boldsymbol{k} - \boldsymbol{k}_{\boldsymbol{\alpha}})$ to get

$$\partial_t a = -\int \left\{ \boldsymbol{\nabla}_{\boldsymbol{x}} \cdot (\boldsymbol{c}_{g\boldsymbol{\alpha}} A_{\boldsymbol{\alpha}} \delta(\boldsymbol{k} - \boldsymbol{k}_{\boldsymbol{\alpha}})) - A_{\boldsymbol{\alpha}} \boldsymbol{\nabla}_{\boldsymbol{x}} \Omega_{\boldsymbol{\alpha}} \cdot \boldsymbol{\nabla}_{\boldsymbol{k}} \delta(\boldsymbol{k} - \boldsymbol{k}_{\boldsymbol{\alpha}}) \right\} \mathrm{d}\boldsymbol{\alpha}. \tag{1.70}$$

Finally, we use the the δ function property,

$$\int f(\boldsymbol{k}_{\boldsymbol{\alpha}}) A_{\boldsymbol{\alpha}} \delta(\boldsymbol{k} - \boldsymbol{k}_{\boldsymbol{\alpha}}) \mathrm{d}\boldsymbol{\alpha} = f(\boldsymbol{k}) \int A_{\boldsymbol{\alpha}} \delta(\boldsymbol{k} - \boldsymbol{k}_{\boldsymbol{\alpha}}) \mathrm{d}\boldsymbol{\alpha}, \tag{1.71}$$

and that $\boldsymbol{\nabla}_{\boldsymbol{x}}$ and $\boldsymbol{\nabla}_{\boldsymbol{k}}$ are independent of $\boldsymbol{\alpha}$ to get

$$\partial_t a = -\boldsymbol{\nabla}_{\boldsymbol{x}} \cdot (\boldsymbol{\nabla}_{\boldsymbol{k}} \omega a) + \boldsymbol{\nabla}_{\boldsymbol{k}} \cdot (\boldsymbol{\nabla}_{\boldsymbol{x}} \omega a), \tag{1.72}$$

which can be written as the conservation equation for wave action density in $(\boldsymbol{x}, \boldsymbol{k})$ space,

$$\partial_t a + \boldsymbol{\nabla}_{\boldsymbol{k}} \omega \cdot \boldsymbol{\nabla}_{\boldsymbol{x}} a - \boldsymbol{\nabla}_{\boldsymbol{x}} \omega \cdot \boldsymbol{\nabla}_{\boldsymbol{k}} a = 0, \tag{1.73}$$

with total frequency (1.38). Here, we replace Ω by ω because, having summed over individual wave modes $\boldsymbol{\alpha}$, $\boldsymbol{k}$ and $\boldsymbol{x}$ are independent variables. We emphasise that the height $H(\boldsymbol{x}, t)$ is taken to vary on the same physical and temporal scales as the flow throughout this derivation.

The left-hand side of the action conservation equation (1.73) is the total derivative of $a(\boldsymbol{x}, \boldsymbol{k}, t)$ and contains a Poisson bracket $\{\omega, a\}$. In fact, ω is the Hamiltonian of the system and is conserved for any constant-action trajectory in $(\boldsymbol{x}, \boldsymbol{k})$ space. Hamilton's equations are the characteristic equations of (1.73) and describe rays of constant-action,

hence their name – the ray equations. They are,

$$\partial_t \boldsymbol{x} = \boldsymbol{\nabla}_{\boldsymbol{k}} \omega, \quad \text{and} \quad \partial_t \boldsymbol{k} = -\boldsymbol{\nabla}_{\boldsymbol{x}} \omega. \tag{1.74a,b}$$

The ray equations are used extensively in models of internal waves (e.g. Chavanne *et al.*, 2010; Dong *et al.*, 2020; Sebastia Saez, Eden & Chouksey, 2024).

The conservation law (1.73) describes the energy distribution of the waves through (1.55) and (1.67). The wave energy distribution in $(\boldsymbol{x}, \boldsymbol{k})$ space is

$$e(\boldsymbol{x}, \boldsymbol{k}, t) = \omega_{\text{in}}(\boldsymbol{x}, \boldsymbol{k}, t) a(\boldsymbol{x}, \boldsymbol{k}, t). \tag{1.75}$$

As previously remarked, the conservation equation for wave action density (1.73) holds for any waves interacting with larger scale, slowly evolving inhomogeneities such that the WKB approximation applies. In particular, in the presence of a background flow, IGWs described by the Boussinesq equations (1.3)–(1.5) satisfy (1.73) with a frequency

$$\omega = (f^2 \cos^2\theta + N^2 \sin^2\theta)^{1/2} + \boldsymbol{U} \cdot \boldsymbol{k}. \tag{1.76}$$

1.5 Scattering and induced spectral diffusion

In the limit of weak Doppler shift by a slowly evolving flow, the action conservation equation (1.73) and frequency (1.76) become a diffusion equation,

$$\partial_t a + \boldsymbol{c} \cdot \boldsymbol{\nabla}_{\boldsymbol{x}} a = \boldsymbol{\nabla}_{\boldsymbol{k}} \cdot (\boldsymbol{D} \cdot \boldsymbol{\nabla}_{\boldsymbol{k}} a)\,, \tag{1.77}$$

with the diffusivity in component form,

$$D_{ij} = k_m k_n \int_0^\infty \langle \partial_{x_i} U_m(\boldsymbol{x}, t) \partial_{x_j} U_n(\boldsymbol{x} - \boldsymbol{c}s, t - s) \rangle \, \mathrm{d}s. \tag{1.78}$$

This is valid for the Boussinesq system with constant buoyancy frequency N. In this case, the diffusivity is a 3×3 tensor. For the rotating shallow water system with frequency (1.38) and a constant height $H = \bar{H}$, the diffusivity (1.78) is a 2×2 tensor. The diffusivity (1.78) does not take into account height variations or variations in

buoyancy.

The diffusivity (1.78) was introduced by McComas & Bretherton (1977) in the context of short waves interacting with long, slowly evolving waves. They note that the diffusivity also holds for short waves propagating in a low-frequency current. Initial discussions on flow-induced diffusivities are contained in Müller & Olbers (1975); Müller (1976, 1977).

Diffusion is a subclass of scattering. Scattering is the process of repeated weak interactions between waves and slowly evolving inhomogeneities resulting in the redistribution of wave energy in spectral space (e.g. Hasselmann, 1966; Ryzhik, Papanicolaou & Keller, 1996; Eden, Pollmann & Olbers, 2019). It is described by Boltzmann-like kinetic equations derived from the governing equations of the fluid (e.g. the Boussinesq equations (1.3)–(1.5)) and individual interactions can be described by Feynman diagrams (Hasselmann, 1966).

McComas & Bretherton (1977) provide two derivations for the diffusion equation (1.77). The first begins with a kinetic equation for resonant wave-wave interactions. These so-called triadic interactions preserve the combined frequencies and wavevectors of scattering constituents. Let the incident wavevectors and frequencies be denoted by subscripts $1, 2$ and the resultant wave have subscript 3. Then,

$$\boldsymbol{k}_1 + \boldsymbol{k}_2 = \boldsymbol{k}_3 \quad \text{and} \quad \omega_1 + \omega_2 = \omega_3, \tag{1.79a,b}$$

where we use the convention $\omega_i > 0$.

To reach the diffusion equation (1.77), McComas & Bretherton (1977) take the limit of their kinetic equation for a field of high-frequency, short incident waves being scattered by long, low-frequency waves. The physical scale separation here is equivalent to the WKB regime. Then, $\omega_2 \ll \omega_1 \approx \omega_3$ and $|\boldsymbol{k}_2| \ll |\boldsymbol{k}_1| \approx |\boldsymbol{k}_3|$. Savva (2020) shows that (1.77) is the WKB limit of a kinetic equation describing waves being scattered by a slowly evolving background flow, first described in Savva, Kafiabad & Vanneste (2021).

As the WKB limit of scattering, diffusion equations can also be derived from conservation of wave action. McComas & Bretherton (1977) provide an alternative derivation for the diffusion equation (1.77) starting with the ray equations (1.74a,b).

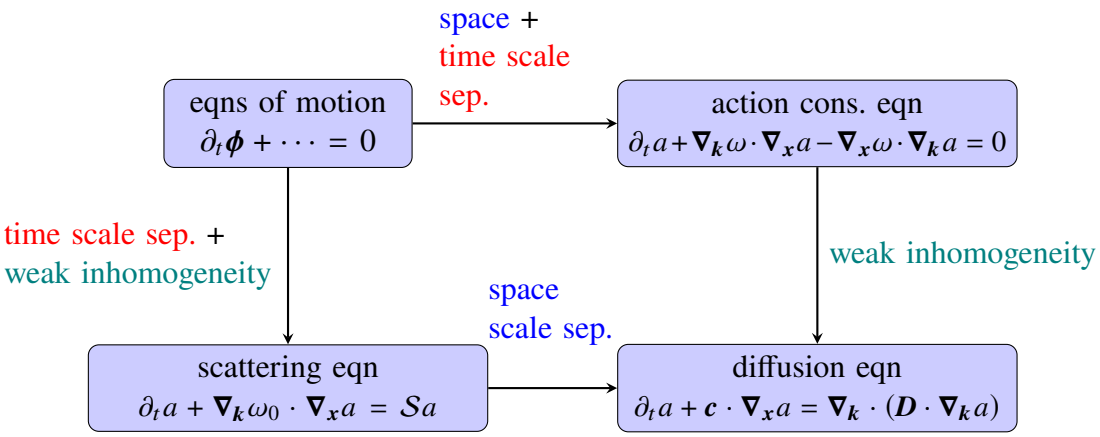

Figure 1.3: Diagram demonstrating necessary assumptions to reach various approximations of the governing equations. Here, $\boldsymbol{\phi}$ is a vector of fluid variables, a is wave action, ω is the total frequency of the waves, ω_0 is the leading order, inhomogeneity-free part of the frequency (later termed the bare frequency) and $\boldsymbol{c} = \boldsymbol{\nabla}_{\boldsymbol{x}}\omega_0$ is the leading order group velocity of the waves. The right-hand side of the scattering equation, $\mathcal{S}$, is a scattering integral of a. This scattering integral reduces to a diffusivity under the WKB approximation.

Kafiabad *et al.* (2019, hereafter KSV) obtain the same result through applying matched asymptotics to the action conservation equation (1.73) but instead of wave-wave interactions, they consider waves scattered by a large-scale, low-frequency background flow. The assumptions to move between the governing equations, wave action conservation, scattering and diffusion are summarised in figure 1.3.

Both papers presented in this thesis (§2, §3) build upon the results of KSV, which we now summarise.

In KSV, the diffusion equation is derived for a time-independent background flow. As a direct result of the flow's time independence, wave action is confined to constant-frequency surfaces – cones (see figure 1.1) – in spectral space. As frequency is unchanged, this means energy is also constrained to cones of constant frequency by (1.75). This can be interpreted through resonant triads as a catalytic interaction between a high-frequency, short wave and zero-frequency, large-scale background flow, resulting in a scattered wave of the same frequency propagating with a modified wavevector. No energy is exchanged between the waves and flow.

KSV solve the diffusion equation (1.77) for an initial value problem of waves excited at a single wavenumber and frequency. The result is a cascade of energy to higher wavenumbers along the cone of constant frequency. With forcing at a single

wavenumber and frequency, the equilibrium solution is found to behave as the power law k^{-2}, where k is the radial wavenumber. This predicted slope is consistent with observed wave energy spectra in the ocean and atmosphere.

These predictions are supported by simulations of the Boussinesq equations (1.3)–(1.4) in which wave energy is found to remain close to the cone of initial/forcing frequency, despite the background flow being slowly time dependent. This supports the assumption of KSV that if the flow is sufficiently slow in its evolution, it can be considered stationary.

KSV mention that a degree of caution should be taken when applying their results to the atmosphere. This is because background flows can be very high speed and directional, violating the assumption of a weak, statistically homogeneous flow which their analysis relies on. They derive an energy spectrum for IGWs but the concept of an energy spectrum may be ill-defined in the atmosphere because of the short-lived nature of atmospheric waves. In §2.5, we discuss the limitations of the diffusion approximation used in KSV – namely, where the weak interaction approximation breaks down.

The diffusivity derivation presented in KSV provides a clear method for reaching diffusion equations of the form (1.77) from the action conservation equation with weak interactions between waves and inhomogeneities. The derivation is adapted to include time-dependent flow in a rotating shallow water system by Dong *et al.* (2020). For surface waves scattered by background currents, the derivation is adapted by Villas Bôas & Young (2020), with intermediate results from the matched asymptotics used to predict wave height (Wang *et al.*, 2023). Yang *et al.* (2023) investigate diffusion in a realistic ocean simulation.

The work of Dong *et al.* (2020) raises questions regarding flow time dependence. They use ray tracing to explore the effect of flow time dependence on Poincaré waves and find significant diffusion of action and energy across the constant-frequency surface – a circle in two dimensions – in wavevector space. This suggests rather than the flow scattering the waves in a catalytic interaction, the flow enables energy exchange between waves of different frequencies. Will the same cross-frequency diffusion occur for the three-dimensional system? This is the question our first paper, §2, answers.

We relax the assumption of flow time dependence and adapt the results of KSV to a time-dependent flow. The main result of the paper is the adapted equilibrium spectrum

for wave energy which quantifies the spread of energy in frequency space due to the flow time dependence. We find the spread is negligible, justifying the assumption of flow time independence and showing resonant interactions between waves of the same frequency dominate in the diffusion regime.

It is also assumed in KSV; Dong *et al.* (2020); Villas Bôas & Young (2020) that the background flow affects the waves only through Doppler shift. In deriving the shallow water action conservation equation (1.73), we allow for height variations induced by the background flow. Analogously, in the Boussinesq system, buoyancy fluctuations are induced by the flow. These height and buoyancy fluctuations in the wave frequency result in corrections to the diffusivity (1.78). In fact, any inhomogeneity-induced correction to the constant part of the wave frequency results in a diffusivity correction. In §3, we generalise the induced-diffusion framework of McComas & Bretherton (1977) and KSV to account for any inhomogeneity the wave encounters.

Chapter 2

Inertia-gravity-wave diffusion by geostrophic turbulence: the impact of flow time dependence

This chapter is adapted from the paper of the same name published in the Journal of Fluid Mechanics (Cox, Kafiabad & Vanneste, 2023). The paper is included in its entirety, with an additional section and two appendices: §2.6 is a discussion on the width of IGW spectral peaks; §A.1 provides a method for computing all corrections to the diffusivity induced by a time-dependent flow, not only $D_{\theta\theta}$ presented in the paper and; §A.2 confirms in the time-independent flow limit, our predicted wave energy spectrum reduces to the spectrum of KSV. §2.5 appears in the published paper as an appendix but is included here in the main body of text after the discussion. We stress that ω in this chapter denotes the intrinsic frequency, not the absolute frequency as it does in other parts of this thesis. Capital Ω denotes the flow frequency, which is the case elsewhere.

The Boussinesq simulation presented in §2.3.2 is the work of Hossein A. Kafiabad alone. The remainder of the paper, including the analysis using the simulation data, is a collaborative work between the authors.

2.1 Introduction

Atmospheric and oceanic inertia-gravity waves (IGWs) propagate in a complex turbulent flow which is in approximately geostrophic and hydrostatic balance. The inhomogeneities of this flow result in the scattering of IGWs which redistributes their energy across wavevector space. This process has long been thought to play a role in the energetics of the atmosphere and ocean and it has been modelled using a range of approximations (see Müller, 1976, 1977; Watson, 1985; Müller, Holloway, Henyey & Pomphrey, 1986; Savva, Kafiabad & Vanneste, 2021; Young, 2021).

Kafiabad, Savva & Vanneste (2019, hereafter KSV) used multiscale asymptotics to show that the wave-action of linear IGWs propagating in a steady random geostrophic flow of much larger spatial scale evolves according to the diffusion equation

$$\partial_t a + \boldsymbol{c} \cdot \boldsymbol{\nabla}_{\boldsymbol{x}} a = \boldsymbol{\nabla}_{\boldsymbol{k}} \cdot (\boldsymbol{D} \cdot \boldsymbol{\nabla}_{\boldsymbol{k}} a) + F. \tag{2.1}$$

Here $a(\boldsymbol{x}, \boldsymbol{k}, t)$ is the wave-action density in the $(\boldsymbol{x}, \boldsymbol{k})$ phase space, $\boldsymbol{k}$ is the wavevector, $\boldsymbol{c} = \boldsymbol{\nabla}_{\boldsymbol{k}}\omega$ is the intrinsic group velocity of IGWs, and $F(\boldsymbol{x}, \boldsymbol{k}, t)$ is a forcing term. The IGW intrinsic frequency

$$\omega = (f^2 \cos^2\theta + N^2 \sin^2\theta)^{1/2}, \tag{2.2}$$

with $f < N$ the Coriolis and buoyancy frequencies, depends on the angle θ between $\boldsymbol{k}$ and the vertical. The $\boldsymbol{k}$-dependent diffusivity tensor $\boldsymbol{D}$ is given in components by

$$D_{ij} = k_m k_n \int_0^\infty \langle \partial_{x_i} U_n(\boldsymbol{x}) \partial_{x_j} U_m(\boldsymbol{x} - \boldsymbol{c}s) \rangle \, \mathrm{d}s, \tag{2.3}$$

where $\langle \cdot \rangle$ denotes ensemble average and $\boldsymbol{U}$ is the flow velocity field, with prescribed homogeneous statistics. A striking prediction of the diffusion equation (2.1) is that forced IGWs have a stationary spectrum scaling with wavenumber as k^{-2}, consistent with observed atmospheric mesoscale spectra (Gage & Nastrom, 1986; Lindborg, 1999) and oceanic submesoscale spectra (Callies & Ferrari, 2013). This provides support to the interpretation of the dynamics in these ranges as dominated by almost linear IGWs (Dewan, 1979; VanZandt, 1982; Bühler *et al.*, 2014; Callies *et al.*, 2014, 2016). (The

nature of the dynamics and level of nonlinearity in the atmospheric mesoscales is still a subject of debate; see Li & Lindborg (2018) and references therein for a contrasting view.)

Crucially, the assumption of time-independent flow implies that the diffusivity tensor satisfies $\boldsymbol{D} \cdot \boldsymbol{c} = 0$, as shown in KSV. Thus, noting $\boldsymbol{D}$ is symmetric, the diffusive flux $\boldsymbol{D} \cdot \boldsymbol{\nabla}_{\boldsymbol{k}} a$ is perpendicular to $\boldsymbol{c} = \boldsymbol{\nabla}_{\boldsymbol{k}} \omega$ and hence the diffusion of wave action is restricted to a constant-frequency surface, namely a cone $\theta = \text{const}$. This prediction is the direct consequence of the assumed linearity and time independence. Simulations of the nonlinear Boussinesq equations reported by KSV nonetheless indicate that it applies to a good approximation to small-Rossby-number flows, because their time scale is asymptotically larger than the IGW propagation time scale. This is illustrated in figure 2.1 which shows the result of a forced nonlinear Boussinesq simulation similar to KSV's (see §2.3.2 for details): the energy density in wavevector space is confined close to the constant-θ cone corresponding to the forcing frequency.

However, Dong, Bühler & Smith (2020) suggest that the slow diffusion of wave action across constant-frequency surfaces that results from slow flow time dependence causes significant transfer of wave action from low to high frequency and demonstrate this for IGWs in rotating shallow water. The relevance of this result to three-dimensional IGWs is unclear. It is therefore an open question whether flow time dependence can radically alter the phenomenology of IGW diffusion by geostrophic turbulence, possibly on time scales much longer than the length of the simulations reported in KSV and in figure 2.1.

We address this question in this paper by revisiting KSV to account for the slow time dependence of the geostrophic flow. Our starting point is the McComas & Bretherton (1977) diffusivity

$$D_{ij} = k_m k_n \int_0^\infty \langle \partial_{x_i} U_n(\boldsymbol{x}, t) \partial_{x_j} U_m(\boldsymbol{x} - \boldsymbol{c}s, t - s) \rangle \, \mathrm{d}s, \tag{2.4}$$

which applies to flows with arbitrary time dependence and was originally derived for wave–wave interactions in the induced diffusion regime. This diffusivity reduces to (2.3) in the time-independent case. (See Dong *et al.* (2020) for a derivation using multiscale asymptotics.) Under the assumption of slow time dependence, encapsulated

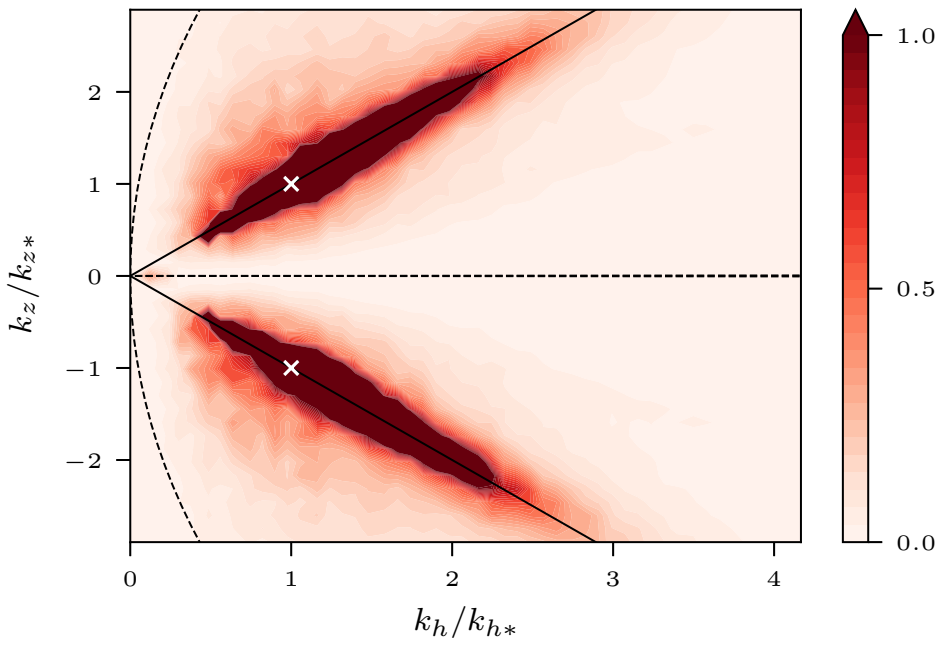

Figure 2.1: IGW energy spectrum e as a function of the horizontal and vertical wavenumbers (k_h, k_z) in the forced Boussinesq simulation described in §2.3.2. The wavenumbers are scaled by the forcing wavenumbers (k_{h*}, k_{z*}) indicated by the white crosses. The cone corresponding to the forcing frequency is indicated by the solid lines. The energy e is re-scaled by a characteristic value. The dashed lines indicate the boundary of the region of validity of the diffusion approximation (see §2.5).

by a small parameter ϵ – the ratio of the geostrophic flow velocity to the IGW group speed – we approximate (2.4) and solve the associated diffusion equation asymptotically to obtain the equilibrium action distribution resulting from a steady single-frequency forcing. The results show that the action remains localised within an $O(\epsilon)$-thick boundary layer around the cone corresponding to the forcing frequency. This indicates that the diffusion of three-dimensional IGWs is largely unaffected by the slow time dependence of geostrophic turbulence. In particular, the k^{-2} equilibrium spectrum found by KSV can be recovered by integration of the solution across the boundary layer. We confirm the main theoretical predictions by comparison with a high-resolution simulation of the nonlinear Boussinesq equations as shown in figure 2.1.

2.2 Approximation of the diffusivity tensor

In this section we approximate the diffusivity in (2.4) taking advantage of the slow time dependence of the geostrophic flow. Introducing the velocity correlation tensor $\Pi_{mn}(\boldsymbol{y}, s) = \langle U_m(\boldsymbol{x}+\boldsymbol{y}, t+s)U_n(\boldsymbol{x}, t)\rangle$ we rewrite (2.4) as

$$D_{ij} = -\frac{1}{2}k_m k_n \int_{-\infty}^{\infty} \frac{\partial^2 \Pi_{mn}}{\partial y_i \partial y_j}(\boldsymbol{c}s, s)\,\mathrm{d}s, \tag{2.5}$$

where we extend the integration range to $(-\infty, \infty)$ using that $k_m k_n \Pi_{mn}(-\boldsymbol{c}s, -s) = k_m k_n \Pi_{mn}(\boldsymbol{c}s, s)$. In terms of the wavevector–frequency spectrum $\hat{\Pi}_{mn}$ defined via the Fourier transform

$$\Pi_{mn}(\boldsymbol{x}, t) = \int_{\mathbb{R}^4} \hat{\Pi}_{mn}(\boldsymbol{K}, \Omega)\mathrm{e}^{\mathrm{i}(\boldsymbol{K}\cdot\boldsymbol{x}-\Omega t)}\,\mathrm{d}\boldsymbol{K}\mathrm{d}\Omega \tag{2.6}$$

this becomes

$$D_{ij} = \pi k_m k_n \int_{\mathbb{R}^4} K_i K_j \hat{\Pi}_{mn}(\boldsymbol{K}, \Omega)\delta(\boldsymbol{K}\cdot\boldsymbol{c} - \Omega)\,\mathrm{d}\boldsymbol{K}\mathrm{d}\Omega \tag{2.7}$$

on using $\int_{\mathbb{R}} \mathrm{e}^{\mathrm{i}(\boldsymbol{K}\cdot\boldsymbol{c}-\Omega)s}\,\mathrm{d}s = 2\pi\delta(\boldsymbol{K}\cdot\boldsymbol{c} - \Omega)$. Using the spherical polar coordinates (k, θ, ϕ) for $\boldsymbol{k}$ and (K, Θ, Φ) for $\boldsymbol{K}$ (lowercase symbols for IGW $\boldsymbol{k}$-space and uppercase

symbols for geostrophic flow $\boldsymbol{K}$-space), we compute

$$k_m k_n \hat{\Pi}_{mn}(\boldsymbol{K}, \Omega) = (k_1 K_2 - k_2 K_1)^2 E_\psi(\boldsymbol{K}, \Omega) = 2k^2 \sin^2\theta \sin^2\gamma E(\boldsymbol{K}, \Omega), \tag{2.8}$$

where E_ψ is the spectrum of the stream function ψ of the geostrophic flow (that is, the Fourier transform of $\langle \psi(\boldsymbol{x}+\boldsymbol{y}, t+s)\psi(\boldsymbol{x}, t)\rangle$),

$$\gamma = \Phi - \phi, \tag{2.9}$$

and $E(\boldsymbol{K}, \Omega) = K^2 \sin^2\Theta E_\psi/2$ is the geostrophic flow kinetic-energy spectrum. Substituting (2.8)–(2.9) into (2.7) yields

$$D_{ij} = 2\pi k^2 \sin^2\theta \int_{\mathbb{R}^4} K_i K_j \sin^2\gamma E(\boldsymbol{K}, \Omega)\delta(\boldsymbol{K}\cdot\boldsymbol{c} - \Omega)\,\mathrm{d}\boldsymbol{K}\mathrm{d}\Omega. \tag{2.10}$$

Following KSV, we assume that the flow is isotropic in the horizontal so that $E(\boldsymbol{K}, \Omega)$ is independent of Φ. In spherical polar coordinates, several components of $\boldsymbol{D}$ vanish. To see this, we replace Φ by γ as an integration variable in (2.10) and express $\boldsymbol{K}$ in the local spherical basis $(\boldsymbol{e}_k, \boldsymbol{e}_\theta, \boldsymbol{e}_\phi)$ associated with $\boldsymbol{k}$. Thus we write

$$\boldsymbol{K} = K\sin\Theta\left((\sin\theta\cos\gamma + \cot\Theta\cos\theta)\boldsymbol{e}_k + (\cos\theta\cos\gamma - \cot\Theta\sin\theta)\boldsymbol{e}_\theta + \sin\gamma\boldsymbol{e}_\phi\right). \tag{2.11}$$

We can now use the parity of the integrand with respect to γ in (2.10), noting that $\delta(\boldsymbol{K}\cdot\boldsymbol{c} - \Omega)$ is even since $\boldsymbol{c} = \boldsymbol{\nabla}_{\boldsymbol{k}}\omega(\theta)$ implies that $\boldsymbol{c} \parallel \boldsymbol{e}_\theta$ hence $\boldsymbol{K}\cdot\boldsymbol{c} = \boldsymbol{e}_\theta\cdot\boldsymbol{K}\,c$. The parity of the integrands giving the components $D_{kk} = \boldsymbol{e}_k\cdot\boldsymbol{D}\cdot\boldsymbol{e}_k$, etc. of $\boldsymbol{D}$ is then determined by the parity of pairwise products of $\boldsymbol{e}_k\cdot\boldsymbol{K}$, $\boldsymbol{e}_\theta\cdot\boldsymbol{K}$ and $\boldsymbol{e}_\phi\cdot\boldsymbol{K}$. We conclude from this that the only non-zero components of $\boldsymbol{D}$ are $D_{kk}, D_{k\theta} = D_{\theta k}, D_{\theta\theta}$, and $D_{\phi\phi}$. Thus, diffusion in the azimuthal direction depends only on azimuthal gradients of action and is decoupled from the k and θ directions.

We now restrict our attention to flows that are slowly time dependent in the sense that their typical frequencies Ω and wavevectors $\boldsymbol{K}$ satisfy $\Omega \ll \boldsymbol{K}\cdot\boldsymbol{c}$. For realistic turbulent flows, $\Omega \sim UK$, hence this condition is equivalent to the condition $U \ll c$ that underpins the diffusion approximation (2.1), the limitation of which is discussed in

§2.5. To make the smallness of Ω relative to $\boldsymbol{K}\cdot\boldsymbol{c}$ explicit, we introduce a bookkeeping parameter $\epsilon \ll 1$ to mark out asymptotically small terms. The delta function $\delta(\boldsymbol{K}\cdot\boldsymbol{c}-\Omega)$ in (2.10) becomes $\delta(\boldsymbol{K}\cdot\boldsymbol{c}-\epsilon\Omega)$ and can be expanded as

$$\delta(\boldsymbol{K}\cdot\boldsymbol{c}-\epsilon\Omega) = \delta(\boldsymbol{K}\cdot\boldsymbol{c}) - \epsilon\delta'(\boldsymbol{K}\cdot\boldsymbol{c})\Omega + \epsilon^2\delta''(\boldsymbol{K}\cdot\boldsymbol{c})\Omega^2/2 + O(\epsilon^3). \tag{2.12}$$

Using this alongside the evenness of $E(\boldsymbol{K},\Omega)$ in Ω leads to the approximation

$$\boldsymbol{D} = \boldsymbol{D}^{(0)} + \epsilon^2\boldsymbol{D}^{(1)} + O(\epsilon^4). \tag{2.13}$$

Here

$$D^{(0)}_{ij} = 2\pi k^2 \sin^2\theta \int_{\mathbb{R}^3} K_i K_j \sin^2\gamma E(\boldsymbol{K})\delta(\boldsymbol{K}\cdot\boldsymbol{c})\,\mathrm{d}\boldsymbol{K}, \tag{2.14}$$

where $E(\boldsymbol{K})$ is the geostrophic flow kinetic energy spectrum marginalised over frequencies, recovers the diffusivity of time-independent flows obtained by KSV (up to a factor $(2\pi)^3$ corresponding to a different Fourier transform convention, see (2.6)). For a horizontally isotropic geostrophic flow, $D^{(0)}_{ij}$ has two non-zero components in spherical polar coordinates, namely

$$D^{(0)}_{kk} = \frac{4\pi k^3\omega\sin^2\theta}{(N^2-f^2)|\cos^5\theta|}\int_0^\infty\int_\theta^{\pi-\theta} K^3\cos^2\Theta(\cot^2\theta-\cot^2\Theta)^{1/2}E(K,\Theta)\,\mathrm{d}K\mathrm{d}\Theta, \tag{2.15a}$$

$$D^{(0)}_{\phi\phi} = \frac{4\pi k^3\omega\sin^4\theta}{(N^2-f^2)|\cos^5\theta|}\int_0^\infty\int_\theta^{\pi-\theta} K^3\sin^2\Theta(\cot^2\theta-\cot^2\Theta)^{3/2}E(K,\Theta)\,\mathrm{d}K\mathrm{d}\Theta. \tag{2.15b}$$

(These equations are (A 13) in KSV, up to the $(2\pi)^3$ factor and typographical corrections in the lower limits of Θ and K.)

The leading-order correction to (2.14) induced by the slow flow time dependence is

$$D^{(1)}_{ij} = \pi k^2 \sin^2\theta \int_{\mathbb{R}^3} K_i K_j \sin^2\gamma A(\boldsymbol{K})\delta''(\boldsymbol{K}\cdot\boldsymbol{c})\,\mathrm{d}\boldsymbol{K}, \tag{2.16}$$

and depends on the geostrophic-flow acceleration spectrum

$$A(\boldsymbol{K}) = \int_{\mathbb{R}} E(\boldsymbol{K}, \Omega)\Omega^2 \, \mathrm{d}\Omega, \tag{2.17}$$

a natural measure of the flow's unsteadiness.

We have shown by parity arguments that the non-zero components of $\boldsymbol{D}$ are $D_{kk}, D_{k\theta} = D_{\theta k}, D_{\theta\theta}$, and $D_{\phi\phi}$. Of these components, only D_{kk} and $D_{\phi\phi}$ are non-zero to leading order. The corresponding correction components, $D^{(1)}_{kk}$ and $D^{(1)}_{\phi\phi}$, are never significant because they are $O(\epsilon^2)$ smaller than the leading order terms. For the other non-zero corrections, $D^{(1)}_{k\theta} = D^{(1)}_{\theta k}$ and $D^{(1)}_{\theta\theta}$, to appear at the same order as $D^{(0)}_{kk}$ and $D^{(0)}_{\phi\phi}$ in the diffusion equation, action must be rapidly changing with θ so that the θ derivatives are large. In the diffusion equation, $D^{(1)}_{\theta\theta}$ appears with two θ derivatives, whereas $D^{(1)}_{k\theta} = D^{(1)}_{\theta k}$ appears with one. This means $D^{(1)}_{\theta\theta}$, corresponding to across-cone diffusion, will always be an order of magnitude larger than the $D^{(1)}_{\theta k} = D^{(1)}_{k\theta}$ and therefore is the only dynamically significant component of $\boldsymbol{D}^{(1)}$. (In appendix A.1, not included in the published paper, we present a general method for evaluating all components of the diffusivity correction (2.16).)

Contracting (2.16) twice with $\boldsymbol{e}_\theta = \boldsymbol{c}/c$, we obtain

$$D^{(1)}_{\theta\theta} = \frac{\boldsymbol{c} \cdot \boldsymbol{D}^{(1)} \cdot \boldsymbol{c}}{c^2} = \frac{\pi k^2 \sin^2\theta}{c^2} \int_{\mathbb{R}^3} (\boldsymbol{K} \cdot \boldsymbol{c})^2 \sin^2\gamma A(\boldsymbol{K}) \delta''(\boldsymbol{K} \cdot \boldsymbol{c}) \, \mathrm{d}\boldsymbol{K}. \tag{2.18}$$

Noting that

$$\int_{\mathbb{R}} x^2 f(x) \delta''(x) \, \mathrm{d}x = 2 \int_{\mathbb{R}} f(x)\delta(x) \, \mathrm{d}x \tag{2.19}$$

for any smooth $f(x)$ reduces (2.18) to

$$D^{(1)}_{\theta\theta} = \frac{2\pi k^2 \sin^2\theta}{c^2} \int_{\mathbb{R}^3} \sin^2\gamma A(\boldsymbol{K}) \delta(\boldsymbol{K} \cdot \boldsymbol{c}) \, \mathrm{d}\boldsymbol{K}. \tag{2.20}$$

Representing $\boldsymbol{K}$ in the polar spherical coordinates (K, Θ, γ) and expanding $\boldsymbol{K} \cdot \boldsymbol{c}$ using

(2.11) gives

$$D^{(1)}_{\theta\theta} = \frac{2\pi k^2 \sin^2\theta}{c^2} \int_0^\infty \mathrm{d}K \int_0^\pi \mathrm{d}\Theta \int_{-\pi}^{\pi} \mathrm{d}\gamma\, K^2 \sin\Theta \sin^2\gamma A(K,\Theta) \times \delta\left(Kc \sin\Theta\cos\theta\left(\cos\gamma - \frac{\cot\Theta}{\cot\theta}\right)\right), \tag{2.21}$$

where we use horizontal isotropy to write $A(\boldsymbol{K}) = A(K,\Theta)$. Under the change of variable $\zeta = \cos\gamma$ this simplifies into

$$D^{(1)}_{\theta\theta} = \frac{4\pi k^2 \sin^2\theta}{c^3|\cos\theta|} \int_0^\infty \mathrm{d}K \int_0^\pi \mathrm{d}\Theta \int_{-1}^{1} \mathrm{d}\zeta\, K(1-\zeta^2)^{1/2} A(K,\Theta)\delta\left(\zeta - \frac{\cot\Theta}{\cot\theta}\right), \tag{2.22}$$

where the factor of 2 arises from the evenness of $\cos\gamma$. Only values of Θ for which $|\cot\Theta/\cot\theta| < 1$ contribute to the integral, which reduces the integration range to $(\theta, \pi-\theta)$. Integrating over ζ then yields

$$D^{(1)}_{\theta\theta} = \frac{4\pi k^2 \sin^2\theta}{c^3|\cos\theta|} \int_0^\infty \mathrm{d}K \int_\theta^{\pi-\theta} \mathrm{d}\Theta\, K\left(1 - \left(\frac{\cot\Theta}{\cot\theta}\right)^2\right)^{1/2} A(K,\Theta). \tag{2.23}$$

Substituting in

$$c = |\boldsymbol{\nabla}_{\boldsymbol{k}}\omega| = \frac{1}{k}\partial_\theta(f^2\cos^2\theta + N^2\sin^2\theta)^{1/2} = \frac{(N^2-f^2)|\sin\theta\cos\theta|}{\omega k}, \tag{2.24}$$

and rearranging gives the final form

$$D^{(1)}_{\theta\theta} = \frac{4\pi\omega^3 k^5}{(N^2-f^2)^3|\cos^5\theta|} \int_0^\infty \int_\theta^{\pi-\theta} K(\cot^2\theta - \cot^2\Theta)^{1/2} A(K,\Theta)\,\mathrm{d}K\mathrm{d}\Theta. \tag{2.25}$$

In summary, the diffusivity with time-dependent geostrophic flow has three significant components: $D_{kk} = D^{(0)}_{kk}$ and $D_{\phi\phi} = D^{(0)}_{\phi\phi}$ given by (2.15) and dependent on the energy spectrum of the geostrophic flow, and $D_{\theta\theta} = \epsilon^2 D^{(1)}_{\theta\theta}$ given by (2.25) and dependent on the flow acceleration spectrum. The small, non-zero $D_{\theta\theta}$ for non-vanishing flow acceleration captures the weak across-cone diffusion pointed out by Dong *et al.* (2020).

2.3 Equilibrium spectrum

2.3.1 Solution of the steady diffusion equation

We now focus on the response to the spatially homogeneous, azimuthally isotropic steady forcing

$$F(\boldsymbol{k}) = \delta(k - k_*)\delta(\theta - \theta_*) \tag{2.26}$$

corresponding to a single IGW frequency. (The response to a forcing with arbitrary dependence on k and θ can be obtained by integration.) We aim to show that the action density reaches an equilibrium $a(k, \theta)$ that is localised near $\theta = \theta_*$ – in other words, that the frequencies remain close to the forcing frequency for all time. This is in contrast with the two-dimensional case of Dong *et al.* (2020) for which no such localised equilibrium exists.

For ease of interpretation, we replace the action density by the energy density $e(k, \theta) = 2\pi k^2 \sin\theta\omega a(k, \theta)$, such that $e\,\mathrm{d}k\mathrm{d}\theta$ is the energy contained in the box $[k, k + \mathrm{d}k]$ and $[\theta, \theta + \mathrm{d}\theta]$. Eq. (2.1) then reduces to

$$\begin{aligned}\partial_k \left(k^2 \left(D^{(0)}_{kk} + \epsilon^2 D^{(1)}_{kk} \right) \partial_k \frac{e}{k^2} + \epsilon^2 \frac{\sin\theta\omega}{k} D^{(1)}_{k\theta} \partial_\theta \frac{e}{\sin\theta\omega} \right) \\ + \epsilon^2 \omega k \partial_\theta \left(\frac{1}{\omega} D^{(1)}_{k\theta} \partial_k \frac{e}{k^2} + \frac{\sin\theta}{k^3} D^{(1)}_{\theta\theta} \partial_\theta \frac{e}{\sin\theta\omega} \right) = -\delta(k - k_*)\delta(\theta - \theta_*),\end{aligned} \tag{2.27}$$

where we ignore unimportant prefactors on the right-hand side. We seek solutions localised in θ in a boundary layer of thickness ϵ around θ_*, assuming

$$\sigma = (\theta - \theta_*)/\epsilon = O(1). \tag{2.28}$$

To leading-order in ϵ, (2.27) reduces to

$$\partial_k \left(k^2 D^{(0)}_{kk}(\theta_*) \partial_k \frac{e}{k^2} \right) + \frac{1}{k^2} D^{(1)}_{\theta\theta}(\theta_*) \partial_{\sigma\sigma} e = -\delta(k - k_*)\delta(\sigma), \tag{2.29}$$

ignoring again a prefactor on the right-hand side. (In this case, the ignored prefactor is

$1/\epsilon$ which amounts to choosing the order of forcing in the perturbation expansion. If the factor is not neglected, the forcing appears against a left-hand side of zero, which is nonsensical. Equivalently, the forcing in (2.26) can be scaled to $\epsilon\delta(k-k_*)\delta(\theta-\theta_*)$. This scaling is natural – the energy e derived from (2.29) is of the form $f(k, (\theta-\theta_*)/\epsilon)/\epsilon$, where f is a function localised in its second argument, and integration with respect to θ gives an $O(1)$ energy distribution.) Note that $D^{(1)}_{\theta\theta}$ is the only correction to the diffusivity tensor induced by flow time dependence that appears in (2.29). (This also applies to anisotropic IGWs in the sense that $\partial_\phi a \neq 0$.) This correction appears at leading order, even though the corresponding diffusivity $\epsilon^2 D^{(1)}_{\theta\theta}$ is small, because of the large gradients in θ of the solution.

We make the dependence on k of the diffusivity components $D^{(0)}_{kk}$ and $D^{(1)}_{\theta\theta}$ in (2.15a) and (2.25) explicit by writing

$$D^{(0)}_{kk} = Q(\theta)k^3 \quad \text{and} \quad D^{(1)}_{\theta\theta} = R(\theta)k^5. \tag{2.30}$$

Under the change of variables

$$e = \bar{e}/(Q_* R_*)^{1/2} \quad \text{and} \quad \sigma = \bar{\sigma}(R_*/Q_*)^{1/2}, \tag{2.31}$$

where $Q_* = Q(\theta_*)$ and $R_* = R(\theta_*)$, (2.29) becomes

$$k^3\partial_{kk}\bar{e} + k^2\partial_k\bar{e} - 4k\bar{e} + k^3\partial_{\bar{\sigma}\bar{\sigma}}\bar{e} = -\delta(k-k_*)\delta(\bar{\sigma}). \tag{2.32}$$

In the following, we drop the overbars for simplicity.

We now solve the re-scaled problem (2.32). Taking a Fourier transform in σ, with l the corresponding Fourier variable, we find

$$k^3\partial_{kk}\hat{e} + k^2\partial_k\hat{e} - 4k\hat{e} - k^3 l^2\hat{e} = -\frac{\delta(k-k_*)}{2\pi}, \tag{2.33}$$

where the hat denotes the Fourier transform. The solution to the homogeneous problem can be written in terms of modified Bessel functions (DLMF, 2022, Ch. 10), leading

to the piecewise expression

$$\hat{e}(k,l) = \begin{cases} A(l)\mathrm{I}_2(|l|k) + B(l)\mathrm{K}_2(|l|k) & \text{for } 0 < k < k_* \\ C(l)\mathrm{I}_2(|l|k) + D(l)\mathrm{K}_2(|l|k) & \text{for } k > k_* \end{cases}, \tag{2.34}$$

where I and K are modified Bessel functions of the first and second kind, and A, B, C and D are so far arbitrary functions of l. These functions are determined by the boundary and jump conditions. Finiteness as $k \to 0$ and $k \to \infty$ requires that $B(l) = C(l) = 0$. Imposing continuity at k_* and the jump $[\partial_k \hat{e}]_{k_*^-}^{k_*^+} = -1/(2\pi k_*^3)$ then gives

$$\begin{pmatrix} A \\ D \end{pmatrix} = \frac{1}{2\pi \mathcal{W}\{\mathrm{K}_2(|l|k_*), \mathrm{I}_2(|l|k_*)\}|l|k_*^3} \begin{pmatrix} \mathrm{K}_2(|l|k_*) \\ \mathrm{I}_2(|l|k_*) \end{pmatrix} = \frac{1}{2\pi k_*^2} \begin{pmatrix} \mathrm{K}_2(|l|k_*) \\ \mathrm{I}_2(|l|k_*) \end{pmatrix}, \tag{2.35}$$

where $\mathcal{W}$ is the Wronskian and we use that $\mathcal{W}\{\mathrm{K}_2(z), \mathrm{I}_2(z)\} = 1/z$ (DLMF, 2022, Eq. (10.28.2)). Hence the solution in Fourier space is

$$\hat{e}(k,l) = \frac{1}{2\pi k_*^2} \times \begin{cases} \mathrm{K}_2(|l|k_*)\mathrm{I}_2(|l|k) & \text{for } 0 < k < k_* \\ \mathrm{I}_2(|l|k_*)\mathrm{K}_2(|l|k) & \text{for } k > k_* \end{cases}. \tag{2.36}$$

We invert the Fourier transform. As $\hat{e}$ is symmetric in l, the inverse of (2.36) is

$$e(k,\sigma) = \frac{1}{\pi k_*^2} \times \begin{cases} \int_0^\infty \mathrm{K}_2(lk_*)\mathrm{I}_2(lk)\cos(\sigma l)\,\mathrm{d}l & \text{for } 0 < k < k_* \\ \int_0^\infty \mathrm{I}_2(lk_*)\mathrm{K}_2(lk)\cos(\sigma l)\,\mathrm{d}l & \text{for } k > k_* \end{cases}. \tag{2.37}$$

This can be evaluated exactly using Eq. (4), §6.672 of Gradshteyn & Ryzhik (2014),

$$\int_0^\infty \mathrm{K}_\nu(ax)\mathrm{I}_\nu(bx)\cos(cx)\,\mathrm{d}x = \frac{1}{2(ab)^{1/2}} \mathrm{Q}_{\nu-1/2}\left(\frac{a^2+b^2+c^2}{2ab}\right), \tag{2.38}$$

which holds provided that $\mathrm{Re}(a) > |\mathrm{Re}(b)|$ and $\mathrm{Re}(\nu) > -1/2$. Here, $\mathrm{Q}_{\nu-1/2}$ is the Legendre function of the second kind (DLMF, 2022, Ch. 14). Clearly, the condition on ν is satisfied for (2.37). For $0 < k < k_*$, $a = k_* > k = b$; for $k > k_*$, $a = k > k_* = b$. Therefore, the condition on a and b also holds. Due to the symmetry of the solution

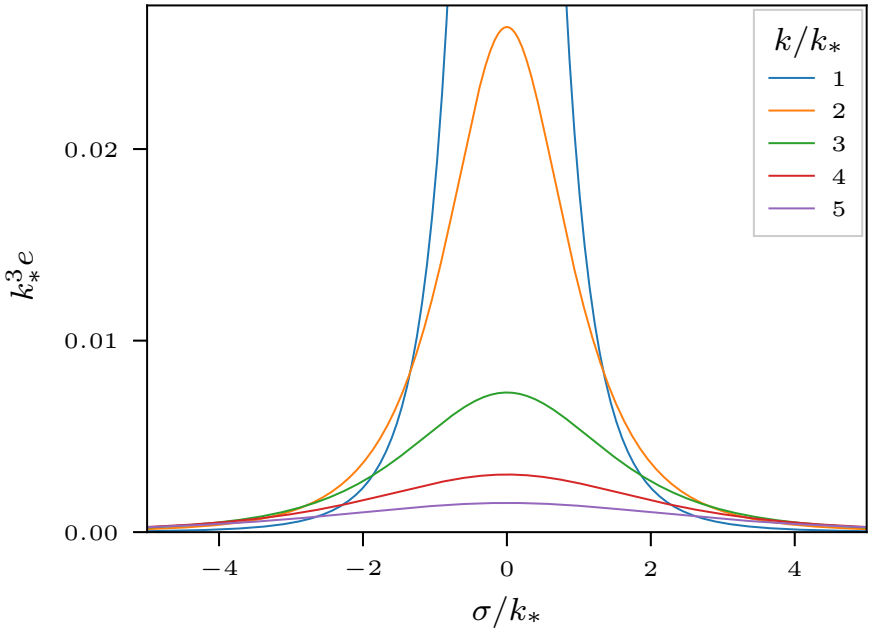

Figure 2.2: IGW energy spectrum e in (2.39) scaled by k_*^3 as a function of the scaled angle σ/k_* for a few values of non-dimensionalised total wavenumber k/k_*.

under exchanges of a and b, both integrals in (2.37) are equivalent, leading to

$$e(k,\sigma) = \frac{1}{2\pi k_*^{5/2} k^{1/2}} \mathrm{Q}_{3/2}\left(\frac{k_*^2 + k^2 + \sigma^2}{2k_* k}\right). \tag{2.39}$$

Eq. (2.39) is the main result of the paper. It gives the form of the equilibrium distribution of IGW energy forced at a single wavenumber and frequency, accounting for the time dependence of the turbulence. Since $\mathrm{Q}_{3/2}$ decays rapidly as its argument increases ($\mathrm{Q}_{3/2}(X) \to 3\pi(2X)^{-5/2}/8$ as $X \to \infty$), (2.39) shows that the IGW energy is localised within an $O(\epsilon)$ layer around the constant frequency cone $\theta = \theta_*$ (recall (2.28)). Note that $e(k,\sigma)$ has a mild, logarithmic singularity as $\sigma \to 0$ for $k = k_*$.

We illustrate the form of the energy spectrum predicted by (2.39) in figure 2.2. Here, e scaled by k_*^3 is plotted against the scaled angle σ/k_* for a few values of non-dimensionalised total wavenumber k/k_*. In figure 2.3, e is shown as a function of horizontal and vertical wavenumber and is scaled to approximately match the energy level of the simulation in §2.3.2. The value of R_*/Q_* is also required for figure 2.3 and is chosen to match simulation results.

A useful approximation to (2.39) is obtained from the asymptotics of the Legendre

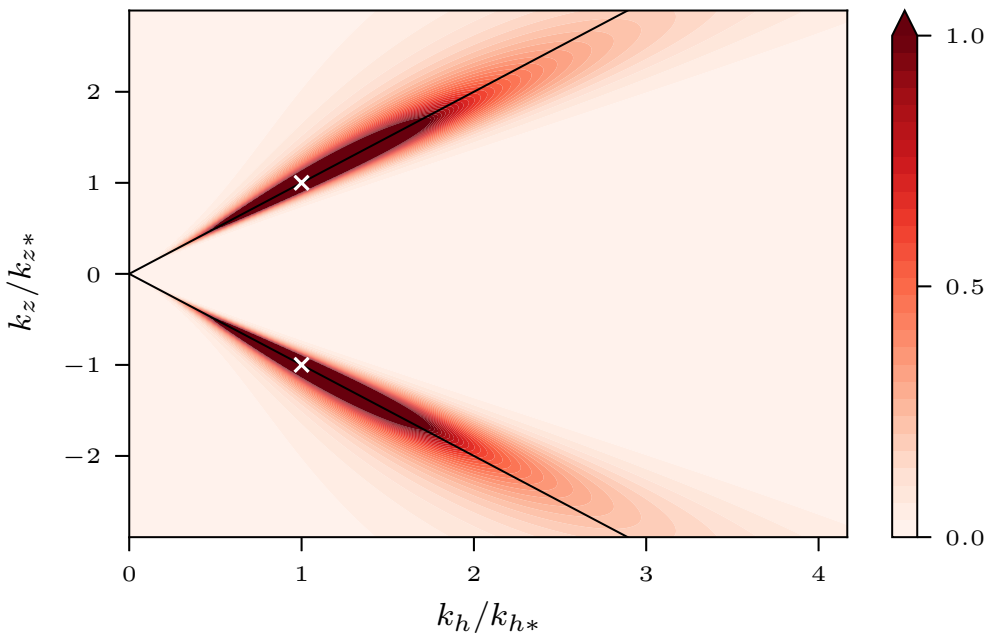

Figure 2.3: IGW energy spectrum e in (2.39) as a function of horizontal and vertical wavenumbers (k_h, k_z). The wavenumbers are scaled by the forcing wavenumbers (k_{h*}, k_{z*}) indicated by the white crosses. The cone corresponding to the forcing frequency is indicated by the solid lines. The parameters Q_* and R_* are chosen to match the simulation results in §2.3.2 (cf. figure 2.1).

function for large argument:

$$e(k,\sigma) \sim \frac{3}{16} k^{-3} \left(1 + \frac{k_*^2 + \sigma^2}{k^2}\right)^{-5/2}, \tag{2.40}$$

which applies for $k \to 0$, $k \to \infty$ or $\sigma \to \infty$. In particular, it makes it possible to characterise the angular localisation of the energy by the power law

$$e(k,\sigma) \sim \frac{3}{16} \frac{k^2}{\sigma^5} \quad \text{as} \quad \sigma \to \infty. \tag{2.41}$$

Eq. (2.40) further shows that at fixed σ, that is, at fixed angle θ or frequency, $e(k,\sigma) \propto k^{-3}$ as $k \to \infty$, and $e(k,\sigma) \propto k^2$ for $k \ll k_*$.

Another limit of interest deduced from (2.40) is

$$e(k,\sigma) \sim \frac{3}{16} k^{-3} \left(1 + \left(\frac{\sigma}{k}\right)^2\right)^{-5/2} \quad \text{as} \quad k \to \infty,\ \sigma/k = O(1), \tag{2.42}$$

which shows that the spectrum broadens in σ like k. Consequently, integration of (2.40)

across angles results in a spectrum decaying like k^{-2}. In fact, the integrated spectrum is exactly proportional to k^{-2} for $k > k_*$: indeed, integration of (2.32) with respect to $\bar{\sigma}$ recovers the equation found by KSV for time-independent flows, with solution proportional to k^{-2} for $k > k_*$ and k^2 for $k < k_*$. In appendix A.2 (not included in the published version of this paper), we integrate the spectrum (2.39) across angles to recover the KSV spectrum. This verifies the steps between (2.32) and (2.39).

In dimensional terms, the thickness of the boundary layer around the cone is proportional to the square root of the ratio R_*/Q_* (see (2.31)), which roughly amounts to the ratio of the flow acceleration variance to its energy, and can be interpreted as the relevant flow frequency. This increases when the flow becomes more transient resulting in a thicker boundary layer.

2.3.2 Comparison with Boussinesq simulations

We compare the analytical prediction (2.39) with the results of a high-resolution three-dimensional Boussinesq simulation. We solve the non-hydrostatic Boussinesq equations using a dealiased pseudospectral code adopted from that in Waite & Bartello (2006). A third-order Adams–Bashforth scheme with timestep $0.0044/f$ is employed for time integration. The triply periodic domain $[0, 2\pi]^2 \times [0, 2\pi f/N]$ is discretised with 2304^3 grid points. A hyperdissipation of the form $\nu_h(\partial_x^2 + \partial_y^2)^4 + \nu_z\partial_z^8$, with $\nu_h = 7.8 \times 10^{-23}$ and $\nu_z = 7.1 \times 10^{-35}$ (in dimensionless units, with the domain size as reference length and f^{-1} as reference time) is implemented in the momentum and buoyancy equations. We take $N/f = 32$, a representative value of mid-depth ocean stratification. We initialise the simulation with a fully developed geostrophic turbulent flow, which is the output of a decaying quasigeostrophic model with the initial energy spectrum proportional to $\exp\left(-(((K_h^2 + f^2K_z^2/N^2)^{1/2} - 24)/10)^2\right)$. This model is run until the energy spectrum fills the spectral space, peaking at $K_h = 4$ and scaling approximately as K_h^{-3} and K_z^{-3}. The flow parameters are selected such that the Rossby number based on the vertical vorticity ζ is $\mathrm{Ro} = \langle\zeta^2\rangle^{1/2}/f = 0.11$. Throughout the simulation, an Ornstein–Uhlenbeck forcing with short correlation time (three timesteps) is applied to the linear wave modes with $(k_{h*}, k_{z*}) = (12, 221)$ corresponding to the fixed IGW frequency of $2f$. This relatively low frequency is chosen so that the aspect ratio of

the IGWs is similar to the aspect ratio N/f of the geostrophic flow and thus the IGWs are well resolved with the anisotropic grid we use. The simulation is performed until $t = 160/f$ by which time the statistics are approximately stationary. Time series of the system's kinetic energy and enstrophy were monitored and the snapshot was taken at the point that both these quantities were constant to good approximation (unfortunately, these time series were not saved and the simulation is expensive to reproduce). We separate IGWs from the mean flow (both for forcing and extracting energy spectra) using the normal-mode decomposition of Bartello (1995).

We compare the functional form implied by (2.39) to the spectrum $e(k_h, k_z)$ obtained in the simulation. This involves fitting two parameters, one that fixes the scale of e and corresponds to strength of the forcing, and the other that fixes the scale of σ and corresponds to $(R_*/Q_*)^{1/2}$ (see (2.31)). We estimate these two parameters by matching the simulation spectrum as a function of $\theta - \theta_*$ for $k \gtrsim 5k_*$ as shown in figure 2.4. These values of k are large enough for the perturbation induced by the non-ideal nature of the forcing in the simulation to be negligible, and for discretisation effects to play only a minor role. A difficulty, evident in figure 2.4, is that the simulation spectrum is not symmetric. We attribute this to an edge effect caused by the proximity of the IGW frequency $\omega = 2f$ to the minimum allowable frequency $\omega = f$, and to the breakdown of the diffusion approximation when ω is close to f (see §2.5 for details). (The forcing frequency cone has a small opening angle, $\theta_* = \tan^{-1}(k_{h*}/k_{z*}) \approx 3°$, a feature obscured by the anisotropic scaling of the axes in figures 2.1 and 2.3.) We therefore carry out the parameter fitting based on the parts of the curves in figure 2.4 right of their maxima. We further allow for an offset of $\theta - \theta_*$, likely the result of the coarse discretisation of the wavevector in the forcing region.

Figure 2.4 could be improved by taking an average energy spectrum over a series of snapshots of the simulation, rather than the instantaneous comparison we show here. This has not been done due to resource limitations – the simulation is expensive and the final snapshot is the only saved data. However, the instantaneous snapshot is a good approximation of the stationary statistics of the system because at this point, the energy of the system was constant to good approximation.

The prediction of (2.39) with the two fitted parameters is shown by the dashed curves in figure 2.4. The agreement with the numerical results is good: (2.39) captures

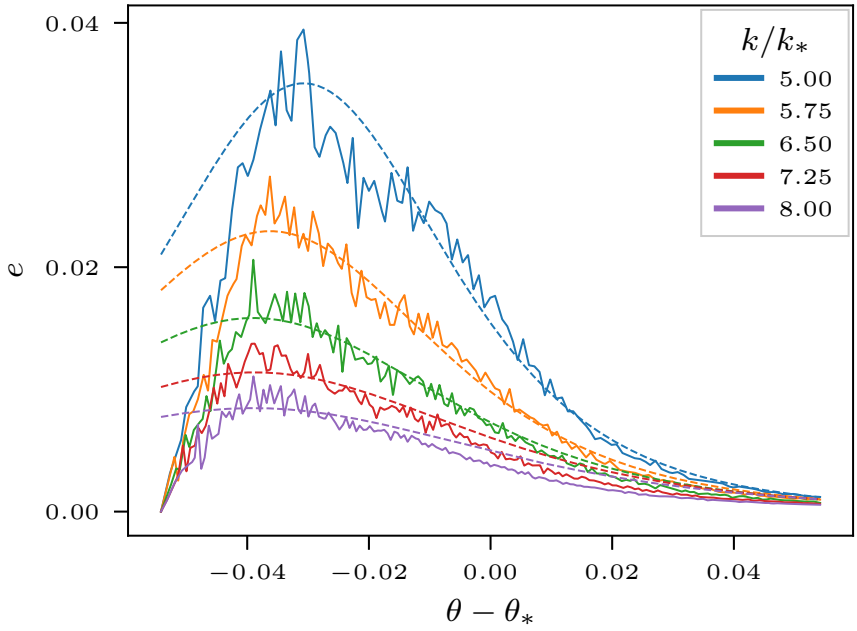

Figure 2.4: IGW energy spectrum e vs $\theta - \theta_*$ for several values of k/k_*: comparison between simulation results (solid lines) and analytical prediction (2.39) (dashed lines). The scalings of e and $\sigma \propto \theta - \theta_*$ are chosen for the analytical prediction to best match the simulation data (scaling σ corresponds to estimating $(R_*/Q_*)^{1/2}$, see (2.28) and (2.31)).

the localisation of e and the general form of its decrease with $\theta - \theta_*$ at different values of k. (We emphasise that the same two parameters are used for all the curves.) A complementary view is provided by figure 2.5 which shows e obtained in the simulation as a function of $\theta - \theta_*$ (panel (a)) and of k/k_* (panel (b)) in log–log coordinates. The power laws σ^{-5} (equivalent to $(\theta - \theta_*)^{-5}$), k^{-3} and k^2 derived in (2.40)–(2.41) from (2.39) are shown in their range of expected validity. The σ^{-5} and k^{-3} power laws are consistent with the data albeit over a limited wavenumber range. We regard this as a reasonable match given the difficulties in capturing such rapid decay in a numerical model, and the pollution by the forcing. The k^2 power law is a poorer match. This is to be expected since the spatial scale-separation assumption between IGWs and geostrophic flow that underpins the diffusion equation (2.1) is not satisfied for wavenumbers smaller than the forcing wavenumber. The numerical spectrum for small k is also strongly affected by discretisation effects. Note that the abrupt drop in the tail of spectra in figure 2.5(b) comes from the truncation of data due to storage limitation; the total energy spectrum shows a smooth transition to dissipation range (not shown).

(a)

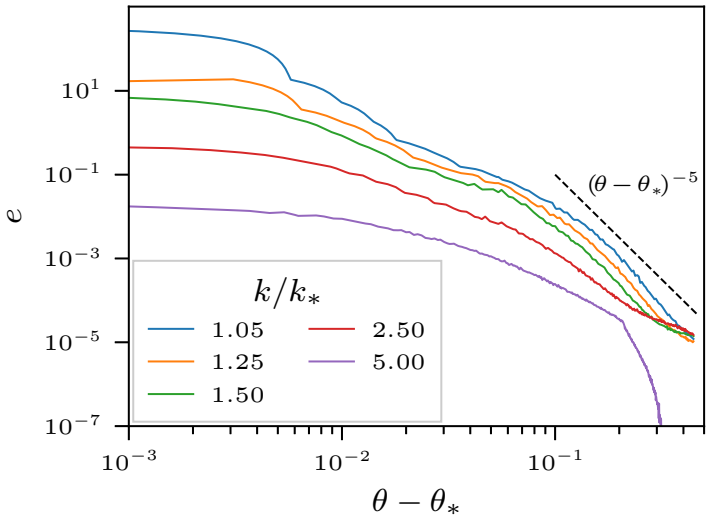

(b)

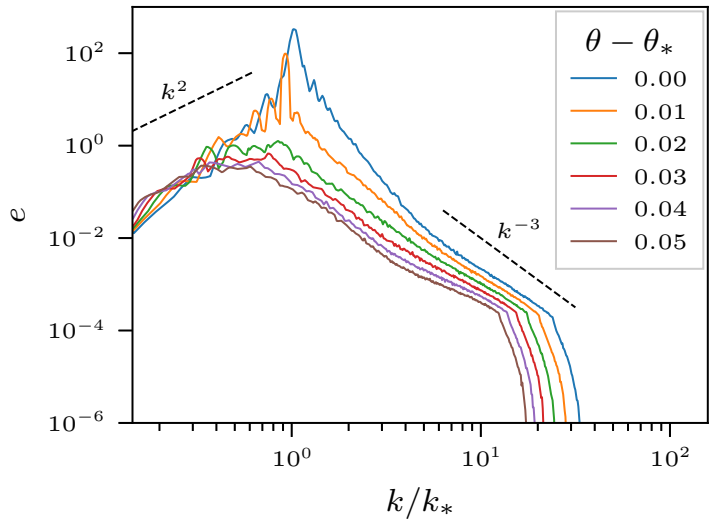

Figure 2.5: IGW energy spectrum e from simulation data in log–log coordinates: (a) as a function of $\theta - \theta_*$ for several values of k/k_*, and; (b) as a function of k/k_* for several values of $\theta - \theta_*$. Predicted power laws are indicated by dashed lines.

Overall, the simulation results compare as well with (2.39) as can be expected given the numerical challenges posed by the finite resolution, non-ideal forcing and an IGW signal that has both low amplitude and decreases rapidly with k and $\theta - \theta_*$. We note that it is in principle possible to compute the scaling parameter $(R_*/Q_*)^{1/2}$ from simulation data using the explicit expressions for R_* and Q_* deduced from (2.15a), (2.25) and (2.30). KSV evaluate Q_* based on the energy spectrum of the geostrophic flow they estimate from simulation data. An analogous evaluation of R_* requires the acceleration spectrum of the geostrophic flow. We leave this computation for future work.

2.4 Discussion

This paper is part of a sequence of works that apply techniques of waves in random media to address the role of the geostrophic flow in shaping the energy distribution of atmospheric and oceanic inertia-gravity waves (Danioux & Vanneste, 2016; Savva & Vanneste, 2018; Kafiabad *et al.*, 2019; Savva *et al.*, 2021). Their main assumption is that the flow is weak enough to be regarded as a small perturbation to what would otherwise be IGWs propagating in a medium at rest. The perturbation, physically transport and refraction, can be interpreted as arising from resonant triadic interactions involving two IGW modes and a geostrophic (or vortical) mode – these are known as 'catalytic interactions' in recognition of the fact that the geostrophic mode is left unaffected (Lelong & Riley, 1991; Bartello, 1995). The present paper further assumes that the IGWs have spatial scales much smaller than the flow scales. In this case, the impact of the flow, modelled as a random field, on the IGWs is a diffusion of wave action in wavevector space. (This is the induced diffusion regime considered by McComas & Bretherton (1977) in the context of wave–wave interactions.) KSV examined this process in some detail and showed, in particular, that it leads to IGW characteristics such as a k^{-2} stationary spectrum that are consistent with atmospheric and oceanic observations.

To obtain these results, KSV treated the geostrophic flow as time independent, on the grounds that it evolves on a time scale much longer than the IGW periods. With this assumption, the geostrophic mode has a zero frequency. The (resonant) catalytic interactions therefore involve two IGW modes with exactly the same frequency, and

wave action exchanges are restricted to a constant-frequency surface in wavevector space. Here, we revisit this assumption by taking the geostrophic flow to be slowly evolving. In this case, the catalytic interactions are between a low frequency geostrophic mode and two IGWs with slightly different frequencies, and action diffuses across the constant-frequency surface. The question is therefore whether this leads to qualitative changes in the statistics of IGWs, for instance by enabling IGW frequencies to diffuse freely and wave action to spread unimpeded across wavevector space (as was recently shown to be the case for two-dimensional waves by Dong *et al.* (2020)). The answer is no: we show that the stationary spectrum established by forcing single-frequency IGWs is localised within a boundary layer close to the cone of constant frequency associated with the forcing. Thus, even in the infinite-time limit corresponding to this stationary response, the time dependence of the geostrophic flow has only a minor impact on the IGW scattering. Hence, the conclusions of KSV drawn by neglecting the time dependence hold for realistic slowly evolving flows. In particular, scattering by geostrophic flow does not control the frequency distribution of IGWs which, in the absence of other mechanisms, is determined by the forcing or initial conditions. This is only strictly true over a finite range of wavenumbers k, since the thickness of the boundary layer increases with k (see (2.42)). However, at large k the hypotheses of weak flow and linear waves also break down (see KSV) and may have a larger impact than the flow time dependence (see §2.5 for a discussion of the restriction on k imposed by the weak-flow hypothesis).

It is worth commenting on the sharp difference between the conclusion drawn here for three-dimensional IGWs in a three-dimensional geostrophic flow and that drawn by Dong *et al.* (2020) in a two-dimensional set up. This difference stems from the very different geometry of the constant-frequency surfaces which are compact in dimension two (circles) and non-compact in dimension three (cones). In the compact case, an initial distribution of action quickly relaxes to become uniform on constant-frequency circles, then slowly spreads across these circles because of the flow time dependence. The flux of action perpendicular to the constant-frequency circles is small, but it allows for the wave frequencies to change without restriction over long time scales. In contrast, for the (non-compact) cones of the three-dimensional case, there is a non-zero action flux along cones, even in the absence of flow time dependence, corresponding to a

forward cascade towards small scales. The flux across cones introduced by the slow time dependence of the geostrophic flow acts therefore only as a small perturbation which barely affects the (non-equilibrium) stationary spectrum at finite distances along the cones.

2.5 Limitation of the diffusion approximation

The diffusion approximation (2.1) on which (2.39) and KSV rely is valid for $U \ll c$. Defining the velocity-based Rossby number, $\mathrm{Ro} = UK_h/f$ (rather than the vorticity-based definition of §2.3.2), and using c in (2.24), we can rewrite this condition as

$$\frac{k_h}{K_h} \ll \frac{\left((N/f)^2 - 1\right)\sin^2\theta\cos\theta}{\mathrm{Ro}\left((N/f)^2\sin^2\theta + \cos^2\theta\right)^{1/2}} \tag{2.43}$$

where $k_h = k\sin\theta$ is the horizontal wavenumber and we have taken $0 \le \theta \le \pi/2$ without loss of generality. Figure 2.6 displays the right-hand side of (2.43) against θ for a range of values of N/f typical of the ocean and atmosphere. The figure shows that, for realistic, small Rossby numbers ($\mathrm{Ro} \in [10^{-2}, 10^{-1}]$), the range of k_h over which the diffusion approximation is valid extends to 20–200 times the typical flow wavenumber K_h for all IGWs except those with frequencies very close to f ($\theta = 0$) and N ($\theta = \pi/2$). (A scattering theory tailored to IGWs with frequencies close to f, that is, near-inertial waves, is developed in Danioux & Vanneste (2016).)

To determine the range of k_h and k_z for which condition (2.43) is met in our simulation, we recast (2.43) in terms of k/k_* as used in figures 2.4 and 2.5 to obtain

$$\frac{k}{k_*} = \frac{k_h\sin\theta_*}{k_{h*}\sin\theta} = \frac{k_z\cos\theta_*}{k_{z*}\cos\theta} \ll \frac{\left((N/f)^2 - 1\right)\sin\theta\cos\theta}{\mathrm{Ro}\left((N/f)^2\sin^2\theta + \cos^2\theta\right)^{1/2}}\frac{K_h}{k_*}. \tag{2.44}$$

The simulation parameters are: $N/f = 32$, $k_* = 221.3$ and $K_h = 4$. The velocity-based Rossby number is estimated to be $\mathrm{Ro} = 0.05$. Using these parameters we compute the curve in the (k_h, k_z)-plane where (2.44) is satisfied as an equality and show the result in figure 2.7. The two lobes labelled C and D indicate the region of validity of the diffusion approximation. The rectangles labelled A (also shown in the inset)

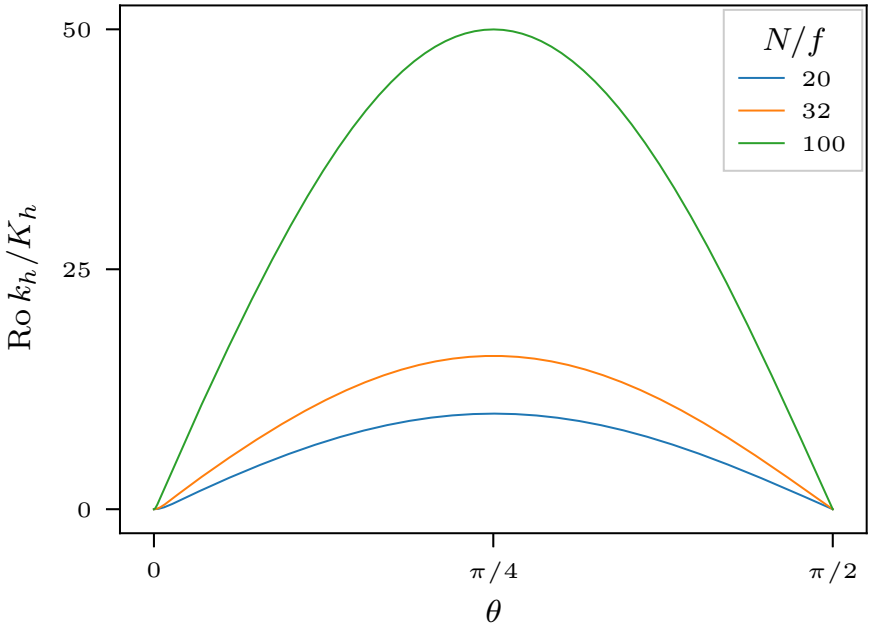

Figure 2.6: Upper bound of $\mathrm{Ro}\, k_h/K_h$ given by the right-hand side of (2.43) as a function of θ for a range of N/f values including our simulation value, $N/f = 32$.

and B show the ranges of k_h and k_z used in figure 2.1 and resolved in the simulation, respectively. This confirms that the diffusion approximation applies to the typical wavenumbers considered in our analysis. However, because of the rapid change of k_z as θ decreases from θ_*, the diffusion approximation can be expected to break down around $\theta - \theta_* \approx -0.03$ in figure 2.4. This likely explains the mismatch between theoretical prediction and simulation results to the left of the curves' maxima in the figure.

2.6 Width of spectral peaks

The energy spectrum (2.39) decays away from the forcing frequency within a boundary layer determined by the variable change (2.31). In this section, not included in the published version of the above paper, we propose the boundary layer width as a measure of the spread in frequency of internal tides away from their forcing frequency. There is interest in estimating this spreading (e.g. Geoffroy & Nycander, 2022; Zaron, 2022) because it is thought to quantify nonlinear interactions between tides and low-frequency inhomogeneities in the ocean.

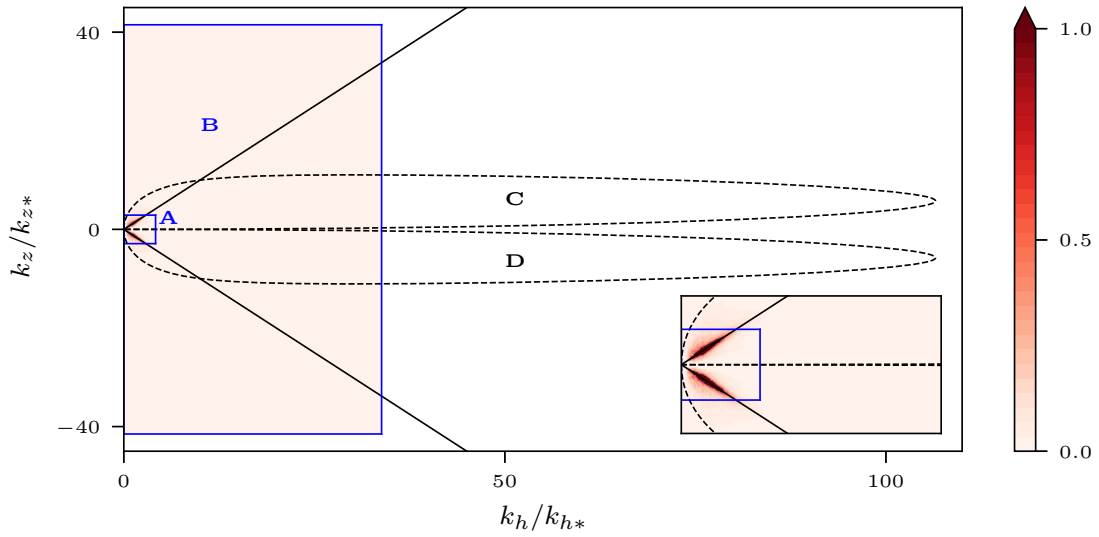

Figure 2.7: Region of validity of the diffusion approximation in the simulation: inequality (2.44) holds in regions C and D, where the diffusion approximation applies; rectangle A (also in the inset) reproduces figure 2.1 in showing the energy density e; rectangle B shows the ranges of k_h and k_z resolved in the simulation.

Observed wave energy spectra, such as those taken from moorings in the ocean, are dominated by peaks at the semi-diurnal, diurnal and inertial (Coriolis) frequencies (see, for example, the kinetic energy spectra in figure 2 of Luecke *et al.* (2020)). The semi-diurnal and diurnal peaks are the result of astronomical forcing. The strongest peak is typically the semi-diurnal frequency.

Astronomical forcing is the combined effect of the Moon and Sun's gravitational force, and the Earth and Moon's orbits. It can be described as a discrete set of frequencies and amplitudes derived from orbital parameters, called tidal constituents, which make up the depth-independent tidal potential. Although the semi-diurnal and diurnal peaks appear to be at a single frequency, they are actually made up of many lunar and solar components at slightly different frequencies.

The tidal potential drives a depth-independent current, called the barotropic tide, at tidal frequencies. The barotropic tide is scattered at topography, exciting internal tides (also called baroclinic tides) (see Garrett & Kunze (2007) for a review).

Early work (Doodson, 1921) modelled internal tides as harmonics with frequencies and amplitudes given by the tidal potential. A response method developed by Munk, Cartwright & Bullard (1966) improves on this, considering tides to be the internal wave

components which maintain both constant phase and amplitude in relation to the tidal potential. This filters out random motions propagating at tidal frequencies.

Thus, internal wave spectra are split into a coherent component, also called phase locked, which maintains a constant relationship in phase and amplitude with the tidal potential, and noncoherent tides, also called non-phase locked. The barotropic tide is almost entirely coherent, whereas baroclinic internal tides have significant noncoherent components. Noncoherent tidal spectra have broad peaks at the semi-diurnal and diurnal frequencies, despite the sharp, coherent peaks being removed.

Broad, noncoherent peaks are thought to be the result of 1) seasonal changes in stratification which cause internal tides to be generated at frequencies away from the tidal potential (see, for example, Baines, 1982) and; 2) time-dependent background flow and stratification modifying the frequency of internal tides as they propagate (Munk, Zetler & Groves, 1965). The two are difficult to distinguish between, both being the result of time-dependent background fields. Munk *et al.* (1965) estimate the frequency smearing due to time-dependent background flow. Their estimate is a cusp, so they term these peaks tidal cusps. However, the agreement between this estimate and the actual noncoherent peak width is not good. Munk *et al.* (1965) attribute this to varying stratification or higher-order interactions. In the following, tidal cusp refers to peaks in the noncoherent tidal spectrum, despite the peaks themselves not actually being cusp-like.

In this chapter, we have derived an expression for the wave energy spectrum across the cone of constant frequency in wavevector space, (2.39). This steeply decaying spectrum, shown for fixed radial wavenumber in figure 2.2, exists within a boundary layer of thickness proportional to $(R_*/Q_*)^{1/2}$ in wavevector space (see (2.31)). The k-independent quantities R_* and Q_* are defined through (2.30) and the polar and radial diffusivities $D_{\theta\theta}$ (2.25) and D_{kk} (2.15a). From these equations, $(R_*/Q_*)^{1/2}$ can be interpreted as the square root of the balance between the flow acceleration and its energy i.e. the relevant flow frequency.

The boundary layer width, $(R_*/Q_*)^{1/2}$, we derive above quantifies the smearing of a forcing frequency due to flow time dependence. It is a flow frequency, although not necessarily the characteristic frequency of the flow – R_* and Q_* are θ dependent and the integral limits mean sections of the flow are invisible to the waves (see §3.3.3 for a

discussion on this). The flow energy and acceleration spectra also have Θ-dependent prefactors in the integrands. We propose that the widths of tidal cusps observed in data are proportional to $(R_*/Q_*)^{1/2}$, a revision of Munk *et al.* (1965). Note that like Munk *et al.* (1965), our spectrum (2.39) contains an actual cusp at the forcing frequency, not a broad peak, because of the mild logarithmic singularity as $\theta \to \theta_*$, $k = k_*$, the forcing ring.

There is interest in measuring the tidal cusp width because the noncoherent spectrum quantifies the nonlinear interactions between coherent tides and low-frequency background processes (Zaron, 2022). This is important in devising models for internal tides interacting with low-frequency background flow, such as Kachelein *et al.* (2022). Munk *et al.* (1965) propose that long-term climate fluctuations might be captured in fluctuations of internal tides. Colosi & Munk (2006) expand on this, attributing long-time tidal fluctuations in Hawaii to global warming.

It is difficult to discern the individual width of tidal cusps because the tidal constituents in the semi-diurnal and diurnal bands are close together. Colosi & Munk (2006) resolve the individual spectral peaks, derived from mean sea level data, and show that there is interference between neighbouring peaks in each band. They fit a model peak to the central part of each cusp which is uncontaminated by neighbouring cusps. This allows extrapolation to fully determine individual peaks, which would enable a cusp-width estimate. Resolving the individual peaks requires frequent observations, whilst capturing long-term variability requires a long time series of data.

Kelly *et al.* (2015) analyse spectra from mooring records in the Timor Sea. They use the response method of Munk *et al.* (1966) to identify the variation of the noncoherent tide. Instead of resolving the individual cusps, they find the total variation of the semi-diurnal band. They find the bandwidth and decorrelation frequencies of the semi-diurnal noncoherent tides to be similar to the barotropic mean flow frequency, which supports the notion that time-dependent background flows cause smearing of the tidal frequencies.

In order to compare our estimate $(R_*/Q_*)^{1/2}$ to the observed tidal cusps we need to establish a measure of observational cusp width. We also need to decide whether we will compare our estimate with individual peak widths, extrapolated to avoid interference as in Colosi & Munk (2006), or compare the estimate to the total peak width as in Kelly

et al. (2015). The former requires more work to estimate the observed tidal cusp width, whereas the latter requires our estimate to be adapted to many close together forcing frequencies, as is the case in the semi-diurnal band.

Our estimate $(R_*/Q_*)^{1/2}$ requires background flow energy and acceleration spectra, as well as the buoyancy frequency N of the mooring location. To extract the mean flow energy spectra we could follow Kelly *et al.* (2015) and average the observed energy spectra over a long time period. Kelly *et al.* (2015) also compute buoyancy frequency from density measurements. In order to confirm our estimate, mooring data should be taken from multiple locations or the cusp width should be estimated for multiple peaks at a single location.

Colosi & Munk (2006) and Kelly *et al.* (2015) provide good starting points for future work estimating tidal cusp width and comparing this to our prediction. We can be encouraged by Kelly *et al.* (2015), who find similar values for mean flow frequency and noncoherent peak width.

To summarise, we propose the boundary layer width $(R_*/Q_*)^{1/2}$, dependent on the flow energy and acceleration spectra and the buoyancy frequency N, is proportional to the width of observed tidal cusps in wave energy spectra. Comparing the estimate to observed cusps could help to decide what causes the spread of tidal frequencies – slow flow, changing stratification or nonlinear wave interactions. A positive correlation between predicted tidal cusp width and observed tidal cusp width would, if found, demonstrate the importance of IGW scattering by slowly evolving background velocities in determining atmospheric and oceanic wave energy spectra.

Chapter 3

Inhomogeneity-induced wavenumber diffusion

This chapter consists of a paper of the same name submitted to the Journal of Fluid Mechanics and available on arXiv at `https://doi.org/10.48550/arXiv.2406.17149` (Cox *et al.*, 2024). The key modifications to the initial submission are 1) the WKB analysis of a rotating shallow water system appears in the introduction of this thesis (§1.4) rather than in the appendices; 2) an additional appendix (§B.1) is included which concerns corrections to the IGW frequency (1.76) induced by buoyancy gradients and; 3) a consistency check on our ray tracing simulations is included in a second additional appendix (§B.2).

The Boussinesq simulation of §3.3.3 and the code for the two-dimensional Navier–Stokes simulation of §3.3.2 are the work of Hossein A. Kafiabad alone. The remainder of the paper, including simulation data analysis and shallow water ray tracing, is a collaborative work between the authors.

3.1 Introduction

Inertia-gravity waves (IGWs) propagate in the atmosphere and ocean under the restoring forces of buoyancy and Coriolis effect. As they propagate, they encounter and interact with a variety of inhomogeneities, including background flows, topography and other waves. These inhomogeneities refract, reflect and, in the case of background flows,

advect the waves. For example, internal tides – IGWs generated at the semi-diurnal and diurnal frequencies by astronomical forcing – are advected and refracted by background flows (e.g. Park & Watts 2006; Rainville & Pinkel 2006; Chavanne *et al.* 2010; Pan, Haley & Lermusiaux 2021) and reflected by bottom topography (e.g. Müller & Xu 1992; Bühler & Holmes-Cerfon 2011; Kelly *et al.* 2013; Lahaye, Gula & Roullet 2020; Pan *et al.* 2021). IGWs are also affected by each other (e.g. Eden & Olbers, 2014). In the limit of weak, repeated interactions, wave energy is redistributed in spectral space in a scattering process which can be described statistically.

Kinetic equations derived from the governing fluid equations provide this statistical description of scattering by weak, slowly evolving, random inhomogeneities (see Hasselmann (1966) and Ryzhik, Papanicolaou & Keller (1996) for general formulations). For example, Hasselmann (1966) and Ardhuin & Herbers (2002) derive a kinetic equation for surface waves scattered by gently-sloping bottom topography; Eden, Pollmann & Olbers (2019) derive a scattering equation for IGWs interacting with a weak, random, slowly evolving wave field (see also Eden, Pollmann & Olbers, 2020); and Danioux & Vanneste (2016), Savva & Vanneste (2018) and Savva, Kafiabad & Vanneste (2021) derive kinetic equations for near-inertial waves, internal tides and IGWs respectively, scattered by weak, slowly evolving turbulence. A key feature of scattering is that if the scattering inhomogeneities evolve sufficiently slowly compared with the waves, wave frequency is preserved.

This paper concerns the WKB limit of large-scale inhomogeneities scattering small-scale waves, in which scattering reduces to diffusion in spectral space. The corresponding induced-diffusion equation can be derived by invoking conservation of wave action density, which holds in the WKB limit. This was first done by McComas & Bretherton (1977) in the context of wave-wave interactions using the ray equations – the characteristic equations for action conservation. (McComas & Bretherton (1977) note that their derivation also applies to diffusion induced by low-frequency currents. A flow-induced diffusivity is first discussed in Müller & Olbers (1975) and expanded on in Müller (1976, 1977).) Recently, alternative derivations for the diffusion equation start with the conservation of wave action and use multi-scale asymptotics. They have been carried out for weak geostrophic flows scattering 1) IGWs in a 3D Boussinesq system (Kafiabad, Savva & Vanneste 2019, hereafter KSV); 2) Poincaré waves in a rotating

shallow water system (Dong, Bühler & Smith, 2020) and; 3) deep-water surface waves (Villas Bôas & Young, 2020). In all these derivations, the geostrophic flow impacts wave propagation solely through the Doppler shift term of the wave dispersion relation. McComas & Bretherton (1977) and Savva (2020) show that induced-diffusion is the WKB limit of a scattering integral for wave-wave and wave-flow interactions respectively. Yang *et al.* (2023) investigate the relevance of diffusion theories in a realistic ocean simulation.

The aims of this paper are twofold: 1) we argue at the level of the dispersion relation that inhomogeneities other than Doppler shift can be significant in scattering waves (§3.2); and 2) we derive the spectral diffusivity induced by any weak inhomogeneity (§3.3), thus generalising the original result of McComas & Bretherton (1977) .

In §3.2 we use scaling arguments to compare the Doppler shift term of the dispersion relation to two ofttimes neglected inhomogeneities: height fluctuations in a rotating shallow water system, and buoyancy gradients in a Boussinesq system. The height fluctuation effects are neglected in Dong *et al.* (2020) and the buoyancy fluctuation term is neglected in previous work of the authors, KSV and Cox, Kafiabad & Vanneste (2023, hereafter CKV). For both systems, we find regimes where these inhomogeneities can be significant. Doppler shift and vertical flow buoyancy gradients are accounted for in tidal ray tracing implemented by Chavanne *et al.* (2010). They find both to be important and, in their simulations, refraction by these gradients is more significant in the transfer of wave energy than advection by Doppler shift. (The ray tracing formulation used by Chavanne *et al.* (2010) is outlined in Olbers (1981) for IGWs propagating in geostrophic flows with vertical and horizontal shears.) Doppler shift, refraction through a background flow, buoyancy gradients and topography are all found to be significant in a coupled set of tidal equations derived by Pan *et al.* (2021).

In §3.3, we impose further statistical assumptions on the inhomogeneities, assume they are slowly time dependent and follow the perturbation expansion of KSV to reach a general diffusion equation for any inhomogeneity. We evaluate the general diffusivity for our two example systems and revise the scaling arguments of the previous section. For the shallow water system, we support our analysis with ray tracing simulations (§3.3.2), finding good agreement with the exact solution for 2D wave action given in Villas Bôas & Young (2020). For the Boussinesq system, we find the forced

equilibrium spectrum of wave energy. We also evaluate the Boussinesq diffusivity for a typical quasi-geostrophic flow.

3.2 Scaling arguments

In this section, we introduce a general inhomogeneity term into the wave dispersion relation for waves in the WKB regime. This term encompasses Doppler shift by a background flow but can include additional inhomogeneities. We motivate the inclusion of two such inhomogeneities: flow-induced height fluctuations in a rotating shallow water system and vertical buoyancy gradients in a 3D Boussinesq system. We find regimes where the additional inhomogeneities are significant, at points dominant. This has implications to ray tracing simulations which do not always take into account inhomogeneities other than Doppler shift and motivates the general diffusion equation derivation of §3.3, because previous diffusion equations of the form first introduced by McComas & Bretherton (1977) have only considered Doppler shift (by a background flow or long waves) as the scattering mechanism.

Our starting point is the conservation of wave action a in $(\boldsymbol{x}, \boldsymbol{k})$ space, which holds in the WKB limit of small-scale waves scattered by large-scale inhomogeneities:

$$\partial_t a + \boldsymbol{\nabla}_{\boldsymbol{k}}\omega \cdot \boldsymbol{\nabla}_{\boldsymbol{x}} a - \boldsymbol{\nabla}_{\boldsymbol{x}}\omega \cdot \boldsymbol{\nabla}_{\boldsymbol{k}} a = 0. \tag{3.1}$$

The absolute frequency of the waves ω is the sum of a homogeneous part, ω_0, and a weak, inhomogeneity-induced part, ω_1:

$$\omega(\boldsymbol{x}, \boldsymbol{k}, t) = \omega_0(\boldsymbol{k}) + \omega_1(\boldsymbol{x}, \boldsymbol{k}, t), \tag{3.2}$$

with $\omega_1 \ll \omega_0$. We call ω_0 the *bare* frequency and assume that it varies sufficiently slowly in time and space as to be considered constant. The frequency correction ω_1 includes the Doppler shift $\boldsymbol{U} \cdot \boldsymbol{k}$ and any other inhomogeneities. We consider two systems where other inhomogeneities inevitably arise in the presence of Doppler shift.

3.2.1 Shallow water

We consider Poincaré waves propagating in rotating shallow water with flat bottom and a background geostrophic flow. The background velocity $\boldsymbol{U} = (U, V, 0)$ and height H are related through the geostrophic balance

$$f\boldsymbol{e}_z \times \boldsymbol{U} = -g\boldsymbol{\nabla}_{\boldsymbol{x}}\Delta H, \tag{3.3}$$

where f is the Coriolis frequency, g the gravitational constant and $\boldsymbol{e}_z$ the unit vertical vector. Here we have introduced ΔH, the geostrophic perturbation to the mean height $\bar{H}$ such that $H = \bar{H} + \Delta H$ (see figure 1.2). ΔH and hence $\boldsymbol{U}$ is assumed to vary slowly in time and space compared with the period and wavelength of the Poincaré waves. In §1.4, we verified that action conservation (3.1) holds in this case.

Assuming that $\Delta H \ll \bar{H}$, the frequency of waves with wavevector $\boldsymbol{k} = (k_1, k_2)$ can be approximated as

$$\omega = (f^2 + g(\bar{H} + \Delta H)k_h^2)^{1/2} + \boldsymbol{U}\cdot\boldsymbol{k} \approx \omega_0 + \frac{g\Delta H k_h^2}{2\omega_0} + \boldsymbol{U}\cdot\boldsymbol{k}, \tag{3.4}$$

where $k_h = (k_1^2 + k_2^2)^{1/2}$ is the wavenumber and $\omega_0 = (f^2 + g\bar{H}k_h^2)^{1/2}$ is the intrinsic frequency for constant height $\bar{H}$. Thus, there are two contributions to the frequency inhomogeneity,

$$\omega_1 = \underbrace{\frac{g\Delta H k_h^2}{2\omega_0}}_{\text{height fluctuation}} + \underbrace{\boldsymbol{U}\cdot\boldsymbol{k}}_{\text{Doppler shift}}, \tag{3.5}$$

and hence two contributions to the scattering.

We now compare the relative size of the terms in (3.5) to argue that height fluctuation effects can be just as important as Doppler shift in ray tracing and induced diffusion. We introduce the characteristic flow speed U_*, characteristic horizontal wavenumber K_* and the flow Burger number

$$Bu = \frac{g\bar{H}}{f^2}K_*^2. \tag{3.6}$$

Using the geostrophic balance (3.3) and expressing ω_0 in terms of Bu, the height

fluctuation term scales like

$$\frac{g\Delta H k_h^2}{2\omega_0} \sim \frac{U_* k_h^2}{2K_*(1+Bu(k_h/K_*)^2))^{1/2}}. \tag{3.7}$$

Then, the ratio between the height fluctuation and Doppler shift terms is given by

$$R_{\text{sw}} = \frac{\text{height fluctuation}}{\text{Doppler shift}} \sim \frac{k_h/K_*}{2(1+Bu\,(k_h/K_*)^2)^{1/2}}. \tag{3.8}$$

In figure 3.1, we plot the ratio R_{sw} given by (3.8) against non-dimensionalised wavenumber k_h/K_* for different realistic values of the Burger number: $Bu = O(1)$ corresponds to the quasi-geostrophy (QG) regime and $Bu \ll 1$ to the planetary geostrophy (PG) regime. We take the limit of (3.8) for large k_h/K_*, a necessary condition for (3.1) to hold,

$$R_{\text{sw}} \to Bu^{-1/2}/2, \quad k_h/K_* \gg 1. \tag{3.9}$$

We see that for $Bu = 0.25$, $R_{\text{sw}} \to 1$ and the height fluctuation and Doppler shift terms in (3.5) have the same magnitude. For $Bu = 1$ corresponding to QG flow, $R_{\text{sw}} \to 0.5$. For smaller Bu associated with PG, height fluctuations dominate over Doppler shift. For larger Bu, Doppler shift dominates over height fluctuations.

In §3.3.1, we show a better estimate for the relative importance of height fluctuation to Doppler shift effects in the diffusion regime is $R'_{\text{sw}} = R^2_{\text{sw}}$. This is because the diffusion tensor is an integral over the product of frequency corrections ω_1 so the estimate based on the diffusivity tensor is a square of the estimate from this section. The diffusion regime estimate is also plotted in figure 3.1.

3.2.2 3D Boussinesq

Chavanne *et al.* (2010) compare the effect of refraction through flow buoyancy gradients to that of Doppler shift on internal tide propagation. Our set-up is similar to theirs – we consider 3D IGWs of wavevector $\boldsymbol{k} = (k_1, k_2, k_3)$ propagating in a geostrophic flow $\boldsymbol{U} = (U, V, 0)$ with buoyancy B. Unlike the tides, our waves are not in hydrostatic balance.

We first consider waves propagating with no background flow buoyancy gradients.

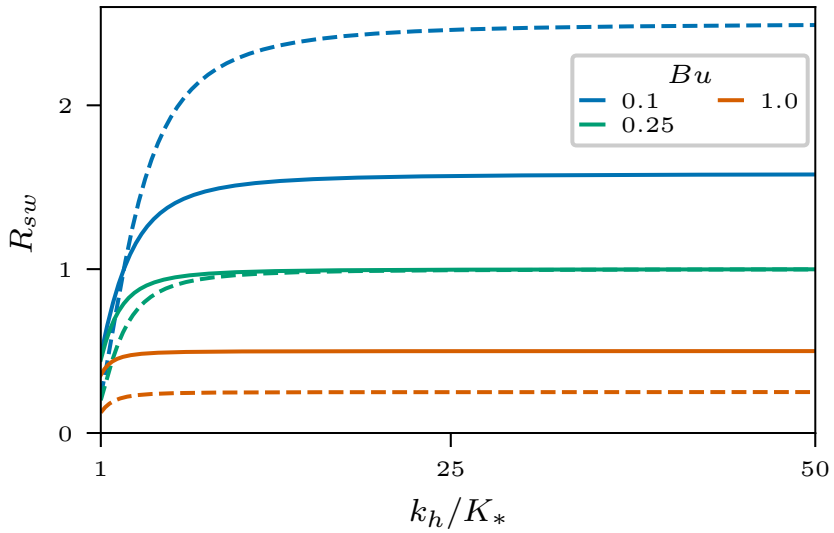

Figure 3.1: Ratio R_{sw} (solid lines) defined by (3.8), the estimated relative importance of height fluctuation and Doppler shift terms in the shallow water system, plotted for different values of the Burger number Bu against non-dimensionalised horizontal wavenumber $k_h/K_* > 1$. QG flow is $Bu = 1$. $Bu = 0.1, 0.25$ are associated with the PG regime. Dashed lines are the square of this ratio, R'_{sw} (3.46), which gives a more accurate relative importance ratio for the diffusion regime, as shown in §3.3.1.

Then, the dispersion relation is

$$\omega = \left(f^2 \cos^2\theta + N^2 \sin^2\theta\right)^{1/2} + \boldsymbol{U}\cdot\boldsymbol{k}. \tag{3.10}$$

The intrinsic frequency is the first term, dependent on θ, the angle between $\boldsymbol{k}$ and the vertical, and N is the buoyancy frequency. With uniform vertical buoyancy gradients, $N^2 = \bar{N}^2 = \text{const}$, the bare frequency coincides with the intrinsic frequency. To obtain (3.10), a WKB ansatz is substituted into the 3D Boussinesq equations. We omit the full derivation, but it follows the same method as 1.4 for the shallow water system. (See also derivations of action conservation with vertical buoyancy gradients by 1) Bretherton (1966) for gravity waves in a shear flow without the effect of rotation and; 2) Pan *et al.* (2021) for internal tides in hydrostatic balance.)

We make a rough argument for the inclusion of inhomogeneous vertical buoyancy gradients associated with the geostrophic flow in (3.10). Horizontal geostrophic balance

and vertical hydrostatic balance lead to the thermal wind balance

$$\boldsymbol{f} \times \partial_z \boldsymbol{U} = \boldsymbol{\nabla}_{\boldsymbol{x},h} B. \tag{3.11}$$

The h-subscript indicates a purely horizontal gradient. This means horizontal flow buoyancy gradients are induced by vertical shear. If the flow's vertical shear is nonlinear, vertical buoyancy gradients are also induced.

In deriving (3.10), the buoyancy frequency N^2 only appears in the equation for wave buoyancy b which is given, for negligible background flow buoyancy gradients, by

$$\partial_t b + \boldsymbol{U} \cdot \boldsymbol{\nabla}_{\boldsymbol{x}} b + N^2 w = 0. \tag{3.12}$$

Here, w is the vertical wave velocity and $N^2 = \bar{N}^2$. Gradients in $\boldsymbol{U}$ have been neglected under the WKB ansatz (see, for example, Olbers (1981)).

The full wave velocity is $\boldsymbol{u} = (u, v, w)$. Introducing flow buoyancy gradients such that $B = B(\boldsymbol{x})$, (3.12) becomes

$$\partial_t b + \boldsymbol{U} \cdot \boldsymbol{\nabla}_{\boldsymbol{x}} b + \boldsymbol{u}_h \cdot \boldsymbol{\nabla}_{\boldsymbol{x},h} B + N^2 w = 0, \tag{3.13}$$

where

$$N^2 = \bar{N}^2 + \partial_z B. \tag{3.14}$$

This is (A5) of appendix a of Chavanne *et al.* (2010). The vertical buoyancy gradient $\partial_z B$ acts as a perturbation to $\bar{N}^2$. If horizontal gradients are neglected, then (3.10) remains the same with variable N^2 defined by (3.14).

Horizontal buoyancy gradients introduce u and v terms into the buoyancy equation. This changes the nature of the eigenvalue problem for ω. It is shown in appendix B.1, not included in the submitted version of this paper, that the perturbations to the total frequency (3.10) caused by these u and v terms are imaginary. This is discussed in Chavanne *et al.* (2010) and corresponds to growing and decaying wave modes which exchange energy with the background flow. This shear instability is because buoyancy is a non-conservative force in a baroclinic fluid (Jones, 2001). Following Bretherton (1966), Olbers (1981) and Chavanne *et al.* (2010), we neglect these horizontal gradients

which amounts to an assumption of large Richardson number and leave exploration of this instability and its interaction with wavevector diffusion to future work.

Accounting for weak flow-induced vertical buoyancy gradients, we expand the dispersion relation (3.10) with N^2 given by (3.14) to obtain

$$\omega = \underbrace{\left(f^2\cos^2\theta + \bar{N}^2\sin^2\theta\right)^{1/2}}_{\omega_0} + \underbrace{\frac{\partial_z B\sin^2\theta}{2\omega_0} + \boldsymbol{U}\cdot\boldsymbol{k}}_{\omega_1}, \tag{3.15}$$

valid for small $\partial_z B/\bar{N}^2$ (in appendix B.1, we obtain this expression via an eigenvalue perturbation problem). We compare the size of the Doppler shift and buoyancy gradient terms in ω_1. We introduce the background flow aspect ratio α defined by

$$\alpha = \frac{L_*}{H_*} = \frac{K_{v*}}{K_*}, \tag{3.16}$$

for characteristic length scales $L_* = 1/K_*$ and $H_* = 1/K_{v*}$ in the horizontal and vertical respectively. Using the thermal wind relation (3.11) and aspect ratio, the buoyancy fluctuation term scales like

$$\frac{\partial_z B\sin^2\theta}{2\omega_0} \sim \frac{\alpha^2 U_* K_*\sin^2\theta}{2(\cos^2\theta + (\bar{N}^2/f^2)\sin^2\theta)^{1/2}}. \tag{3.17}$$

Thus, the ratio R_B between the buoyancy fluctuation and Doppler shift terms is roughly

$$R_\mathrm{B} = \frac{\text{buoyancy fluctuation}}{\text{Doppler shift}} \sim \frac{\alpha^2\sin\theta}{2(\cos^2\theta + (\bar{N}^2/f^2)\sin^2\theta)^{1/2}(k/K_*)}, \tag{3.18}$$

where $k = k_h/\sin\theta$ is the wavenumber magnitude. It is instructive to consider R_B as a function of non-dimensionalised frequency and horizontal wavenumber, ω_0/f and k_h/K_*:

$$R_\mathrm{B} \sim \frac{1}{2}\frac{\alpha^2}{\bar{N}^2/f^2 - 1}\frac{(\omega_0/f)^2 - 1}{\omega_0/f}\frac{1}{k_h/K_*} \approx \frac{1}{2}\left(\frac{\alpha}{\bar{N}/f}\right)^2\frac{(\omega_0/f)^2 - 1}{\omega_0/f}\frac{1}{k_h/K_*}. \tag{3.19}$$

The second expression holds for $(\bar{N}/f)^2 \gg 1$, which is true in both the atmosphere and ocean. At $\omega_0 = f$, $R_\mathrm{B} = 0$. This is to be expected: buoyancy effects are absent for vertically-propagating inertial waves. The ratio attains a maximum value of

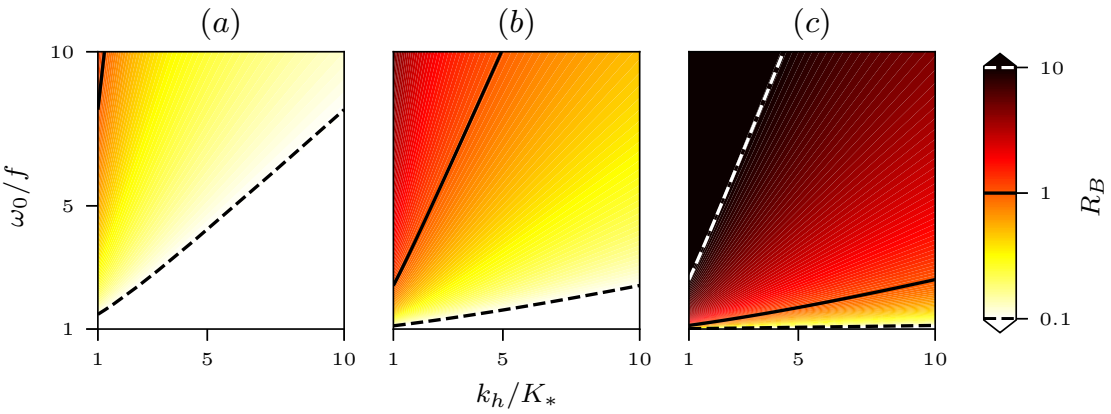

Figure 3.2: Ratio R_B as given in (3.19), the relative importance of buoyancy fluctuation and Doppler shift terms in the full Boussinesq system, against non-dimensionalised frequency ω_0/f and horizontal wavenumber k_h/K_*. Panels (a), (b) and (c) correspond to $\alpha = \bar{N}/(2f)$, $\bar{N}/f$, and $3\bar{N}/f$ respectively, with $(\bar{N}/f)^2 \gg 1$. Contours are shown for $R_\mathrm{B} = 0.1$ (dotted black), 1 (solid black) and 10 (dotted white).

$R_\mathrm{B} \sim \alpha^2(2(\bar{N}/f)(k_h/K_*))^{-1}$ when $\omega_0 = \bar{N}$. The ratio decays as $(k_h/K_*)^{-1}$. In the WKB regime we consider, $k_h/K_* \gg 1$ and so it appears justified to assume the Doppler shift term dominates. However, for large values of α or when considering the lower limit of the WKB regime, this may not be the case.

Figure 3.2 shows the ratio (3.19) for $(\bar{N}/f)^2 \gg 1$ and three values of $\alpha/(\bar{N}/f)$. We note that $\alpha \sim \bar{N}/f$ is a realistic regime for geostrophic turbulence. Contours of $R_\mathrm{B} = 0.1, 1$ and 10, corresponding to a negligible, balanced and dominant buoyancy term respectively, are given for each value of α. The buoyancy term can be equal to or greater than the Doppler shift term, namely for high aspect ratio α, higher frequencies and lower wavenumbers.

3.3 Diffusion regime

In this section, we impose statistical assumptions on slowly evolving, weak inhomogeneities to derive a spectral diffusion equation from the action conservation equation (3.1). We expand the derivation of KSV to include any total frequency of the form (3.2) assuming 1) the inhomogeneity is weak enough, that is, $\omega_1 \ll \omega_0$ (this is the weak interaction limit of statistical scattering theories such as Hasselmann (1966)); 2) the bare frequency varies slowly over $\boldsymbol{x}$ (inhomogeneity-induced $\boldsymbol{x}$-variations are accounted for

in ω_1); and 3) the inhomogeneity can be well modelled by a statistically homogeneous and stationary field. As in McComas & Bretherton (1977), Dong *et al.* (2020) and CKV, we retain time dependence in ω_1 but later will simplify to the time-independent case.

We start with the action conservation equation (3.1) with total frequency (3.2). Following §A.1 of KSV, we introduce a small bookkeeping parameter ϵ, making the substitution $\omega_1 \to \epsilon\omega_1$ to enforce the assumption that the perturbation terms are weak enough to be dominated by the bare frequency. We define slow time and space scales $\boldsymbol{X} = \epsilon^2\boldsymbol{x}$, $T = \epsilon^2 t$ and expand the action $a(\boldsymbol{x}, \boldsymbol{X}, \boldsymbol{k}, t, T)$ in powers of ϵ,

$$a = a^{(0)}(\boldsymbol{X}, \boldsymbol{k}, T) + \epsilon a^{(1)}(\boldsymbol{x}, \boldsymbol{X}, \boldsymbol{k}, t, T) + \dots \tag{3.20}$$

Allowing $a^{(0)}$ to vary only on slow time and space scales immediately satisfies the leading order equation. At $O(\epsilon)$,

$$\partial_t a^{(1)} + c_i \partial_{x_i} a^{(1)} = \partial_{x_i}\omega_1 \partial_{k_i} a^{(0)}, \tag{3.21}$$

where c_i is the i^{th} component of

$$\boldsymbol{c} = \boldsymbol{\nabla}_{\boldsymbol{k}}\omega_0, \tag{3.22}$$

the (leading order contribution to the) group velocity of the waves. This has the solution

$$a^{(1)}(\boldsymbol{x}, \boldsymbol{X}, \boldsymbol{k}, t, T) = \int_0^t \partial_{x_j}\omega_1(\boldsymbol{x} - \boldsymbol{c}s, \boldsymbol{k}, t - s)\,\mathrm{d}s\,\partial_{k_j} a^{(0)}. \tag{3.23}$$

($a^{(1)}$, the deviation from leading order wave action, is in itself useful. See, for example, Wang *et al.* (2024), in which $a^{(1)}$ is related to deviations in significant wave height of surface waves.) At $O(\epsilon^2)$, we average to eliminate $a^{(2)}$ terms and find

$$\partial_T a^{(0)} + c_i \partial_{X_i} a^{(0)} = \langle \partial_{k_i}(a^{(1)}\partial_{x_i}\omega_1)\rangle, \tag{3.24}$$

where we have used spatial homogeneity. Unlike KSV and following Villas Bôas & Young (2020), we do not require $\partial_{x_i}\partial_{k_i}\omega_1 = 0$, equivalent to incompressibility for $\omega_1 = \boldsymbol{U}\cdot\boldsymbol{k}$. We substitute (3.23) into (3.24), taking the upper bound of the integral to

be $t \to \infty$, appropriate for slowly evolving inhomogeneities. Then

$$\partial_T a^{(0)} + c_i \partial_{X_i} a^{(0)} = \partial_{k_i} \left(D_{ij} \partial_{k_j} a^{(0)} \right), \tag{3.25}$$

where

$$D_{ij} = \int_0^\infty \langle \partial_{x_i} \omega_1(\boldsymbol{x}, \boldsymbol{k}, t) \partial_{x_j} \omega_1(\boldsymbol{x} - \boldsymbol{c}s, \boldsymbol{k}, t - s) \rangle \, \mathrm{d}s, \tag{3.26}$$

with $\langle \cdot \rangle$ the ensemble average, are the components of the diffusivity tensor $\boldsymbol{D}$. Setting the bookkeeping parameter to 1 gives the diffusion equation,

$$\partial_t a + \boldsymbol{c} \cdot \boldsymbol{\nabla}_{\boldsymbol{x}} a = \boldsymbol{\nabla}_{\boldsymbol{k}} \cdot (\boldsymbol{D} \cdot \boldsymbol{\nabla}_{\boldsymbol{k}} a) \, . \tag{3.27}$$

Considering the special case of $\omega_1 = \boldsymbol{U} \cdot \boldsymbol{k}$, the diffusivity (3.26) reduces to the McComas & Bretherton (1977) diffusivity

$$D_{ij} = k_m k_n \int_0^\infty \langle \partial_{x_i} U_m(\boldsymbol{x}, t) \partial_{x_j} U_n(\boldsymbol{x} - \boldsymbol{c}s, t - s) \rangle \, \mathrm{d}s. \tag{3.28}$$

To evaluate the diffusivity, we introduce the correlation function

$$\Lambda(\boldsymbol{y}, \boldsymbol{k}, r) = \langle \omega_1(\boldsymbol{x}, \boldsymbol{k}, t) \omega_1(\boldsymbol{x} + \boldsymbol{y}, \boldsymbol{k}, t + r) \rangle, \tag{3.29}$$

and rewrite (3.26) as

$$D_{ij} = -\frac{1}{2} \int_{-\infty}^\infty \frac{\partial^2 \Lambda}{\partial y_i \partial y_j} (\boldsymbol{c}s, \boldsymbol{k}, s) \, \mathrm{d}s, \tag{3.30}$$

where we use $\Lambda(\boldsymbol{y}, \boldsymbol{k}, r) = \Lambda(-\boldsymbol{y}, \boldsymbol{k}, -r)$ to extend the limits of integration. Defining the Fourier transformed correlation function $\hat{\Lambda}$ through its inverse

$$\Lambda(\boldsymbol{x}, \boldsymbol{k}, t) = \int_{\mathbb{R}^{n+1}} \hat{\Lambda}(\boldsymbol{K}, \boldsymbol{k}, \Omega) \mathrm{e}^{\mathrm{i}(\boldsymbol{K} \cdot \boldsymbol{x} - \Omega t)} \, \mathrm{d}\boldsymbol{K} \mathrm{d}\Omega, \tag{3.31}$$

the diffusivity becomes

$$D_{ij} = \pi \int_{\mathbb{R}^{n+1}} K_i K_j \hat{\Lambda}(\boldsymbol{K}, \boldsymbol{k}, \Omega) \delta(\boldsymbol{K} \cdot \boldsymbol{c} - \Omega) \, \mathrm{d}\boldsymbol{K} \mathrm{d}\Omega, \tag{3.32}$$

where we have used that $\int_{\mathbb{R}} \exp(\mathrm{i}(\boldsymbol{K}\cdot\boldsymbol{c}-\Omega)s)\mathrm{d}s = 2\pi\delta(\boldsymbol{K}\cdot\boldsymbol{c}-\Omega)$. In the case of time-independent ω_1, this reduces to

$$D_{ij} = \pi \int_{\mathbb{R}^n} K_i K_j \hat{\Lambda}(\boldsymbol{K},\boldsymbol{k})\delta(\boldsymbol{K}\cdot\boldsymbol{c})\,\mathrm{d}\boldsymbol{K}. \tag{3.33}$$

Next, we evaluate this expression for our two example systems and in the shallow water case, support our findings with ray tracing simulations. In the Boussinesq case, we find the forced equilibrium wave energy spectrum.

3.3.1 Shallow water

To evaluate the shallow water diffusivity, we first evaluate the correlation function (3.29), then find its Fourier transform and substitute into (3.32). We introduce the background flow stream function ψ such that

$$\boldsymbol{U} = \boldsymbol{\nabla}_{\boldsymbol{x}}^{\perp}\psi = (-\partial_{x_2}\psi, \partial_{x_1}\psi, 0) \quad \text{and} \quad g\Delta H = f\psi, \tag{3.34}$$

where $\boldsymbol{\nabla}_{\boldsymbol{x}}^{\perp} = (-\partial_{x_2}, \partial_{x_1})$ is the skew gradient. Substituting this and the frequency (3.5) into (3.29) yields

$$\Lambda(\boldsymbol{y},\boldsymbol{k},r) = \underbrace{-(\boldsymbol{k}\cdot\boldsymbol{\nabla}_{\boldsymbol{y}}^{\perp})^2\langle\psi(\boldsymbol{x},t)\psi(\boldsymbol{x}+\boldsymbol{y},t+r)\rangle}_{\text{Doppler shift}} + \underbrace{\frac{f^2k_h^4}{4\omega_0^2}\langle\psi(\boldsymbol{x},t)\psi(\boldsymbol{x}+\boldsymbol{y},t+r)\rangle}_{\text{height fluctuation}}. \tag{3.35}$$

For the Doppler shift term, the skew gradients have been moved through the ensemble average using integration by parts and the symmetry of $\boldsymbol{x}$ and $\boldsymbol{y}$ arguments. Notably, there are no cross terms in (3.35) and the height fluctuation and Doppler shift effects are uncoupled. This is because, using integration by parts under the ensemble average,

$$\begin{aligned}\text{cross terms} &\propto \langle\psi(\boldsymbol{x}+\boldsymbol{y},t+r)\boldsymbol{k}\cdot\boldsymbol{\nabla}_{\boldsymbol{x}}^{\perp}\psi(\boldsymbol{x},t)\rangle + \langle\psi(\boldsymbol{x},t)\boldsymbol{k}\cdot\boldsymbol{\nabla}_{\boldsymbol{x}}^{\perp}\psi(\boldsymbol{x}+\boldsymbol{y},t+r)\rangle \\ &\propto -\langle\psi(\boldsymbol{x},t)\boldsymbol{k}\cdot\boldsymbol{\nabla}_{\boldsymbol{x}}^{\perp}\psi(\boldsymbol{x}+\boldsymbol{y},t+r)\rangle + \langle\psi(\boldsymbol{x},t)\boldsymbol{k}\cdot\boldsymbol{\nabla}_{\boldsymbol{x}}^{\perp}\psi(\boldsymbol{x}+\boldsymbol{y},t+r)\rangle \\ &= 0.\end{aligned} \tag{3.36}$$

The Fourier transform of the correlation function (3.35) is

$$\hat{\Lambda}(\boldsymbol{K},\boldsymbol{k},\Omega) = |\boldsymbol{k}\times\boldsymbol{K}|^2 E_\psi(\boldsymbol{K},\Omega) \;+\; \frac{f^2k_h^4}{4\omega_0^2}E_\psi(\boldsymbol{K},\Omega) \tag{3.37}$$

$$= 2k_h^2\sin^2\gamma E(\boldsymbol{K},\Omega) \;+\; \frac{f^2k_h^4}{2K_h^2\omega_0^2}E(\boldsymbol{K},\Omega). \tag{3.38}$$

Here, we have introduced: $E_\psi(\boldsymbol{K},\Omega)$, the Fourier transform of $\langle\psi(\boldsymbol{x},t)\psi(\boldsymbol{x}+\boldsymbol{y},t+r)\rangle$; γ, the angle between $\boldsymbol{K}$ and $\boldsymbol{k}$; and $E(\boldsymbol{K},\Omega) = K_h^2E_\psi/2$, the flow kinetic energy spectrum. Combined with (3.32), we have a diffusivity that accounts for height fluctuation effects for a time-dependent flow.

As proof of concept, we simplify to a time-independent flow. This 1) allows for inexpensive ray-tracing simulations in §3.3.2; and 2) results in a simpler form for the diffusivity. Adding time dependence is possible, as done solely for the Doppler shift effect by Dong *et al.* (2020) and – for the full 3d set-up – CKV. Combining the time-independent-flow limit of (3.38) with (3.33), we have

$$\begin{aligned} D_{ij} =& 2\pi k_h^2\int_0^\infty \mathrm{d}K_h\int_0^{2\pi}\mathrm{d}\gamma\, K_hK_iK_j\sin^2\gamma E(\boldsymbol{K})\delta(\boldsymbol{K}\cdot\boldsymbol{c}) \\ &+\frac{\pi f^2k_h^4}{2\omega_0^2}\int_0^\infty \mathrm{d}K_h\int_0^{2\pi}\mathrm{d}\gamma\,\frac{K_iK_j}{K_h}E(\boldsymbol{K})\delta(\boldsymbol{K}\cdot\boldsymbol{c}), \end{aligned} \tag{3.39}$$

in polar coordinates $\boldsymbol{K} = (K_h,\gamma)$. $E(\boldsymbol{K})$ is the flow kinetic energy spectrum marginalised over frequencies. In the local polar basis $(\boldsymbol{e}_{k_h},\boldsymbol{e}_\phi)$ associated with $\boldsymbol{k}$, this diffusivity has one non-zero component,

$$D_{\phi\phi} = \boldsymbol{e}_\phi\cdot\boldsymbol{D}\cdot\boldsymbol{e}_\phi. \tag{3.40}$$

This is because the constant frequency surface in spectral space is the circle $\omega = \omega_0(k_h) + O(\epsilon) = \text{const}$. There is no diffusion of action across this circle because for a time-independent linear system, wave frequency does not change. This means there are no radial components of the diffusivity, only (3.40). We see this explicitly by expanding $\boldsymbol{K}$ as

$$\boldsymbol{K} = K_h\cos\gamma\boldsymbol{e}_{k_h} + K_h\sin\gamma\boldsymbol{e}_\phi. \tag{3.41}$$

Then, noting $\delta(\boldsymbol{K}\cdot\boldsymbol{c}) \propto \delta(\cos\gamma)$ as $\boldsymbol{c} = \boldsymbol{\nabla}_{\boldsymbol{k}}\omega_0(k_h) = c\boldsymbol{e}_{k_h}$ shows that any integrand

containing $\cos\gamma$ integrates to zero (providing the energy spectrum $E(\boldsymbol{K})$ is well-behaved). This is the case for all components of (3.39) bar (3.40), which, using (3.41), is

$$\begin{aligned} D_{\phi\phi} = {} & 2\pi k_h^2 \int_0^\infty \mathrm{d}K_h \int_0^{2\pi} \mathrm{d}\gamma \, K_h^3 \sin^4\gamma E(\boldsymbol{K}) \delta(K_h c \cos\gamma) \\ & + \frac{\pi f^2 k_h^4}{2\omega_0^2} \int_0^\infty \mathrm{d}K_h \int_0^{2\pi} \mathrm{d}\gamma \, K_h \sin^2\gamma E(\boldsymbol{K}) \delta(K_h c \cos\gamma). \end{aligned} \tag{3.42}$$

Assuming flow isotropy such that $E(\boldsymbol{K}) = E(K_h)$, we integrate in γ to get

$$D_{\phi\phi} = \underbrace{\frac{4\pi k_h^2}{c} \int_0^\infty K_h^2 E(K_h) \, \mathrm{d}K_h}_{\text{Doppler shift}} + \underbrace{\frac{\pi f^2 k_h^4}{c\omega_0^2} \int_0^\infty E(K_h) \, \mathrm{d}K_h}_{\text{height fluctuation}}. \tag{3.43}$$

With this single component, the diffusion equation (3.27) reduces to

$$\partial_t a + \boldsymbol{c} \cdot \boldsymbol{\nabla}_{\boldsymbol{x}} a = \mu \partial_{\phi\phi} a, \tag{3.44}$$

where we define the directional diffusivity

$$\mu = D_{\phi\phi} / k_h^2. \tag{3.45}$$

(The height fluctuation diffusivity (3.43) can also be used to describe rotating shallow water waves scattered by topography. Letting ΔH be the topographical displacement from a flat bottom, we replace $E(K_h)$ in the height fluctuation term by $(gK_h/f)^2 \widehat{\langle \Delta H \Delta H \rangle}/2$, with $\widehat{\langle \Delta H \Delta H \rangle}$ the Fourier transform of the topographical correlation length $\langle \Delta H(\boldsymbol{x}) \Delta H(\boldsymbol{x} + \boldsymbol{y}) \rangle$. There are no Doppler shift-topography cross terms if velocity and topographic height are uncorrelated. With an adaption to the bare frequency, this expression could also be used to describe surface wave scattering by topography (e.g. Hasselmann, 1966; Ardhuin & Herbers, 2002) or internal tides (e.g. Bretherton & Garrett, 1968; Tolman, 1990).)

To examine the relative importance of each term in (3.43), we consider the ratio

between the two,

$$R'_{\mathrm{sw}} = \frac{\left[D_{\phi\phi}\right]_{\text{height fluctuation}}}{\left[D_{\phi\phi}\right]_{\text{Doppler shift}}} = \frac{f^2 k_h^2}{4\omega_0^2} \frac{\int_0^\infty E(K_h)\,\mathrm{d}K_h}{\int_0^\infty K_h^2 E(K_h)\,\mathrm{d}K_h} \sim \frac{(k_h/K_*)^2}{4(1+Bu\,(k_h/K_*)^2)}, \tag{3.46}$$

where we approximate the ratio of the two integrals as the square of the characteristic horizontal wavenumber of the flow, K_*. The final expression in (3.46) is the square of the scaling argument estimate R_{sw} (3.8) which comes from the wave dispersion relation. This is sensible – the diffusivity (3.26) consists of a square frequency term. This means that in the diffusion regime, the scaling argument of §3.2.1 is an underestimate for $R_{\mathrm{sw}} > 1$ and overestimate for $R_{\mathrm{sw}} < 1$. In figure 3.1, the adjustment from R_{sw} to R'_{sw} is shown.

3.3.2 Shallow water ray tracing

The 2D diffusion equation (3.44) has an exact solution as outlined in §4 of Villas Bôas & Young (2020). We use this solution and ray tracing – a numerical method to find constant-wave-action trajectories – to assess the validity of the diffusion approximation and form of the diffusivity (3.43).

We start by multiplying the diffusion equation by $\cos\phi$ and integrating over the entire (x, y)-plane and $\phi \in (-\pi, \pi)$ to get

$$\frac{\mathrm{d}}{\mathrm{d}t} \iiint \cos\phi\, a\, \mathrm{d}x\mathrm{d}y\mathrm{d}\phi = -\mu \iiint \cos\phi\, a\, \mathrm{d}x\mathrm{d}y\mathrm{d}\phi. \tag{3.47}$$

Note that without pre-multiplying by $\cos\phi$, the left-hand side is zero by action conservation. Here, the $\boldsymbol{c}\cdot\boldsymbol{\nabla}_{\boldsymbol{x}} a$ term disappears under the (x, y) integrals because the a we consider is ensemble averaged and we assume statistical spatial homogeneity in deriving the diffusion equation. Integrating with respect to time yields

$$\ln\left(\langle\cos\phi\rangle_a\right) = -\mu t + \ln\left(\langle\cos\phi_0\rangle_a\right), \tag{3.48}$$

where $\langle\cdot\rangle_a$ denotes the action-weighted ensemble average and ϕ_0 is the initial angle. This is an alternative form of (4.3) in Villas Bôas & Young (2020).

We confirm that (3.48) holds by ray tracing: solving the characteristic equations

of the action conservation equation (3.1) numerically to give many constant-action trajectories and taking an ensemble average. These ray equations are

$$\partial_t \boldsymbol{x} = \boldsymbol{\nabla}_{\boldsymbol{k}}\omega, \quad \text{and} \quad \partial_t \boldsymbol{k} = -\boldsymbol{\nabla}_{\boldsymbol{x}}\omega. \tag{3.49a,b}$$

We define non-dimensional quantities

$$t' = tf, \quad \boldsymbol{k}' = \boldsymbol{k}/K_*, \quad \boldsymbol{x}' = \boldsymbol{x}K_*, \quad \text{and} \quad U' = \boldsymbol{U}/U_*, \tag{3.50a–d}$$

(and $\psi' = \psi K_*/U_*$). Substituting the approximate frequency for shallow water waves (3.4) into (3.49a,b) gives

$$\partial_{t'}\boldsymbol{x}' = \frac{Bu}{(1+Buk_h'^2)^{1/2}}\boldsymbol{k}' + Ro\boldsymbol{U}' + Ro\frac{2+Buk_h'^2}{2(1+Buk_h'^2)^{3/2}}\psi'\boldsymbol{k}', \tag{3.51a}$$

$$\partial_{t'}\boldsymbol{k}' = \underbrace{0}_{\text{no flow}} \underbrace{- Ro\boldsymbol{\nabla}_{\boldsymbol{x}'}(\boldsymbol{U}'\cdot\boldsymbol{k}')}_{\text{Doppler shift}} \underbrace{- Ro\frac{k_h'^2}{2(1+Buk_h'^2)}\boldsymbol{U}'^{\perp}}_{\text{height fluctuation}}, \tag{3.51b}$$

where

$$Ro = \frac{U_*K_*}{f} \tag{3.52}$$

is the flow Rossby number and we introduce $\boldsymbol{U}^{\perp} = (V, -U, 0)$. Note $\boldsymbol{x}$ is non-dimensionalised by the characteristic wavenumber of the flow $K_* = 2\pi/L_*$, not by the wavenumber associated with the size of the domain $\boldsymbol{x} = L$. The quantity L/L_* is approximately the number of vortices in the domain.

The rays propagate in a flow which is a snapshot of a fully-evolved 2D quasi-geostrophic Navier-Stokes simulation, solved using a pseudo-spectral method and Crank-Nicholson time-stepping with time-step $\mathrm{d}t = 0.01$. The simulation has a dealiasing mask which forces the nonlinear terms to be zero for flow horizontal wavenumbers $K_x > 2/3 \times \mathrm{Max}(K_x)$ and vertical wavenumbers $K_y > 2/3 \times \mathrm{Max}(K_y)$. This prevents aliasing the energy of small-scale modes to larger scale modes which could result in instabilities. The doubly periodic domain $[0, 2\pi L/L_*]^2$ is discretised by 1024^2 gridpoints

so that relatively small-scale turbulent motions are resolved. Viscosity is $\nu = 10^{-5}$, in line with our simulation resolution. The initial wavenumber distribution of the flow is Gaussian. This is evolved to the point that statistics are as expected for a 2D QG flow – we have a K_*^{-3} energy spectrum – but not so long that energy concentrates at larger scales due to the inverse cascade. We prescribe 9 values of the Rossby radius of deformation $L_D = Bu^{1/2}/K_*$ and 3 values of the initial wavenumber K_* to give 3^3 flows. This gives final snapshots with varying Ro and Bu. A typical flow is shown in panel (a) of figure 3.3.

We perform ray simulations with the inhomogeneity ω_1 given by (a) Doppler shift only; (b) height fluctuation only and; (c) both Doppler shift and height fluctuation. In appendix B.2, we show that the absolute frequencies ω of the rays are conserved for our simulation. This should be the case – the ray equations (3.49a,b) are Hamilton's equations for the Hamiltonian ω which is conserved along the rays because it has no explicit time dependence.

We initialise 50^2 rays equally distributed across the periodic $\boldsymbol{x}$-domain with a constant horizontal wavenumber $k_h \approx 32.2K_*$ (within the WKB regime in which the characteristic length scale of the waves is orders of magnitude smaller than that of the flow) and random initial angle. By giving the rays different initial angles, our rays sample more of the flow and the ensemble average approaches the exact solution more rapidly as the number of rays increases than it would with a constant initial angle. For simplicity, we consider the angle ϕ to be the angle of deviation from the ray's initial angle meaning $\ln(\langle\cos\phi_0\rangle_a) = 0$. This is possible because of the flow's statistical isotropy. The angle of deviation for each ray is calculated at each time-step, and $\cos\phi$ is averaged over. We choose action $a = 1$ for each ray so that $\langle\cdot\rangle_a$ and the ensemble average are identical. Some of the 3^3 flows have very similar Burger or Rossby numbers; we average over these Burger and Rossby numbers to leave 3^2 results with distinct Burger and Rossby numbers. We estimate μ, (3.45), the negative gradient of $\ln(\langle\cos\phi\rangle_a)$ against time t with $D_{\phi\phi}$ computed from (3.43). We compare this to the simulation gradient.

An example ray tracing simulation is shown in figure 3.3. Panel 3.3(a) shows a sample of 10 rays in physical space superimposed on the flow vorticity field. The reduced number of rays is for ease of interpretation. The Rossby number of the flow is the small

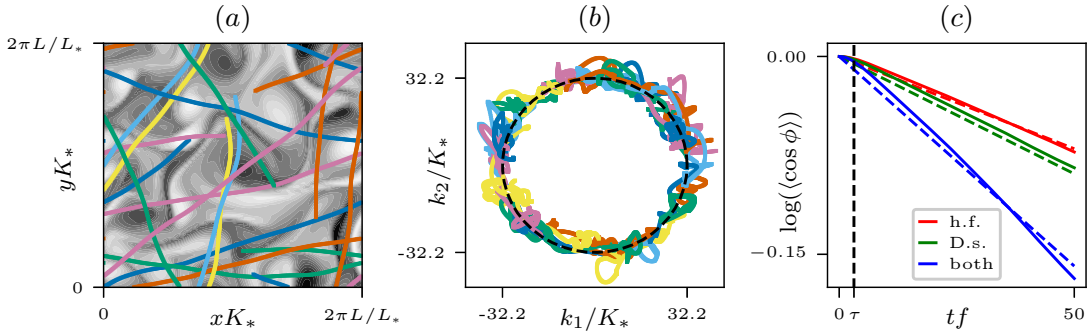

Figure 3.3: Ray trajectories satisfying the characteristic equations (3.51a)–(3.51b), propagating in the flow described in §3.3.2 with $Ro = 0.03$, $Bu = 0.32$ and $K_* = 3.10$. Panel (a) shows a sample of 10 rays in physical space superimposed on the flow vorticity field (darker sections indicate higher-magnitude vorticity). Panel (b) shows a sample of 50 rays in spectral space initialised on a constant-frequency circle given by the dotted black line. Panel (c) gives the exact solution (3.48) approximated by the rays' ensemble average (solid lines) and the diffusivity (3.43) (dashed lines). Red lines are calculated solely with the height fluctuation terms in (3.43) and (3.51a)–(3.51b); green lines are solely Doppler shift and; blue lines are the entire system with both Doppler and height fluctuation effects. The vertical dashed line indicates τ, the point at which the gradient calculation for figure 3.4 begins.

parameter in §3.3, $\epsilon \sim Ro \sim O(0.01)$, and so the flow is weak and the rays are only slightly deflected from their initial angle of propagation. Panel 3.3(b) shows a larger sample of 50 rays from the same simulation in wavevector space. The rays are initialised on a constant-frequency ring and their deviation from this ring is characterised by the small Rossby number. For the full 50^2-ray simulation, the exact solution and simulation approximation of (3.48) are shown in figure 3.3(c) for contributions from height fluctuations, Doppler shift and both effects combined. The simulation approximates the gradients and magnitudes of the exact solutions reasonably well and this corroborates the diffusion approximation and the formulas (3.43). As expected from these formulas, the height fluctuations and Doppler shift make comparable contributions to the spectral diffusivity.

The Ro and Bu dependence of μ can be seen from (3.43). We define the non-dimensional directional diffusivity $\tilde{\mu}$ as

$$\tilde{\mu} = \frac{Bu^{1/2}}{fRo^2}\mu \sim \underbrace{\frac{(\omega_0/f)}{Bu^{1/2}(k_h/K_*)}}_{\text{Doppler shift}} + \underbrace{\frac{(k_h/K_*)}{4Bu^{1/2}(\omega_0/f)}}_{\text{height fluctuation}} \to \underbrace{1}_{\text{D.s.}} + \underbrace{(4Bu)^{-1}}_{\text{h.f.}}, \tag{3.53}$$

where we have used that

$$2\pi \int_0^\infty K_h^2 E(K_h)\,\mathrm{d}K_h \sim K_* U_*^2/2 \quad \text{and} \quad 2\pi \int_0^\infty E(K_h)\,\mathrm{d}K_h \sim U_*^2/(2K_*). \tag{3.54a,b}$$

The final limit of (3.53) holds for $(k_h/K_*)^2 \gg 1$. Note the ratio between height fluctuation and Doppler shift effects is in agreement with R'_{sw}, (3.46). In figure 3.4, $\tilde{\mu}$ is displayed for a range of Burger numbers. The Burger dependence of (3.53) is confirmed for each contribution and, because 3 separate Rossby numbers are used in the plot, so too is the Rossby dependence.

The characteristic flow velocity U_* is chosen such that the first expression of (3.54a,b) holds exactly and $\tilde{\mu} = 1$ is the exact limit of the non-dimensionalised, Doppler shift directional diffusivity. Then the height fluctuation $\tilde{\mu}$ shown in figure 3.4 coincides with the ratio between the height fluctuation and Doppler shift effects R'_{sw}. We see good agreement between the height fluctuation $\tilde{\mu}$ computed exactly and from simulations and thus confirm our estimate of R'_{sw} given by (3.46).

In deriving the diffusivity (3.26), we approximate an integral between 0 and t by one between 0 and ∞ and so there is a delay between the start of the ray simulation to the point at which the exact solution (3.48) is well approximated. Therefore, our μ estimates in figure 3.4 begin a short time τ/f after the simulations have begun, as indicated in figure 3.3(c).

We stress that the good agreement in figures 3.3(c) and 3.4 between the μ (3.45) computed from the diffusivity (3.43) and the μ of (3.48) estimated from the ensemble average of rays validates the diffusion approximation (3.44) of the action conservation equation (3.1) with inhomogeneities of the form (3.5).

3.3.3 3D Boussinesq

The method to evaluate the general diffusivity (3.32) for a Boussinesq system with vertical buoyancy gradients is similar to the shallow water system. We give the result here, providing a full derivation in appendix B.3.1. For a Doppler-shift-induced diffusivity, CKV show that it is well justified to assume a slowly evolving flow is time independent. The same likely applies to a buoyancy-gradient-induced diffusivity, so we focus on the

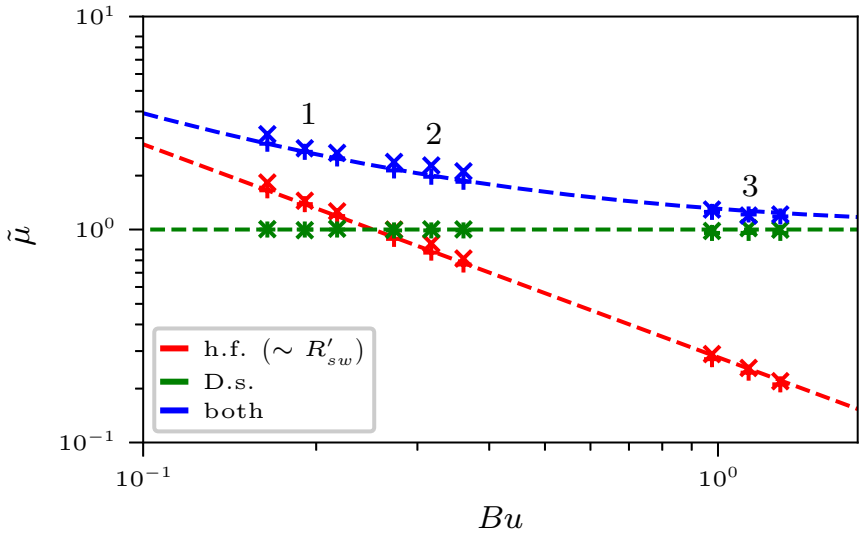

Figure 3.4: Non-dimensional directional diffusivity $\tilde{\mu}$, as defined by (3.45) and (3.53), plotted against flow Burger number Bu. Red lines correspond to the height fluctuation component of the directional diffusivity, green lines to the Doppler shift component and blue lines to the full directional diffusivity. Crosses indicate the estimates of $\tilde{\mu}$ from the 50^2-ray simulations and exact solution (3.48), pluses are computed from the diffusivity expression (3.43) and dotted lines are the power laws predicted by (3.53), fitted to the first of the exact data points. The 9 different Burger numbers cover 3 sets of Rossby number, labelled 1 ($Ro \approx 0.023$), 2 ($Ro \approx 0.030$) and 3 ($Ro \approx 0.057$). The Doppler shift directional diffusivity $\tilde{\mu} \approx 1$ and so the height fluctuation directional diffusivity corresponds to the ratio between the two, R'_{sw} (3.46).

time-independent case.

The two non-zero components of the diffusivities for a Boussinesq system with vertical buoyancy gradients and dispersion relation (3.15) are

$$D_{kk} = \frac{4\pi k^3 \omega_0 \sin^2\theta}{(\bar{N}^2 - f^2)|\cos^5\theta|} \left\{ \int_0^\infty \int_\theta^{\pi-\theta} K^3 \cos^2\Theta (\cot^2\theta - \cot^2\Theta)^{1/2} E(K,\Theta)\, \mathrm{d}K\mathrm{d}\Theta \right\} \text{Doppler shift}$$
$$+ \frac{\pi k f^2 \sin^2\theta}{\omega_0(\bar{N}^2 - f^2)|\cos^3\theta|} \left\{ \int_0^\infty \int_\theta^{\pi-\theta} \frac{K^5 \cos^6\Theta E(K,\Theta)}{\sin^2\Theta(\cot^2\theta - \cot^2\Theta)^{1/2}}\, \mathrm{d}K\mathrm{d}\Theta \right\} \text{buoyancy fluctuation,} \tag{3.55}$$

and

$$D_{\phi\phi} = \frac{4\pi k^3 \omega_0 \sin^4\theta}{(\bar{N}^2 - f^2)|\cos^5\theta|} \left\{ \int_0^\infty \int_\theta^{\pi-\theta} K^3 \sin^2\Theta (\cot^2\theta - \cot^2\Theta)^{3/2} E(K,\Theta)\, \mathrm{d}K\mathrm{d}\Theta \right\} \text{Doppler shift}$$
$$+ \frac{\pi k f^2 \sin^4\theta}{\omega_0(\bar{N}^2 - f^2)|\cos^3\theta|} \left\{ \int_0^\infty \int_\theta^{\pi-\theta} K^5 \cos^4\Theta (\cot^2\theta - \cot^2\Theta)^{1/2} E(K,\Theta)\, \mathrm{d}K\mathrm{d}\Theta \right\} \text{b.f.,} \tag{3.56}$$

where we use polar coordinates $\boldsymbol{K} = (K, \gamma, \Theta)$ for the background flow and E is the flow kinetic energy spectrum, as defined in the shallow water case. Here, $\gamma = \Phi - \phi$ is the angle between the horizontal components of $\boldsymbol{K}$ and $\boldsymbol{k}$. The Doppler shift and buoyancy fluctuation diffusivities are uncoupled, as with the inhomogeneities in the shallow water system. This is true of a time-dependent background flow also (see appendix B.3.1).

Only the kinetic energy spectrum of the flow appears in (3.55)–(3.56) because we assume thermal wind balance. More generally, the diffusivity will be expressed in terms of both potential and kinetic energy spectra.

The $(\cot^2\theta - \cot^2\Theta)^{-1/2}$ factor in the integrand of the buoyancy fluctuation term of D_{kk} behaves like $\delta^{-1/2}$ a small distance δ from the singularities at $\Theta = \theta, \pi - \theta$. Therefore, it is integrable and does not cause the diffusivity to diverge.

Only the part of the flow spectrum with wavevectors of polar angle $\Theta \in (\theta, \pi - \theta)$ contributes to the diffusivity integrals. IGW diffusion is a sub-regime of IGW scattering. This triadic interaction occurs between an incident wave $\boldsymbol{k}$ and the background flow $\boldsymbol{K}$, resulting in a scattered wave $\boldsymbol{k}'$ of the same frequency. In wavevector space, $\boldsymbol{k} + \boldsymbol{K} = \boldsymbol{k}'$. As the incident wave and scattered wave are of the same frequency, $\boldsymbol{K}$ connects two

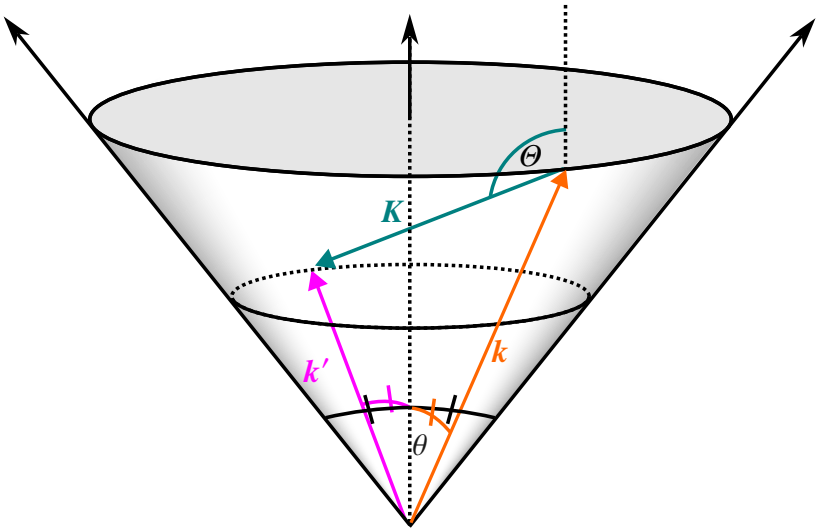

Figure 3.5: Schematic of the scattering interaction between an incident wave $\boldsymbol{k}$ and the background flow $\boldsymbol{K}$ resulting in a scattered wave $\boldsymbol{k}'$. The two waves have the same frequency $\omega_0(\theta)$ and thus the background flow connects two points on the constant-frequency cone. For an arbitrary scattering interaction, angle Θ of the flow's wavevector is bounded between θ and $\pi - \theta$ i.e. the angular range of a vector between any two points on the cone.

points on the cone of constant frequency. Thus, the range of the $\boldsymbol{K}$'s polar angle Θ is the range of angles connecting any two points on the cone i.e. $(\theta, \pi - \theta)$. This is demonstrated in figure 3.5. Significantly, waves of frequency $\omega_0(\theta)$ will not be scattered by flow fluctuations with wavevectors outside of these angle bounds, regardless of the flow's energy.

These invisible flow regions make it difficult to apply the scaling argument of §3.2.2. The polar angle of the characteristic wavevector of the flow $\boldsymbol{K}_*$ does not necessarily lie within $(\theta, \pi - \theta)$, in which case R_B (3.18) computed at $\boldsymbol{K}_*$ is not meaningful. Instead, a dominant wavevector – the characteristic wavevector of the portion of the flow which scatters the waves – must be used.

We define R'_B as the ratio between the buoyancy fluctuation and Doppler shift diffusivites for radial and azimuthal components,

$$R'_{\mathrm{B},kk} = \frac{[D_{kk}]_{\text{buoy. fluct.}}}{[D_{kk}]_{\text{Doppler shift}}} \quad \text{and} \quad R'_{\mathrm{B},\phi\phi} = \frac{[D_{\phi\phi}]_{\text{buoy. fluct.}}}{[D_{\phi\phi}]_{\text{Doppler shift}}}. \tag{3.57a,b}$$

Both ratios scale like $(k_h/K_*)^{-2}$ through the diffusivity prefactors' k dependence.

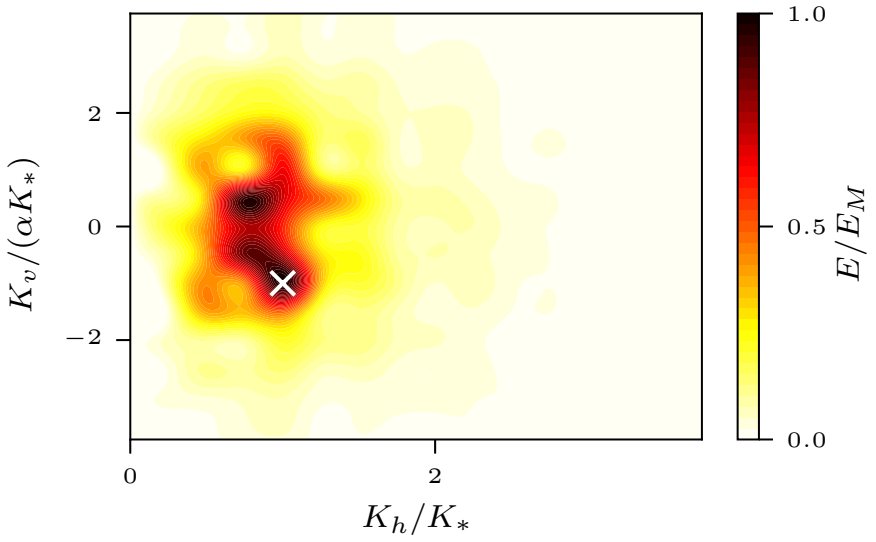

Figure 3.6: The geostrophic flow component E, smoothed and scaled by a maximum value E_M, of the full Boussinesq simulation in CKV. The horizontal and vertical flow wavenumbers (K_h, K_v) are scaled by the characteristic wavevector $(K_h, K_v) = (K_*, \alpha K_*)$ – with α the aspect ratio of the flow (3.16) – marked by a white cross, at which the geostrophic energy is maximum.

The frequency behaviour is more complicated, requiring the diffusivity integrals to be evaluated. In appendix B.3.2, we show that $R'_{\mathrm{B},kk} \to 0$ for $\omega_0/f \to 1$ and for larger frequencies and high aspect ratios α (3.16), $R'_{\mathrm{B},kk} \sim (\omega_0/f)^{-2}$. This means that for waves in the WKB regime with high aspect ratios and frequencies, vertical buoyancy gradients can be neglected.

We compute the ratio of diffusivity components for a typical quasi-geostrophic flow and find good agreement with the -2 power laws. The geostrophic energy spectrum used is extracted from a snapshot of the full Boussinesq simulation described in CKV and is pictured in figure 3.6. For this spectrum, $N/f = 32.0$ and the aspect ratio, (3.16), $\alpha \approx 16.0$.

Both ratios of diffusivities are shown in figure 3.7, computed with the energy spectrum of figure 3.6. In figure 3.8, for the radial diffusivity ratio, we plot cross sections of constant frequency and horizontal wavenumber and find good agreement with the -2 power laws.

The values of $R_{\mathrm{B},kk}$ and $R_{\mathrm{B},\phi\phi}$ are, for the WKB regime of $k_h/K_* \gg 1$, $\lesssim 0.1$. Thus, at least for the waves in CKV, we predict a weak vertical buoyancy gradient

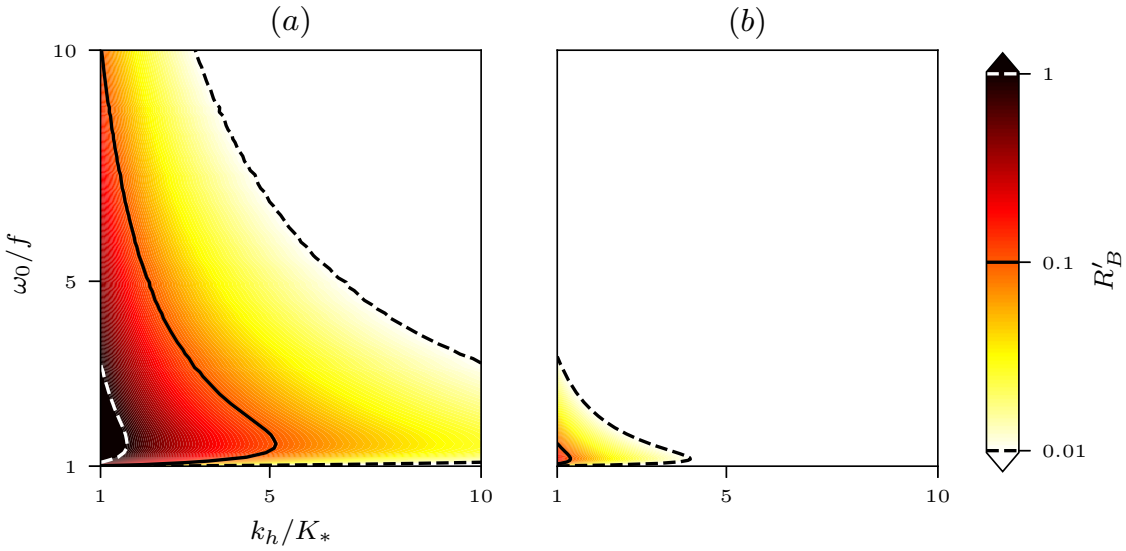

Figure 3.7: Radial and azimuthal ratios (a) $R'_{\mathrm{B},kk}$ and (b) $R'_{\mathrm{B},\phi\phi}$ as given in (3.57a,b), the ratio of buoyancy fluctuation and Doppler shift diffusivities for a snapshot of the full Boussinesq simulation of CKV, against non-dimensionalised frequency ω_0/f and horizontal wavenumber k_h/K_*. Contours are shown for $R_\mathrm{B} = 0.01$ (dotted black), 0.1 (solid black) and 1 (dotted white).

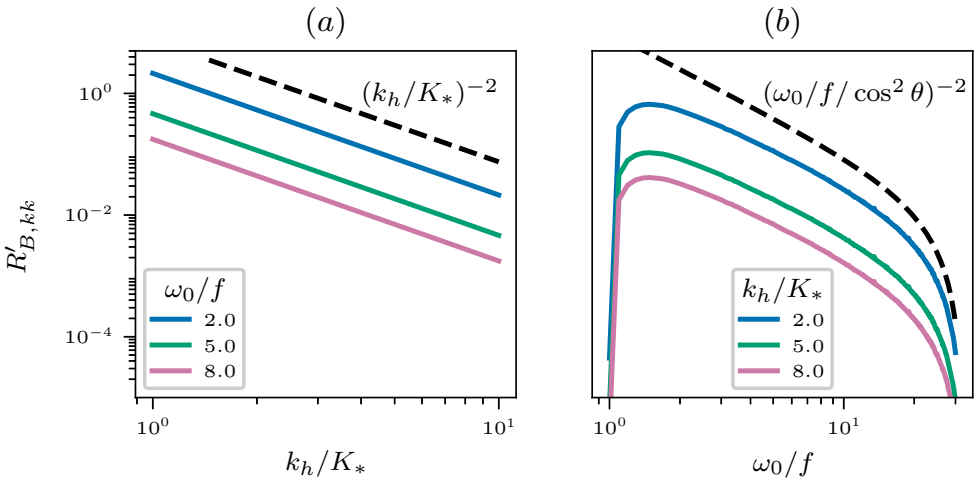

Figure 3.8: Cross sections of radial ratio $R'_{\mathrm{B},kk}$ (3.57a,b), as shown in figure 3.7, for constant (a) ω_0/f and (b) k_h/K_*. The $(\omega_0/f/\cos^2\theta)^{-2}$ prediction of appendix B.3.2 is, for small θ, an $(\omega_0/f)^{-2}$ power law.

induces negligible spectral diffusion in the WKB regime.

Figure 3.7, a comparison of diffusivity magnitudes, is markedly different to the comparison of dispersion relation terms, figure 3.2. Although both predict a decrease in the buoyancy fluctuation effect as horizontal wavenumber increases, the scaling argument of §3.2.2 predicts the effect dominates for higher frequencies. The $(\omega_0/f)^{-2}$ power law predicted from diffusivities and confirmed for an example spectrum in figure 3.8 contradicts this. We attribute this conflicting prediction to the large part of the flow spectrum not contributing to the diffusivity at higher wave frequencies. This makes the scaling arguments of §3.2.2 unreliable and calls for the exact evaluation of the diffusivities (3.55)–(3.56).

3.3.4 Forced equilibrium spectrum

We solve the diffusion equation (3.27) exactly in the time-independent case corresponding to the equilibrium spectrum obtained under constant forcing. Our aim is to assess how the $k^{\pm 2}$ power law spectra obtained by KSV when diffusion is solely caused by Doppler shift is modified when accounting for vertical buoyancy gradients. As in KSV, we focus on radial diffusion, assuming wave statistics independent of ϕ such that $\partial_\phi a = 0$. To concisely contrast this work to theirs, we consider only the forced, equilibrium solution to (3.27). We consider the energy density for ease of interpretation, defined as $e(k;\theta) = 2\pi k^2 \sin\theta \omega a(k;\theta)$, such that $e\,\mathrm{d}k\mathrm{d}\theta$ is the energy contained in the box $[k, k+\mathrm{d}k]$ and $[\theta, \theta+\mathrm{d}\theta]$. Thus, ignoring unimportant prefactors on the right-hand side, (3.27) becomes

$$\partial_k \left(k^2 D_{kk} \partial_k \frac{e}{k^2} \right) = -\delta(k - k_*). \tag{3.58}$$

The forcing in a circle at $k = k_*$ can be generalised via integration. The minus sign ensures a positive energy spectrum. Defining

$$Q = k^3 [D_{kk}]_{\text{Doppler shift}} \quad \text{and} \quad P = k [D_{kk}]_{\text{buoyancy fluctuation}} \tag{3.59}$$

as the k-independent parts of the Doppler shift and buoyancy fluctuation diffusivities, this simplifies to

$$Q\partial_k\left(\left(k^5+\beta k^3\right)\partial_k\frac{e}{k^2}\right)=-\delta(k-k_*), \tag{3.60}$$

where $\beta = P/Q$. This equation has the piece-wise solution found, for example, by partial fractions,

$$e(k)=\begin{cases} A\left(1-\frac{k^2}{\beta}\ln\left(1+\frac{\beta}{k^2}\right)\right)+Bk^2 & \text{for } 0<k<k_* \\ C\left(1-\frac{k^2}{\beta}\ln\left(1+\frac{\beta}{k^2}\right)\right)+Dk^2 & \text{for } k>k_* \end{cases}. \tag{3.61}$$

We require $e(k)$ is bounded as $k\to\infty$ which means $D=0$. We require zero energy at $k=0$, therefore $A=0$. Continuity at $k=k_*$ gives $B=C(1/k_*^2-\ln(1+\beta/k_*^2)/\beta)$. The jump condition $[Q\left(k^5+\beta k^3\right)\partial_k\frac{e}{k^2}]_{k_*^-}^{k_*^+}=-1$ gives $C=1/(2\beta Q)$. Thus,

$$e(k)=\frac{1}{2\beta Q}\begin{cases} \frac{k^2}{k_*^2}\left(1-\frac{k_*^2}{\beta}\ln\left(1+\frac{\beta}{k_*^2}\right)\right) & \text{for } 0<k<k_* \\ 1-\frac{k^2}{\beta}\ln\left(1+\frac{\beta}{k^2}\right) & \text{for } k>k_* \end{cases}. \tag{3.62}$$

Note that $Q\to 0$ is an artificial singularity introduced by the choice of factorisation and forcing in (3.60). The Doppler shift limit of $\beta\to 0$ is

$$e(k)=\frac{1}{4Qk_*^2}\begin{cases} (k/k_*)^2 & \text{for } 0<k<k_* \\ (k_*/k)^2 & \text{for } k>k_* \end{cases}, \tag{3.63}$$

which is exactly (4.1) of KSV. The buoyancy fluctuation limit of $\beta\to\infty$ is

$$e(k)=\frac{1}{2P}\begin{cases} (k/k_*)^2 & \text{for } 0<k<k_* \\ 1 & \text{for } k>k_* \end{cases}. \tag{3.64}$$

In figure 3.9, (3.62)–(3.64) are displayed for two values of β/k_*^2.

The finite energy at $k\to\infty$ of (3.64) is unphysical. However, this solution is unstable in the sense that a vanishingly small Doppler shift contribution will result in $e(k)\to 0$ as $k\to\infty$. This is because the limit of (3.62) as $k\to\infty$, $\beta=o(k)$ is $e(k)\to 1/(4Qk^2)$ i.e. the Doppler shift limit (3.63) for $k>k_*$. This can be seen in figure 3.9 (b). If a buoyancy fluctuation is present, so too is the Doppler shift term by the thermal wind balance (3.11) which means that the $k>k_*$ limit of (3.64) never

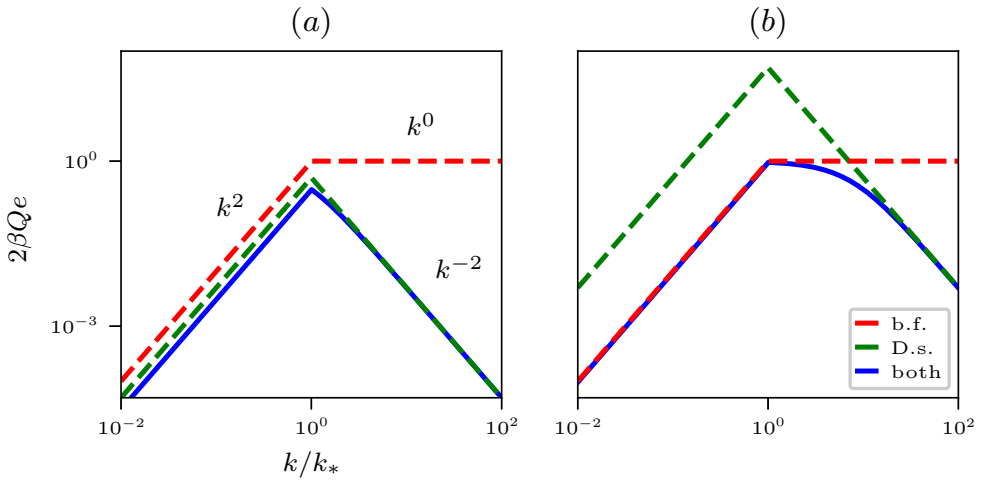

Figure 3.9: Forced equilibrium spectra (3.62)–(3.64) against non-dimensionalised wavenumber for two different values of $\beta/k_*^2 = P/(Qk_*^2)$ (3.59), the k/k_*-independent ratio of buoyancy-induced and Doppler-shift-induced diffusivities. (a) $\beta/k_*^2 = 1$ corresponds to a diffusivity with equal contributions from buoyancy fluctuations and Doppler shift and; (b) $\beta/k_*^2 = 100$ corresponds to a buoyancy-fluctuation-dominated diffusivity. Diffusion by both effects is given in blue (3.62), whilst red and green lines are spectra derived from only the buoyancy and Doppler shift terms respectively, given by (3.64) and (3.63).

occurs and the energy spectrum will always decay for large k under Doppler shift.

Figure 3.9 shows how buoyancy fluctuations affect the spectrum amplitude, mainly for $k < k_*$. For a Doppler-shift-dominated diffusivity ($\beta \to 0$), this amplitude change is negligible. For $k > k_*$, buoyancy fluctuations shallow the Doppler-shift-induced energy spectrum of KSV for a small range of intermediate wavenumbers.

The scaling argument of §3.2.2 and the ratio of radial diffusivity (3.55) predict the buoyancy-induced diffusivity decays to zero for large k/K_* and thus the effect of vertical buoyancy gradients is then small. Our findings in this section compound this prediction because 1) a small buoyancy-induced diffusivity has negligible impact on the wave energy spectrum for any wavenumber and; 2) any buoyancy-induced diffusivity has negligible impact on the wave energy spectrum for large k_h/K_*.

3.4 Discussion

Scattering by turbulent flow leads to the diffusion of inertia-gravity-wave energy in spectral space. In previous work on the topic (McComas & Bretherton, 1977; Kafiabad

et al., 2019; Savva, 2020; Dong *et al.*, 2020; Cox *et al.*, 2023) the mechanism for spectral wave diffusion is a Doppler shift term in the waves' dispersion relation. In this paper, we argue at the level of the dispersion relation that other mechanisms can cause significant wave diffusion. We provide two examples: a fluctuation in the mean height of a rotating shallow water system due to the background geostrophic flow, and an effective variation in buoyancy frequency for the 3D Boussinesq system, caused by vertical background flow buoyancy gradients. There is precedent for this – Chavanne *et al.* (2010) find refraction by vertical buoyancy gradients to be more significant than the Doppler shift effect in the context of internal tides.

We generalise the derivation of Kafiabad *et al.* (2019) to give a diffusion equation valid for any slowly evolving, weak inhomogeneities the waves encounter. For our two examples, we evaluate the corresponding diffusivity.

In the Boussinesq case, we confirm the buoyancy-fluctuation effect can be significant although as waves diffuse to higher wavenumbers, we find this effect is greatly reduced. We also find a reduction for higher frequency waves and background flows with large aspect ratios between horizontal and vertical motions, as is the case in the ocean.

We solve the steady-state diffusion equation and find the resulting energy spectrum agrees with this conclusion – as the waves move further into the WKB regime, the ratio between buoyancy fluctuation and Doppler shift effects decays to zero.

Scaling predictions from the Boussinesq dispersion relation of the relative importance of Doppler shift and vertical buoyancy gradients differ, with respect to wave frequency, to those found from the complete computation of the diffusivities. This is because large parts of the flow energy spectrum which do not meet the relevant resonance condition cannot contribute to scattering the waves.

In the shallow water system, we find that for small Burger numbers the height-fluctuation diffusivity is comparable to or larger than the Doppler-shift diffusivity. This is supported by ray simulations which (a) validate the diffusion approximation of the action conservation equation and; (b) confirm the relative magnitude of the height fluctuation and Doppler shift effects. We note that the Burger number does not have to be vanishingly small for the height fluctuation effect to be significant – at $Bu = O(1)$, the two effects differ only by a factor of $1/4$.

Remarkably, the Doppler shift effect is decoupled from the other diffusion mecha-

nisms in the shallow water and Boussinesq diffusion equations. This occurs despite the Doppler shift being related to these other effects through the geostrophic and thermal wind balances. Uncorrelated effects will also be uncoupled from the Doppler shift. For example, shallow water waves scattered by topography, for which the corresponding diffusivity can be inferred from our height fluctuation diffusivity in §3.3.1.

Our work is relevant to internal tides which, alongside near-inertial waves, dominate the IGW energy spectrum (Ferrari & Wunsch, 2009). Previous work uses ray tracing to model internal tide energy distributions and finds good agreement with observation despite marginal scale separation between the tides and background eddies (Park & Watts, 2006; Rainville & Pinkel, 2006; Chavanne *et al.*, 2010). Furthermore, if internal tides propagate through a barotropic background flow, they form a set of uncoupled shallow water equations (e.g. Savva & Vanneste, 2018). Beyond this, it is clear that our approach applies for any waves propagating through large-scale inhomogeneities.

A possible application of the formula we obtain for the spectral diffusivity is to the representation of the impact of unresolved turbulence on inertia-gravity waves parameterised in atmosphere and ocean models. In ray-tracing modules such as MS-GWaM (Bölöni *et al.*, 2021; Kim *et al.*, 2021), the diffusion could be included by means of additional white-noise terms in the wavevector ray equation, leading to a stochastic parameterisation grounded in the physics of wave–flow interactions.

The diffusion regime is characterised by the weak-interaction assumption of statistical scattering and the WKB approximation. In the case of Doppler-shift-induced diffusion, the weak interaction assumption is equivalent to a weak-flow approximation: the group speed of the waves is much greater than the characteristic background flow speed, $c \gg U_*$. The region of validity for which $c \gg U_*$ is illustrated in §2.5. Outside of the diffusion regime, markedly different behaviour is observed. Dong, Bühler & Smith (2023) ray trace IGWs initialised with the same frequency through 3D background flows. To begin with, wave energy is confined close to this frequency, consistent with the findings of Kafiabad *et al.* (2019) and Cox *et al.* (2023). Over longer times, wave energy spreads across frequencies resulting in an ω^{-1} power law which Dong *et al.* (2023) show is consistent with the wave capture theory of Bühler & McIntyre (2005). They explain that this is not a contradiction of Kafiabad *et al.* (2019) and Cox *et al.* (2023) by demonstrating that the weak-flow approximation is violated as the ω^{-1}

power law forms. This is because as wave energy diffuses to higher wavenumbers, group speed c decays as $1/k$. Therefore, the ω^{-1} power law occurs outside both the diffusion and wider statistical scattering regimes. The relative importance of wave energy diffusion, scattering and wave capture theories in the observed energetics of the atmosphere and ocean is an open question.

Chapter 4

Conclusion

This thesis concerns the scattering of inertia-gravity waves by large-scale, slowly evolving inhomogeneities in the atmosphere and ocean. It builds upon previous work by McComas & Bretherton (1977) and Kafiabad *et al.* (2019) concerning the WKB limit – large-scale inhomogeneities, small-scale waves – of IGWs scattered by velocity inhomogeneities in which scattering becomes a diffusion in spectral space. A key finding of Kafiabad *et al.* (2019) is that if the velocity inhomogeneity is evolving sufficiently slowly as to be considered stationary, energy transfers in spectral space occur along cones of constant frequency and across-cone diffusion, corresponding to energy exchanges between waves of different frequencies, is negligible.

The diffusion equation can be derived by taking the WKB limit of a kinetic equation for scattering, as it is in McComas & Bretherton (1977) and Savva (2020). It can also be reached from the conservation of wave action in physical and spectral space which holds in the WKB regime. In §1.4, we derive this conservation equation for rotating shallow water waves propagating through a layer of variable height, the height variations being induced by geostrophic background flow. The derivation of the action conservation equation is standard. The novelty of the derivation here is its application to the rotating shallow water system and the introduction of variable layer height. To obtain the diffusion equation from the conservation equation for wave action, matched asymptotics are used, first done in Kafiabad *et al.* (2019).

In rotating shallow water, Dong *et al.* (2020) find slow time dependence induces significant diffusion of action and thus energy across the constant-frequency surface

in spectral space (a circle in two dimensions). This is an apparent contradiction to the assumption of Kafiabad *et al.* (2019). In chapter 2 (Cox *et al.*, 2023), we set out to answer the question: for inertia-gravity waves in a three-dimensional fluid, does slow time dependence in the background flow velocity field lead to significant diffusion across the constant-frequency cone in spectral space?

The key result of §2, and indeed this thesis, is the energy spectrum (2.39). This forced-equilibrium energy spectrum decays rapidly away from the forcing frequency and it does so in a thin boundary layer. Yes, time dependence does induce energy diffusion across the constant-frequency surface but this diffusion is negligible for a slowly evolving background flow and the dominant mechanism of energy transfer is resonant exchanges between waves of the same frequency. We attribute the difference between our conclusion and that of Dong *et al.* (2020) to the difference between constant-frequency surfaces. In the two-dimensional shallow water system, the constant-frequency surface is a compact circle meaning energy saturates about the surface, before spreading outwards. In three dimensions, the constant-frequency open cone allows for infinite along-cone energy spread.

A possible upshot of this analysis, discussed in §2.6, is its application to internal tide energy spectra. The energy spectra of internal tides are dominated by peaks at astronomical forcing frequencies. These peaks are broadened and it is understood that this broadening is due to interactions between the waves and low-frequency ocean processes. Munk *et al.* (1965) propose an estimate for this broadening due to low-frequency spectra – a so-called tidal cusp. Their heuristic estimate – which takes the low-frequency variability to be a modulating frequency for propagating tides – does not agree well with observation.

Munk *et al.* (1965) predict the shape of the cusp is dictated by the shape of the energy spectrum at zero frequency, whereas our theory predicts the cusp shape is determined by a ratio of flow acceleration and energy spectra. Our theory offers the prospect of a better quantitative description of the cusp than Munk *et al.* (1965). The width of the boundary layer quantifies the spreading of wave frequency due to a time-dependent background flow. Comparing this boundary layer width to observed cusp widths could help us understand the significance of wave-eddy interactions in causing internal tide frequency spread, compared to other processes such as wave-wave interactions. We

leave this exploration to future work.

As well as time-dependent background velocities, other inhomogeneities cause spectral diffusion. Prior to the paper presented in chapter 3 (Cox *et al.*, 2024, under review), spectral diffusion is only considered as a result of varying background velocities. The main result of this chapter is the generalisation of spectral diffusion to include other large-scale, slowly evolving inhomogeneities. We give two examples of these inhomogeneities that necessarily arise in the presence of a background flow due to geostrophic and thermal wind balances. We demonstrate that there are regimes where these inhomogeneities are significant. The generalisation of Cox *et al.* (2023) to include general inhomogeneities, in particular vertical buoyancy gradients induced by the flow velocity, is left to future work but, given the effect of these gradients decays as waves diffuse to higher wavenumber, we expect their impact to be limited. An exploration of the relationship between observed tidal cusp width and frequency spreading due to buoyancy fluctuations might also be an interesting line of research.

Finally, Dong *et al.* (2023) show that in 3D inertia-gravity waves form a broadband energy spectrum across frequencies when interacting with a geostrophic background flow. At first, this may seem like a contradiction to the work presented in this thesis. However, Dong *et al.* (2023) show that the broadband spectrum is formed outside of the diffusion regime when wave energy has diffused to high wavenumbers. The relative importance of the diffusion works presented here and the wave capture theory of Dong *et al.* (2023) in the observed energetics of the atmosphere and ocean is to be determined.

Appendix A

Additional material for diffusion induced by a time-dependent flow

A.1 Computing all diffusivity corrections

In this appendix, we present a general method to compute all non-zero corrections to the KSV diffusivity induced by a time-dependent flow. We use it to verify our expression for $D^{(1)}_{\theta\theta}$ and compute $D^{(1)}_{\phi\phi}$. This is of limited interest because in §2.2, we show that only $D_{kk}, D_{k\theta} = D_{\theta k}, D_{\theta\theta}$, and $D_{\phi\phi}$ are non-zero and in §2.3 we show that only the $D^{(1)}_{\theta\theta}$ correction is dynamically significant.

The leading-order correction to the time-independent flow diffusivity is given by (2.16). Using the spherical polar decomposition of $\boldsymbol{K}$ (2.11) and that $\boldsymbol{K}\cdot\boldsymbol{c}||\boldsymbol{K}\cdot\boldsymbol{e}_\theta$, we have

$$D^{(1)}_{ij} = \frac{\pi k^2 \sin^2\theta}{c^3|\cos^3\theta|}\int_0^\infty\int_0^\pi\int_{-\pi}^\pi KG_{ij}\sin^2\gamma A(\boldsymbol{K})\delta''\left(\cos\gamma - \frac{\cot\Theta}{\cot\theta}\right)\mathrm{d}K\mathrm{d}\Theta\mathrm{d}\gamma, \tag{A.1}$$

where $G_{ij} = K_iK_j/K^2\sin^2\Theta$ and we have used that $\delta''(\alpha x) = \delta''(x)/|\alpha|^3$. Note, $\sin\Theta/|\sin\Theta| = 1$ in the limits considered. Under the same variable change as used in

§2.2, $\zeta = \cos\gamma$, this becomes

$$D_{ij}^{(1)} = \frac{2\pi k^2 \sin^2\theta}{c^3|\cos^3\theta|}\int_0^\infty \int_\theta^{\pi-\theta}\int_{-1}^{1} KG_{ij}(1-\zeta^2)^{1/2}A(\boldsymbol{K})\delta''\left(\zeta - \frac{\cot\Theta}{\cot\theta}\right)\mathrm{d}K\mathrm{d}\Theta\mathrm{d}\zeta, \tag{A.2}$$

where the factor of 2 arises from the evenness of $\cos\gamma$. Assuming horizontal isotropy and integrating by parts twice,

$$D_{ij}^{(1)} = \frac{2\pi k^2 \sin^2\theta}{c^3|\cos^3\theta|}\int_0^\infty \int_\theta^{\pi-\theta} K\tilde{G}_{ij}(\zeta=\zeta_*)A(K,\Theta)\,\mathrm{d}K\mathrm{d}\Theta, \tag{A.3}$$

where $\tilde{G}_{ij} = \partial_{\zeta\zeta}(G_{ij}(1-\zeta^2)^{1/2})$ and $\zeta_* = \cot\Theta/\cot\theta$.

The derivative $\tilde{G}_{ij}(\zeta=\zeta_*)$ is straightforward to calculate for $D_{\theta\theta}^{(1)}$ but not as simple for other components. Furthermore, only $D_{\theta\theta}^{(1)}$ can be dynamically significant. We include $D_{\theta\theta}^{(1)}$ as a consistency check and $D_{\phi\phi}^{(1)}$ to demonstrate (A.3) can be used to calculate other corrections.

First checking $D_{\theta\theta}^{(1)}$,

$$\tilde{G}_{\theta\theta}(\zeta=\zeta_*) = 2\cos^2\theta\left(1-\frac{\cot^2\Theta}{\cot^2\theta}\right)^{1/2}, \tag{A.4}$$

and so

$$D_{\theta\theta}^{(1)} = \frac{4\pi k^2 \sin^2\theta}{c^3|\cos\theta|}\int_0^\infty \int_\theta^{\pi-\theta} K\left(1-\frac{\cot^2\Theta}{\cot^2\theta}\right)^{1/2}A(K,\Theta)\,\mathrm{d}K\mathrm{d}\Theta. \tag{A.5}$$

This is (2.23), an intermediate form of $D_{\theta\theta}^{(1)}$ leading to the final form (2.25).

For $D_{\phi\phi}^{(1)}$,

$$\tilde{G}_{\phi\phi}(\zeta=\zeta_*) = 3\frac{2\cot^2\Theta - \cot^2\theta}{|\cot\theta|(\cot^2\theta-\cot^2\Theta)^{1/2}}. \tag{A.6}$$

Thus,

$$D_{\phi\phi}^{(1)} = \frac{6\pi k^2|\sin^3\theta|}{c^3\cos^4\theta}\int_0^\infty \int_\theta^{\pi-\theta} K\frac{2\cot^2\Theta-\cot^2\theta}{(\cot^2\theta-\cot^2\Theta)^{1/2}}A(K,\Theta)\,\mathrm{d}K\mathrm{d}\Theta. \tag{A.7}$$

Substituting in the group speed c, (2.24),

$$D^{(1)}_{\phi\phi} = \frac{6\pi\omega^3 k^5}{(N^2 - f^2)^3 |\cos^7\theta|} \int_0^\infty \int_\theta^{\pi-\theta} K \frac{2\cot^2\Theta - \cot^2\theta}{(\cot^2\theta - \cot^2\Theta)^{1/2}} A(K,\Theta)\,\mathrm{d}K\mathrm{d}\Theta. \quad \text{(A.8)}$$

A.2 Recovering the time-independent flow diffusivity

Flow time dependence causes energy to spread across the forcing frequency cone in wavevector space. By integrating the energy spectrum across all angles, we account for this lost energy and recover the time-independent flow solution of KSV. This is equivalent to integrating the energy spectrum (2.39) over re-scaled angle σ between $\pm\infty$.

Let $e_0(k)$ denote this integral,

$$e_0(k) = \frac{1}{Q_*}\int_{-\infty}^{\infty} e(k,\sigma)\mathrm{d}\sigma = \frac{1}{2\pi Q_* k_*^{5/2} k^{1/2}} \int_{-\infty}^{\infty} \mathrm{Q}_{3/2}\left(\frac{k_*^2 + k^2 + \sigma^2}{2k_* k}\right)\mathrm{d}\sigma. \quad \text{(A.9)}$$

The factor of $1/Q_*$ appears because σ and e have been re-scaled. Under the substitution $X = (k_*^2 + k^2 + \sigma^2)/(2k_* k)$,

$$e_0(k) = \frac{1}{2^{1/2}\pi Q_* k_*^2} \int_{X_0}^{\infty} (X - X_0)^{-1/2} \mathrm{Q}_{3/2}(X)\mathrm{d}X, \quad \text{(A.10)}$$

where $X_0 = (k_*^2 + k^2)/(2k_* k)$. This is of the same form as Eq. (1), §7.133 of Gradshteyn & Ryzhik (2014),

$$\int_u^\infty \mathrm{Q}_\nu(x)(x-u)^{\mu-1}\mathrm{d}x = \Gamma(\mu)e^{\mu\pi i}(u^2-1)^{\mu/2}\mathrm{Q}_\nu^{-\mu}(u), \quad \text{(A.11)}$$

where $\mathrm{Q}_\nu^{-\mu}$ is the associated Legendre function of the second kind (DLMF, 2022, Ch. 14), and $|\arg(u-1)| < \pi$ and $0 < \mathrm{Re}(\mu) < 1 + \mathrm{Re}(\nu)$. For (A.10), $\mu = 1/2$ and $\nu = 3/2$ which satisfy both these conditions. Thus,

$$e_0(k) = \frac{\mathrm{e}^{\pi\mathrm{i}/2}(X_0^2 - 1)^{1/4}\mathrm{Q}_{3/2}^{-1/2}(X_0)}{2^{1/2}\pi^{1/2} Q_* k_*^2}. \quad \text{(A.12)}$$

From Eqs. (14.5.17) and (14.2.10) in DLMF (2022),

$$\mathrm{Q}_{3/2}^{-1/2}(X_0) = \pi^{1/2} e^{-\pi \mathrm{i}/2} e^{-2\zeta} / (2^{3/2} \sinh^{1/2} \zeta), \tag{A.13}$$

where ζ is defined through $\cosh \zeta = X_0$. Then, (A.12) becomes

$$e_0(k) = \frac{e^{-2\zeta}}{4Q_* k_*^2}. \tag{A.14}$$

Finally, we use the identity

$$\operatorname{arcosh} Y = \ln(Y + (Y^2 - 1)^{1/2}), \tag{A.15}$$

to obtain $\zeta = \operatorname{arcosh} X_0$, leaving the energy spectrum

$$e_0(k) = \frac{1}{2Q_*} \frac{k^2}{k_*^4 + k^4 + (k_*^2 + k^2)|k_*^2 - k^2|} = \frac{1}{4Q_* k_*^2} \times \begin{cases} k^2/k_*^2 & \text{for } 0 < k < k_* \\ k_*^2/k^2 & \text{for } k > k_* \end{cases}. \tag{A.16}$$

This is Eq. (4.1) of KSV, the forced energy spectrum for time-independent flow, with $Q_* = Q$ (in the time-independent flow case, Q does not change because there is no angular diffusion, so $Q = Q_*$).

Appendix B

Additional material for inhomogeneity-induced wavenumber diffusion

B.1 Perturbed Boussinesq frequencies

In this appendix, we perturb the linearised Boussinesq equations with constant background buoyancy and introduce weak buoyancy gradients in the vertical and horizontal. The vertical buoyancy gradient results in a perturbation to the mean buoyancy frequency, $\bar{N}^2$, in the IGW dispersion relation. The horizontal buoyancy gradient results in an imaginary frequency associated with shear instability.

The dispersion relation (3.10) is the result of a WKB ansatz applied to the Boussinesq equations (1.3)–(1.5), expressed as the right and left eigenvalue problem

$$\boldsymbol{B}\boldsymbol{\phi}^{(0)} = \mathrm{i}\omega_{\mathrm{in}}^{(0)}\boldsymbol{A}\boldsymbol{\phi}^{(0)} \quad \text{and} \quad \boldsymbol{\phi}_{\mathrm{L}}^{(0)}\boldsymbol{B} = \mathrm{i}\omega_{\mathrm{in}}^{(0)}\boldsymbol{\phi}_{\mathrm{L}}^{(0)}\boldsymbol{A}, \tag{B.1a,b}$$

where

$$\boldsymbol{B} = \begin{pmatrix} 0 & -f & 0 & 0 & ik_1 \\ f & 0 & 0 & 0 & ik_2 \\ 0 & 0 & 0 & -1 & ik_3 \\ 0 & 0 & \bar{N}^2 & 0 & 0 \\ ik_1 & ik_2 & ik_3 & 0 & 0 \end{pmatrix} \quad \text{and} \quad \boldsymbol{A} = \begin{pmatrix} 1 & 0 & 0 & 0 & 0 \\ 0 & 1 & 0 & 0 & 0 \\ 0 & 0 & 1 & 0 & 0 \\ 0 & 0 & 0 & 1 & 0 \\ 0 & 0 & 0 & 0 & 0 \end{pmatrix}. \tag{B.2a,b}$$

Here, the (0) superscript indicates the unperturbed eigenvector problem with right and left eigenvectors $\boldsymbol{\phi}^{(0)}$ and $\boldsymbol{\phi}_{\mathrm{L}}^{(0)}$.

We introduce $\boldsymbol{B'}$, an $O(\epsilon)$ correction to $\boldsymbol{B}$ and expand the new eigenvector $\boldsymbol{\phi}$ and intrinsic frequency ω_{in} in powers of ϵ such that

$$(\boldsymbol{B} + \epsilon\boldsymbol{B'})(\boldsymbol{\phi}^{(0)} + \epsilon\boldsymbol{\phi}^{(1)} + \dots) = i(\omega_{\mathrm{in}}^{(0)} + \epsilon\omega_{\mathrm{in}}^{(1)} + \dots)\boldsymbol{A}(\boldsymbol{\phi}^{(0)} + \epsilon\boldsymbol{\phi}^{(1)} + \dots) \tag{B.3}$$

and equivalent for the left eigenvector equation. The zeroth order in ϵ is trivially solved by (B.1a,b). At $O(\epsilon)$, the right eigenvector equation is

$$\boldsymbol{B}\boldsymbol{\phi}^{(1)} + \boldsymbol{B'}\boldsymbol{\phi}^{(0)} = i\omega_{\mathrm{in}}^{(0)}\boldsymbol{A}\boldsymbol{\phi}^{(1)} + i\omega_{\mathrm{in}}^{(1)}\boldsymbol{A}\boldsymbol{\phi}^{(0)}. \tag{B.4}$$

Applying the zeroth order left eigenvector to this expression and rearranging, we find that

$$\omega_{\mathrm{in}}^{(1)} = -i\frac{\boldsymbol{\phi}_{\mathrm{L}}^{(0)}\boldsymbol{B'}\boldsymbol{\phi}^{(0)}}{\boldsymbol{\phi}_{\mathrm{L}}^{(0)}\boldsymbol{A}\boldsymbol{\phi}^{(0)}}, \tag{B.5}$$

where we have used (B.1a,b) to remove the $\boldsymbol{\phi}^{(1)}$ terms.

A small vertical flow buoyancy gradient $\epsilon\partial_z B$ introduces an $\epsilon w\partial_z B$ term into the left-hand side of the wave buoyancy equation. As shown in Olbers (1981), this scaling is consistent with the WKB approximation with negligible velocity shear and horizontal buoyancy gradients but restricts us to large Richardson number, the square ratio between the vertical buoyancy gradient and vertical shear, for a flow in thermal wind balance.

Then,

$$\boldsymbol{B}' = \begin{pmatrix} 0 & 0 & 0 & 0 & 0 \\ 0 & 0 & 0 & 0 & 0 \\ 0 & 0 & 0 & 0 & 0 \\ 0 & 0 & \partial_z B & 0 & 0 \\ 0 & 0 & 0 & 0 & 0 \end{pmatrix}. \tag{B.6}$$

We use a computer algebra system to find the eigenvectors of (B.1a,b) and omit their full form for brevity. With the perturbation (B.6), (B.5) becomes the first term of ω_1 in the frequency (3.15) because $\sin^2\theta = (k_1^2 + k_2^2)/k^2$, $\cos^2\theta = k_3^2/k^2$ and $\omega_{\text{in}}^{(0)} = \omega_0$.

A small horizontal buoyancy gradient, for simplicity considered parallel to the x-axis, $\epsilon\partial_x B$, gives a perturbation matrix,

$$\boldsymbol{B}' = \begin{pmatrix} 0 & 0 & 0 & 0 & 0 \\ 0 & 0 & \partial_z V & 0 & 0 \\ 0 & 0 & 0 & 0 & 0 \\ \partial_x B & 0 & 0 & 0 & 0 \\ 0 & 0 & 0 & 0 & 0 \end{pmatrix}, \tag{B.7}$$

where the vertical shear $\partial_z V$ is induced by the thermal wind balance (3.11). For this perturbation, it can be shown that the real part of $\omega_{\text{in}}^{(1)}$ is proportional to $f\partial_z V + \partial_x B$ which is zero by thermal wind balance (thermal wind balance also results in a zero real part for the full horizontal gradient correction, $\epsilon\boldsymbol{\nabla}_{\boldsymbol{x},h}B$). The imaginary correction is

$$\omega_{\text{in}}^{(1)} = \mathrm{i}\cos\theta\sin\phi\left(1 + f^2/\omega_0^2\right)\partial_z V/2, \tag{B.8}$$

where ϕ is the azimuthal angle to the x-axis, we use that $\omega_{\text{in}}^{(0)} = \omega_0$, and we use thermal wind balance (3.11) to write the buoyancy gradient in terms of vertical shear.

We see that background horizontal buoyancy gradients induce a shear instability which grows or decays depending on the direction of the velocity shear. This is beyond the scope of this work and, as shown in Olbers (1981), a negligible effect for high Richardson number.

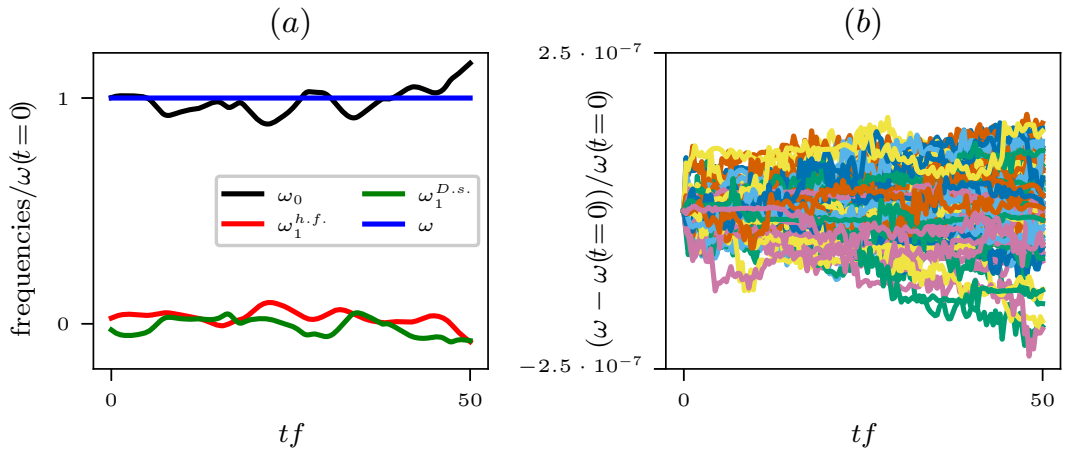

Figure B.1: Panel (a) shows the evolution of different frequency components of a single ray of the ray tracing simulation described in §3.3.2 and shown in figure 3.3. These components are: the bare frequency ω_0 in black; the height fluctuation component of ω_1 (see (3.5)) in red; the Doppler shift component $\boldsymbol{U}\cdot\boldsymbol{k}$ of ω_1 in green and; the absolute frequency ω (3.2) in blue. The components are normalised by the initial value of the absolute frequency $\omega(t = 0)$ and the time coordinate is non-dimensionalised by the Coriolis parameter f. Panel (b) shows the relative error on absolute frequency, which should be constant along each ray by (B.9), for 100 rays of the simulation.

B.2 Consistency check for ray tracing

The ray equations (3.49a,b) are Hamilton's equations for the Hamiltonian ω, the absolute frequency of the system. As ω is not an explicit function of time, the Hamiltonian is conserved and

$$\frac{\mathrm{d}}{\mathrm{d}t}\omega = 0 \tag{B.9}$$

along each constant-action trajectory. In figure B.1, we show that (B.9) holds for (a) a single ray in the ray tracing simulation described in §3.3.2 and shown in figure 3.3 and; (b) for 100 rays of the simulation to a high degree of accuracy. This is a consistency check for our code. Figure B.1(a) also demonstrates the weak interaction assumption underpinning the diffusion regime and the wider statistical scattering regime: the corrections ω_1 to the bare frequency ω_0 are much smaller than ω_0 itself.

B.3 Boussinesq diffusivities

B.3.1 Obtaining diffusivity expressions

In this appendix, we evaluate the general diffusivity (3.32) for the Boussinesq system with vertical buoyancy gradients.

We first substitute ω_1, defined in (3.15) with $B = f\partial_z\psi$ by the thermal wind balance (3.11), into the correlation function (3.29). Due to the two-dimensional nature of geostrophic flow, the Doppler shift term is the same here as it is in (3.35), the shallow water case, with the skew gradient 2D as before. The cross terms also cancel by a similar argument to (3.36). Then,

$$\Lambda(\boldsymbol{y},\boldsymbol{k},r) = \underbrace{-(\boldsymbol{k}\cdot\boldsymbol{\nabla}_{\boldsymbol{x}}^{\perp})^2\langle\psi(\boldsymbol{x},t)\psi(\boldsymbol{x}+\boldsymbol{y},t+r)\rangle}_{\text{Doppler shift}} + \underbrace{\frac{f^2\sin^4\theta}{4\omega_0^2}\partial_{zzzz}\langle\psi(\boldsymbol{x},t)\psi(\boldsymbol{x}+\boldsymbol{y},t+r)\rangle}_{\text{buoyancy fluctuation}}. \tag{B.10}$$

The vertical derivative in the buoyancy fluctuation term has been moved outside the ensemble average using integration by parts and the symmetry of $\boldsymbol{x}$ and $\boldsymbol{y}$ arguments. In Fourier space, this becomes

$$\hat{\Lambda}(\boldsymbol{K},\boldsymbol{k},\Omega) = |\boldsymbol{k}_h\times\boldsymbol{K}_h|^2E_\psi(\boldsymbol{K},\Omega) + \frac{f^2\sin^4\theta K_v^4}{4\omega_0^2}E_\psi(\boldsymbol{K},\Omega). \tag{B.11}$$

Here, K_v is the flow's vertical wavenumber and $\boldsymbol{K}_h$ its horizontal wavevector (distinct from $K_h = |\boldsymbol{K}_h|$, the horizontal wavenumber). Switching to polar coordinates $\boldsymbol{K} = (K,\gamma,\Theta)$, γ as before the angle between the horizontal wavevectors $\boldsymbol{K}_h$ and $\boldsymbol{k}_h$,

$$\hat{\Lambda}(\boldsymbol{K},\boldsymbol{k},\Omega) = 2k^2\sin^2\theta\sin^2\gamma E(\boldsymbol{K},\Omega) + \frac{f^2\sin^4\theta K^2\cos^4\Theta}{2\omega_0^2\sin^2\Theta}E(\boldsymbol{K},\Omega). \tag{B.12}$$

We have used the same definitions of E_ψ and E as in the shallow water case, but note that $E = K_h^2E_\psi/2 = K^2\sin^2\Theta E_\psi/2$. Combined with (3.32), we have a diffusivity that accounts for buoyancy gradients in a time-dependent flow.

We simplify to a time-independent flow and substitute (B.12) into (3.33),

$$\begin{aligned} D_{ij} =& 2\pi k^2 \sin^2\theta \int_0^\infty \mathrm{d}K \int_0^\pi \mathrm{d}\Theta \int_{-\pi}^\pi \mathrm{d}\gamma\, K_i K_j K^2 \sin\Theta \sin^2\gamma E(\boldsymbol{K})\delta(\boldsymbol{K}\cdot\boldsymbol{c}) \\ &+ \frac{\pi f^2 \sin^4\theta}{2\omega_0^2} \int_0^\infty \mathrm{d}K \int_0^\pi \mathrm{d}\Theta \int_{-\pi}^\pi \mathrm{d}\gamma\, \frac{K_i K_j K^4 \cos^4\Theta E(\boldsymbol{K})\delta(\boldsymbol{K}\cdot\boldsymbol{c})}{\sin\Theta}. \end{aligned} \tag{B.13}$$

As in KSV and CKV, we expand $\boldsymbol{K}$ in the local spherical basis $(\boldsymbol{e}_k, \boldsymbol{e}_\theta, \boldsymbol{e}_\phi)$ associated with $\boldsymbol{k}$ such that

$$\boldsymbol{K} = K\sin\Theta\left((\sin\theta\cos\gamma + \cot\Theta\cos\theta)\boldsymbol{e}_k + (\cos\theta\cos\gamma - \cot\Theta\sin\theta)\boldsymbol{e}_\theta + \sin\gamma\boldsymbol{e}_\phi\right). \tag{B.14}$$

We consider $\boldsymbol{D}$ in spherical components i.e. $D_{\theta\theta} = \boldsymbol{e}_\theta\cdot\boldsymbol{D}\cdot\boldsymbol{e}_\theta$, $D_{\theta k} = \boldsymbol{e}_\theta\cdot\boldsymbol{D}\cdot\boldsymbol{e}_k$ etc. We see that $\boldsymbol{D}\cdot\boldsymbol{c} = 0$ because upon moving $\boldsymbol{c}$ inside the integral, each integrand contains a factor of $\boldsymbol{K}\cdot\boldsymbol{c}$, the argument of the delta function. As $\boldsymbol{K}\cdot\boldsymbol{c} = c\boldsymbol{K}\cdot\boldsymbol{e}_\theta$ because $\boldsymbol{c} = \boldsymbol{\nabla}_{\boldsymbol{k}}\omega_0(\theta)$, this means that $D_{\theta\theta}$, $D_{\theta\phi} = D_{\phi\theta}$ and $D_{\theta k} = D_{k\theta}$ are all zero.

As in CKV, we use parity arguments to show that $D_{\phi k} = D_{k\phi} = 0$. The parity of K_iK_j with respect to γ is determined by the parity of pairwise products of $\boldsymbol{e}_k\cdot\boldsymbol{K}$ and $\boldsymbol{e}_\phi\cdot\boldsymbol{K}$. The parity of the delta function is even because of the parity of $\boldsymbol{K}\cdot\boldsymbol{e}_\theta$. Thus, only D_{kk} and $D_{\phi\phi}$ have even integrands in γ and only these components are non-zero. We assume the energy spectrum is horizontally isotropic such then $E(\boldsymbol{K}) = E(K,\Theta)$. This enables integration with respect to γ using, for example, a substitution of $\xi = \cos\gamma$. Thus,

$$\begin{aligned} D_{ij} =& \frac{4\pi k^2\sin^2\theta}{c|\cos\theta|} \int_0^\infty \mathrm{d}K \int_\theta^{\pi-\theta} \mathrm{d}\Theta\, K_iK_j(\xi_*)K(1-\xi_*^2)^{1/2}E(K,\Theta) \\ &+ \frac{\pi f^2\sin^4\theta}{\omega_0^2 c|\cos\theta|} \int_0^\infty \mathrm{d}K \int_\theta^{\pi-\theta} \mathrm{d}\Theta\, \frac{K_iK_j(\xi_*)K^3\cos^4\Theta E(K,\Theta)}{\sin^2\Theta(1-\xi_*^2)^{1/2}}, \end{aligned} \tag{B.15}$$

where $\xi_* = \cot\Theta/\cot\theta$. Note only values of Θ for which $|\cot\Theta/\cot\theta| < 1$ contribute to the integral, which reduces the integration range to $(\theta, \pi-\theta)$. This is discussed in §3.3.3.

We evaluate $(\boldsymbol{e}_k \cdot \boldsymbol{K})^2$ and $(\boldsymbol{e}_\phi \cdot \boldsymbol{K})^2$ at $\cos\gamma = \xi_*$,

$$(\boldsymbol{e}_k \cdot \boldsymbol{K})^2|_{\xi_*} = K^2 \sin^2\Theta(\sin\theta\xi_* + \cot\Theta\cos\theta)^2 \quad \text{and} \quad (\boldsymbol{e}_\phi \cdot \boldsymbol{K})^2|_{\xi_*} = K^2\sin^2\Theta(1-\xi_*^2), \tag{B.16}$$

and note that $c = (\partial_\theta\omega_0)/k = (\bar{N}^2 - f^2)\sin\theta\cos\theta/(k\omega_0)$. Thus, the two non-zero components of $\boldsymbol{D}$ are given by (3.55)–(3.56). Reassuringly, the Doppler shift terms in both these components agree with (A13) in KSV, up to a $(2\pi)^3$ factor due to differing Fourier convention, and typographical errors in both the lower limits of the integrals. One of these errors is corrected in (2.11) of CKV, but the lower limit of the K integral is still incorrect.

B.3.2 Frequency dependence of the radial diffusivity ratio

We explain the $(\omega_0/f)^{-2}$ power law of ratio $R'_{\mathrm{B},kk}$ (3.57a,b) and its behaviour as $\theta \to 0$. Substituting the radial diffusivity components (3.55) into (3.57a,b),

$$R'_{\mathrm{B},kk} = \frac{\sin^4\theta}{4(\omega_0/f)^2k_h^2}\frac{\int_0^\infty\int_\theta^{\pi-\theta} K^5\cos^6\Theta E(K,\Theta)(1-\cot^2\Theta/\cot^2\theta)^{-1/2}\sin^{-2}\Theta\,\mathrm{d}K\mathrm{d}\Theta}{\int_0^\infty\int_\theta^{\pi-\theta} K^3\cos^2\Theta E(K,\Theta)(1-\cot^2\Theta/\cot^2\theta)^{1/2}\,\mathrm{d}K\mathrm{d}\Theta}. \tag{B.17}$$

As $\omega_0/f \to 1$ and $\theta \to 0$, the prefactor goes to zero and the integrals tend to spectrum-dependent constants. Thus, the ratio $R'_{\mathrm{B},kk}$ tends to zero.

Transforming to variables $(K_h, Y) = (K/\sin\Theta, \cot\Theta/\cot\theta)$, we have that,

$$R'_{\mathrm{B},kk} = \frac{\cos^4\theta}{4(\omega_0/f)^2k_h^2}\frac{\int_0^\infty K_h^4\mathrm{d}K_h\int_{-1}^1 Y^6\tilde{E}(K_h, K_v = YK_h\cot\theta)(1-Y^2)^{-1/2}\,\mathrm{d}Y}{\int_0^\infty K_h^2\mathrm{d}K_h\int_{-1}^1 Y^2\tilde{E}(K_h, K_v = YK_h\cot\theta)(1-Y^2)^{1/2}\,\mathrm{d}Y}. \tag{B.18}$$

Here, we introduce the cylindrical energy spectrum $\tilde{E}(K_h, K_v) = 2\pi K_h E(\boldsymbol{K})$. For an energy spectrum which is vertically homogeneous across the integration domain in spectral space, $\tilde{E}(K_h, K_v) \approx \tilde{E}(K_h)$ and both integrals can be evaluated with respect to Y. Then,

$$R'_{\mathrm{B},kk} = \frac{5\cos^4\theta}{8(\omega_0/f)^2k_h^2}\frac{\int_0^\infty K_h^4\tilde{E}(K_h)\,\mathrm{d}K_h}{\int_0^\infty K_h^2\tilde{E}(K_h)\,\mathrm{d}K_h} \approx \frac{5\cos^4\theta}{8(\omega_0/f)^2(k_h/K_*)^2}. \tag{B.19}$$

For small θ, this gives a $(\omega_0/f)^{-2}$ power law.

The spectrum can be considered vertically homogeneous, even for small θ, because of the large aspect ratio of the flow, α (3.16). This approximation improves as either θ or α grows, the former because the integration domain over Θ shrinks. For the flow of CKV, we find (B.19) to be a good estimate of $R'_{\mathrm{B},kk}$ for $\cot\theta \gtrsim \alpha$ i.e. the point at which the integration domain $(\theta, \pi - \theta)$ coincides with the characteristic wavevector of the flow. At this point, θ is not large enough for the spectrum to appear homogeneous in the vertical and we attribute this better-than-expected approximation to the prefactor of (B.18) varying more quickly than the ratio of integrals with θ.

Bibliography

Achatz, U. 2022 Gravity Waves and Their Impact on the Atmospheric Flow. In *Atmospheric Dynamics*, pp. 407–505. Springer Berlin Heidelberg.

Alford, Matthew H., MacKinnon, Jennifer A., Simmons, Harper L. & Nash, Jonathan D. 2016 Near-inertial internal gravity waves in the ocean. *Annu. Rev. Marine Sci.* **8**, 95–123.

Arbic, B. K. 2022 Incorporating tides and internal gravity waves within global ocean general circulation models: A review. *Prog. Oceanogr.* **206**.

Ardhuin, F. & Herbers, T. H. C. 2002 Bragg scattering of random surface gravity waves by irregular seabed topography. *J. Fluid Mech.* **451**, 1–33.

Baines, P. G. 1982 On internal tide generation models. *Deep-Sea Res.* **29**, 307–338.

Bartello, P. 1995 Geostrophic adjustment and inverse cascades in rotating stratified turbulence. *J. Atmos. Sci.* **52**, 4410–4428.

Bell Jr., T. H. 1975 Topographically generated internal waves in the open ocean. *J. Geophys. Res. (1896-1977)* **80** (3), 320–327.

Bender, C. M. & Orszag, S. A. 1999 WKB Theory. In *Advanced Mathematical Methods for Scientists and Engineers I: Asymptotic Methods and Perturbation Theory*, pp. 484–543. Springer New York.

Bretherton, F. P. 1966 The propagation of groups of internal gravity waves in a shear flow. *Q. J. Roy. Meteorol. Soc.* **92** (394), 466–480.

Bretherton, F. P. 1971 The general linearised theory of wave propagation. *Lectures Appl. Math.* **13**, 61–102.

Bretherton, F. P. & Garrett, C. J. R. 1968 Wavetrains in inhomogeneous moving media. *Proc. R. Soc. Lond. Ser. A, Math. Phys.Sci.* **302** (1471), 529–554.

Bühler, O., Callies, J. & Ferrari, R. 2014 Wave–vortex decomposition of one-dimensional ship-track data. *J. Fluid Mech.* **756**, 1007–1026.

Bühler, O. & McIntyre, M. E. 2005 Wave capture and wave–vortex duality. *J. Fluid Mech.* **534**, 67–95.

Bölöni, G., Kim, Y.-H., Borchert, S. & Achatz, U. 2021 Toward transient subgrid-scale gravity wave representation in atmospheric models. part I: Propagation model including nondissipative wave–mean-flow interactions. *J. Atmos. Sci.* **78** (4), 1317 – 1338.

Bühler, O. & Holmes-Cerfon, M. 2011 Decay of an internal tide due to random topography in the ocean. *J. Fluid Mech.* **678**, 271–293.

Callies, J., Bühler, O. & Ferrari, R. 2016 The dynamics of mesoscale winds in the upper troposphere and lower stratosphere. *J. Atmos. Sci.* **73**, 4853–4872.

Callies, J. & Ferrari, R. 2013 Interpreting energy and tracer spectra of upper-ocean turbulence in the submesoscale range (1–200 km). *J. Phys. Oceanogr.* **43** (11), 2456–2474.

Callies, J., Ferrari, R. & Bühler, O. 2014 Transition from geostrophic turbulence to inertia–gravity waves in the atmospheric energy spectrum. *Proc. Nat. Acad. Sci.* **111**, 17033–17038.

Charney, J.G. 1948 On the scale of atmospheric motions. *Geofys. Publ.* **17** (2), 1–17.

Charney, J. G. 1971 Geostrophic turbulence. *J. Atmos. Sci.* **28** (6), 1087 – 1095.

Chavanne, C, Flament, P, Luther, D & Gurgel, KW 2010 The surface expression of semidiurnal internal tides near a strong source at hawaii. part II: Interactions with mesoscale currents. *J. Phys. Oceanogr.* **40** (6), 1180–1200.

Colosi, J. A. & Munk, W. 2006 Tales of the venerable honolulu tide gauge. *J. Phys. Oceanogr.* **36** (6), 967 – 996.

Cox, M. R., Kafiabad, H. A. & Vanneste, J. 2023 Inertia-gravity-wave diffusion by geostrophic turbulence: the impact of flow time dependence. *J. Fluid Mech.* **958**, A21.

Cox, M. R., Kafiabad, H. A. & Vanneste, J. 2024 Inhomogeneity-induced wavenumber diffusion (under review), arXiv: 2406.17149.

Danioux, E. & Vanneste, J. 2016 Propagation of near-inertial waves in random flows. *Phys. Rev. Fluids* **1**, 0033701.

Dewan, E. M. 1979 Stratospheric wave spectra resembling turbulence. *Science* **204**, 832–835.

DLMF 2022 *NIST Digital Library of Mathematical Functions*. http://dlmf.nist.gov/, Release 1.1.4 of 2022-01-15, F. W. J. Olver, A. B. Olde Daalhuis, D. W. Lozier, B. I. Schneider, R. F. Boisvert, C. W. Clark, B. R. Miller, B. V. Saunders, H. S. Cohl, and M. A. McClain, eds.

Dong, W., Bühler, O. & Smith, K. S. 2023 Geostrophic Eddies Spread Near-Inertial Wave Energy to High Frequencies. *J. Phys. Oceanogr.* **53** (5), 1311–1322.

Dong, W., Bühler, O. & Smith, K. S. 2020 Frequency diffusion of waves by unsteady flows. *J. Fluid Mech.* **905**, R3.

Doodson, A. T. 1921 The harmonic development of the tide-generating potential. *Proc. R. Soc. Lond. Ser. A, Cont. Pap. Math. and Phys. Char.* **100** (704), 305–329.

Eden, C. & Olbers, D. 2014 An energy compartment model for propagation, nonlinear interaction, and dissipation of internal gravity waves. *J. Phys. Oceanogr.* **44** (8), 2093–2106.

Eden, C., Pollmann, F. & Olbers, D. 2019 Numerical evaluation of energy transfers in internal gravity wave spectra of the ocean. *J. Phys. Oceanogr.* **49** (3), 737 – 749.

Eden, C., Pollmann, F. & Olbers, D. 2020 Towards a global spectral energy budget for internal gravity waves in the ocean. *J. Phys. Oceanogr.* **50** (4), 935 – 944.

Ferrari, R. & Wunsch, C. 2009 Ocean circulation kinetic energy: Reservoirs, sources, and sinks. *Annu. Rev. Fluid Mech.* **41**, 253–282.

Gage, K. S. & Nastrom, G. D. 1986 Theoretical interpretation of atmospheric wavenumber spectra of wind and temperature observed by commercial aircraft during GASP. *J. Atmos. Sci.* **43**, 729–740.

Garrett, C. & Kunze, E. 2007 Internal tide generation in the deep ocean. *Annu. Rev. Fluid Mech.* **39**, 57–87.

Geoffroy, G. & Nycander, J. 2022 Global mapping of the nonstationary semidiurnal internal tide using argo data. *J. Geophys. Res.: Oceans* **127** (4), e2021JC018283.

Gerkema, T., Maas, L. R. M. & van Haren, H. 2013 A note on the role of mean flows in doppler-shifted frequencies. *J. Phys. Oceanogr.* **43** (2), 432 – 441.

Gill, A. 1982 *Atmosphere-Ocean Dynamics*. Academic Press.

Gradshteyn, I. S. & Ryzhik, I. M. 2014 *Table of Integrals, Series, and Products*, 8th edn. Academic Press.

Hasselmann, K. 1966 Feynman diagrams and interaction rules of wave-wave scattering processes. *Rev. Geophys.* **4** (1), 1–32.

Jones, R. M. 2001 The dispersion relation for internal acoustic-gravity waves in a baroclinic fluid. *Phys. Fluids* **13** (5), 1274–1280.

Kachelein, L., Cornuelle, B. D., Gille, S. T. & Mazloff, M. R. 2022 Harmonic analysis of non-phase-locked tides with red noise using the red_tide package. *J. Atmos. Oceanic Tech.* **39** (7), 1031 – 1051.

Kafiabad, H. A., Savva, M. A. C. & Vanneste, J. 2019 Diffusion of inertia-gravity waves by geostrophic turbulence. *J. Fluid Mech.* **869**, R7.

Kelly, SM, Jones, NL, Nash, JD & Waterhouse, AF 2013 The geography of semidiurnal mode-1 internal-tide energy loss. *Geophys. Res. Lett.* **40** (17), 4689–4693.

Kelly, S. M., Jones, N. L., Ivey, G. N. & Lowe, R. J. 2015 Internal-tide spectroscopy and prediction in the timor sea. *J. Phys. Oceanogr.* **45** (1), 64 – 83.

Khatri, H., Sukhatme, J., Kumar, A. & Verma, M. K. 2018 Surface ocean enstrophy, kinetic energy fluxes, and spectra from satellite altimetry. *J. Geophys. Res. Oceans* **123** (5), 3875–3892.

Kim, Y.-H., Bölöni, G., Borchert, S., Chun, H.-Y. & Achatz, U. 2021 Toward transient subgrid-scale gravity wave representation in atmospheric models. part II: Wave intermittency simulated with convective sources. *J. Atmos. Sci.* **78** (4), 1339 – 1357.

Lahaye, N., Gula, J. & Roullet, G. 2020 Internal tide cycle and topographic scattering over the north mid-atlantic ridge. *J. Geophys. Res.: Oceans* **125** (12), e2020JC016376.

Lelong, M.-P. & Riley, J. J. 1991 Internal wave-vortical mode interactions in strongly stratified flows. *J. Fluid Mech.* **232**, 1–19.

Li, Q. & Lindborg, E. 2018 Weakly or strongly nonlinear mesoscale dynamics close to the tropopause? *J. Atmos. Sci.* **75** (4), 1215–1229.

Lindborg, E. 1999 Can the atmospheric kinetic energy spectrum be explained by two-dimensional turbulence? *J. Fluid Mech.* **388**, 259–288.

Luecke, C. A., Arbic, B. K., Richman, J. G., Shriver, J. F., Alford, M. H., Ansong, J. K., Bassette, S. L., Buijsman, M. C., Menemenlis, D., Scott, R. B., Timko, P. G., Voet, G., Wallcraft, A. J. & Zamudio, L. 2020 Statistical comparisons of temperature variance and kinetic energy in global ocean models and observations: Results from mesoscale to internal wave frequencies. *J. Geophys. Res.: Oceans* **125** (5).

McComas, C. H. & Bretherton, F. P. 1977 Resonant interaction of oceanic internal waves. *J. Geophys. Res.* **82**, 1397–1412.

Müller, P. 1976 On the diffusion of momentum and mass by internal gravity waves. *J. Fluid Mech.* **77** (4), 789–823.

Müller, P., Holloway, G., Henyey, F. & Pomphrey, N. 1986 Nonlinear interactions among internal gravity waves. *Rev. Geophys.* **24**, 493–536.

Müller, P. & Xu, N. 1992 Scattering of oceanic internal gravity waves off random bottom topography. *J. Phys. Oceanogr.* **22** (5), 474–488.

Munk, W. H., Cartwright, D. E. & Bullard, E. C. 1966 Tidal spectroscopy and prediction. *Phil. Trans. R. Soc. Lond. Ser. A, Math. Phys. Sci.* **259** (1105), 533–581.

Munk, W. H., Zetler, B. & Groves, G. W. 1965 Tidal Cusps. *Geophys. J. Int.* **10** (2), 211–219.

Müller, P. 1976 On the diffusion of momentum and mass by internal gravity waves. *J. Fluid Mech.* **77**, 789–823.

Müller, P. 1977 Spectral features of the energy transfer between internal waves and a larger-scale shear flow. *Dyn. Atm. Oceans* **2**, 49–72.

Müller, P. & Olbers, D. J. 1975 On the dynamics of internal waves in the deep ocean. *J. Geophys. Res.* **80**, 3848–3860.

Olbers, D., Eden, C., Becker, E., Pollmann, F. & Jungclaus, J. 2019 The IDEMIX model: Parameterization of internal gravity waves for circulation models of ocean and atmosphere. In *Energy Transfers in Atmosphere and Ocean* (ed. C. Eden & A. Iske), pp. 87–125. Springer International Publishing.

Olbers, D., Willebrand, J. & Eden, C. 2012*a* Geostrophic and quasi-geostrophic motions. In *Ocean Dynamics*, pp. 135–155. Springer Berlin Heidelberg.

Olbers, D., Willebrand, J. & Eden, C. 2012*b* Long waves. In *Ocean Dynamics*, pp. 211–286. Springer Berlin Heidelberg.

Olbers, D., Willebrand, J. & Eden, C. 2012*c* Sound waves. In *Ocean Dynamics*, pp. 159–175. Springer Berlin Heidelberg.

Olbers, D. J. 1981 The propagation of internal waves in a geostrophic current. *J. Phys. Oceanogr.* **11** (9), 1224 – 1233.

Pan, Y., Haley, P. J. & Lermusiaux, P. F.J. 2021 Interactions of internal tides with a heterogeneous and rotational ocean. *J. Fluid Mech.* **920**, A18.

Park, J.-H. & Watts, D. R. 2006 Internal tides in the southwestern japan/east sea. *J. Phys. Oceanogr.* **36** (1), 22–34.

Pedlosky, J. 1987 Inviscid shallow-water theory. In *Geophysical Fluid Dynamics*, pp. 57–178. Springer New York.

Phillips, N. A. 1963 Geostrophic motion. *Rev. Geophys.* **1** (2), 123–176.

Plougonven, R. & Zhang, F. 2014 Internal gravity waves from atmospheric jets and fronts. *Rev. Geophys.* **52** (1), 33–76.

Rainville, L. & Pinkel, R. 2006 Propagation of low-mode internal waves through the ocean. *J. Phys. Oceanogr.* **36** (6), 1220–1236.

Ryzhik, L., Papanicolaou, G. & Keller, J. B. 1996 Transport equations for elastic and other waves in random media. *Wave Motion* **24** (4), 327–370.

Savva, M.A.C., Kafiabad, H.A. & Vanneste, J. 2021 Inertia-gravity-wave scattering by three-dimensional geostrophic turbulence. *J. Fluid Mech.* **916**, A6.

Savva, M. A. C. 2020 Inertia-gravity-waves in geostrophic turbulence. PhD thesis, University of Edinburgh.

Savva, M. A. C. & Vanneste, J. 2018 Scattering of internal tides by barotropic quasigeostrophic flows. *J. Fluid Mech.* **856**, 504–530.

Schubert, R., Vergara, O. & Gula, J. 2023 The open ocean kinetic energy cascade is strongest in late winter and spring. *Commun. Earth Environ.* **4** (1), 450.

Scott, R. B. & Wang, F. 2005 Direct evidence of an oceanic inverse kinetic energy cascade from satellite altimetry. *J. Phys. Oceanogr.* **35** (9), 1650 – 1666.

Sebastia Saez, P., Eden, C. & Chouksey, M. 2024 Evolution of internal gravity waves in a mesoscale eddy simulated using a novel model. *J. Phys. Oceanogr.* **54** (4), 985 – 1002.

Sutherland, B. R. 2016 Internal wave transmission through a thermohaline staircase. *Phys. Rev. Fluids* **1**, 013701.

Tolman, H. L. 1990 The influence of unsteady depths and currents of tides on wind-wave propagation in shelf seas. *J. Phys. Oceanogr.* **20** (8), 1166 – 1174.

Vallis, G. K. 2017*a* Effects of Rotation and Stratification. In *Atmospheric and Oceanic Fluid Dynamics: Fundamentals and Large-Scale Circulation*, pp. 55–104. Cambridge University Press.

Vallis, G. K. 2017*b* Geostrophic Theory. In *Atmospheric and Oceanic Fluid Dynamics: Fundamentals and Large-Scale Circulation*, p. 171–212. Cambridge University Press.

Vallis, G. K. 2017*c* Shallow Water Systems. In *Atmospheric and Oceanic Fluid Dynamics: Fundamentals and Large-Scale Circulation*, pp. 105–142. Cambridge University Press.

Vallis, G. K. 2017*d* Wave Fundamentals. In *Atmospheric and Oceanic Fluid Dynamics: Fundamentals and Large-Scale Circulation*, pp. 215–250. Cambridge University Press.

Vanneste, J. 2013 Balance and spontaneous wave generation in geophysical flows. *Annu. Rev. Fluid Mech.* **45**, 147–172.

VanZandt, T. E. 1982 A universal spectrum of buoyancy waves in the atmosphere. *Geophys. Res. Lett.* **9** (5), 575–578.

Villas Bôas, A. B. & Young, W. R. 2020 Directional diffusion of surface gravity wave action by ocean macroturbulence. *J. Fluid Mech.* **890**, R3.

Voelker, G. S., Bölöni, G., Kim, Y.-H., Zängl, G. & Achatz, U. 2024 MS-GWaM: A 3-dimensional transient gravity wave parametrization for atmospheric models. *J. Atmos. Sci.* .

Waite, M. L. & Bartello, P. 2006 The transition from geostrophic to stratified turbulence. *J. Fluid Mech.* **568**, 89–108.

Wang, H., Villas Bôas, A. B., Vanneste, J. & Young, W. R. 2024 Scattering of surface waves by ocean currents: the U2H map (preprint), arXiv: 2402.05652.

Wang, H., Villas Bôas, A. B., Young, W. R. & Vanneste, J. 2023 Scattering of swell by currents. *J. Fluid Mech.* **975**, A1.

Watson, K. M. 1985 Interaction between internal waves and mesoscale flow. *J. Phys. Oceanogr.* **15**, 1296–1311.

Whalen, C., de Lavergne, C., Garabato, A., Klymak, J., MacKinnon, J. & Sheen, K. 2020 Internal wave-driven mixing: governing processes and consequences for climate. *Nat. Rev. Earth Environ.* pp. 1–16.

Wunsch, C. & Ferrari, R. 2004 Vertical mixing, energy, and the general circulation of the oceans. *Annu. Rev. Fluid Mech.* **36** (Volume 36, 2004), 281–314.

Yang, L., Barkan, R., Srinivasan, K., McWilliams, J. C., Shakespeare, C. J. & Gibson, A. H. 2023 Oceanic eddies induce a rapid formation of an internal wave continuum. *Commun. Earth Environ.* **4** (484).

Young, W. R. 2021 Inertia-gravity waves and geostrophic turbulence. *J. Fluid Mech.* **920**, F1.

Zaron, E. D. 2022 Baroclinic tidal cusps from satellite altimetry. *J. Phys. Oceanogr.* **52** (12), 3123 – 3137.

Zeitlin, V. 2018 *Geophysical Fluid Dynamics: Understanding (almost) everything with rotating shallow water models*. Oxford University Press.